Collective behaviours in living systems : from bacteria to molecular motors

Agnese Curatolo

▶ **To cite this version:**

Agnese Curatolo. Collective behaviours in living systems : from bacteria to molecular motors. Physics [physics]. Université Sorbonne Paris Cité, 2017. English. NNT : 2017USPCC244 . tel-02143186

HAL Id: tel-02143186
https://theses.hal.science/tel-02143186

Submitted on 29 May 2019

HAL is a multi-disciplinary open access archive for the deposit and dissemination of scientific research documents, whether they are published or not. The documents may come from teaching and research institutions in France or abroad, or from public or private research centers.

L'archive ouverte pluridisciplinaire **HAL**, est destinée au dépôt et à la diffusion de documents scientifiques de niveau recherche, publiés ou non, émanant des établissements d'enseignement et de recherche français ou étrangers, des laboratoires publics ou privés.

Thèse de doctorat

de l'Université Sorbonne Paris Cité

Préparée à l'Université Paris Diderot

Ecole doctorale EDPIF 564

Laboratoire Matière et Systèmes Complexes

Collective behaviours in living systems: from bacteria to molecular motors

Par Agnese Ilaria CURATOLO

Thèse de doctorat de Physique théorique

Dirigée par Julien TAILLEUR

Présentée et soutenue publiquement à Paris le 24 Novembre 2017

Président du jury : José HALLOY, Professeur, Université Paris Diderot

Rapporteurs : Antonio CELANI, Chargé de recherche, ICTP, Trieste
Namiko MITARAI, Professeur associé, Niels Bohr Institute, Copenhagen

Examinateurs : Roberto DI LEONARDO, Professeur associé, Sapienza Università, Rome
Aleksandra WALCZAK, Directrice de recherche, ENS, Paris

Directeur de thèse : Julien TAILLEUR, Directeur de recherche, Université Paris Diderot

Acknowledgements

It was nearly four years ago when, as a frightened and inexperienced student, I first sat in front of my computer and began to do research. This work is the result of the accumulation of failures and achievements, of the discovery of bugs and of new features, and if I now leave my student days as a less frightened and less inexperienced doctor, it is thanks to several people whom I would like to acknowledge.

First of all I wish to thank my directeur de thèse, without whom this thesis could not have taken shape. His tireless encouragement and wise guidance have led me throughout the maze of this Ph.D. until I could start to find the way by myself, and I hope that our paths will cross again in the future.

Next, I would like to thank those whom I had the chance to discuss and collaborate with during the many conferences, meetings, and schools that I had the opportunity to attend (thanks again, Julien). Finally, I want to express my gratitude to the members of the jury for the time they have devoted to reading, evaluating, and discussing my research.

To conclude, many thanks to all the people who contributed to restore laughter when times were tough and enthusiasm when times were dull throughout these years. First, to the members of the laboratoire MSC, with a special thanks to Mourtaza, my “little brother”, for his contagious cheerfulness, and to Alex, my “big brother”, who always believed in me. Also, life would not have been the same without the constant presence of my three Francescas and our long chats, accompanied sometimes by birretta, sometimes by tisanina. Last, I would like to thank my family and all the zie and zii scattered around several countries.

Résumé

La première partie de ma thèse est consacrée à l'étude de l'auto-organisation de souches génétiquement modifiées de bactéries *Escherichia coli*. Ce projet, réalisé en collaboration avec des biologistes synthétiques de l'Université de Hong Kong, a pour objectif l'exploration et le décryptage d'un nouveau mécanisme d'auto-organisation dans des colonies bactériennes multi-espèces. Cela a été inspiré par la question fascinante de comment les écosystèmes bactériens comprenant plusieurs espèces de bactéries peuvent s'auto-organiser dans l'espace. En considérant des systèmes dans lesquels deux souches de bactéries régulent mutuellement leurs motilités, j'ai pu montrer que le contrôle de densité réciproque est une voie générique de formation de motifs: si deux souches tendent à faire augmenter mutuellement leur motilité (la souche A se déplace plus vite quand la souche B est présent, et vice versa), ils subissent un processus de formation de motifs conduisant à la démixtion entre les deux souches. Inversement, l'inhibition mutuelle de la motilité conduit à la formation de motifs avec colocalisation. Ces résultats ont été validés expérimentalement par nos collaborateurs biologistes. Par la suite, j'ai étendu mon étude à des systèmes composés de plus de deux espèces en interaction, trouvant des règles simples permettant de prédire l'auto-organisation spatiale d'un nombre arbitraire d'espèces dont la motilité est sous contrôle mutuel. Cette partie de ma thèse ouvre une nouvelle voie pour comprendre l'auto-organisation des colonies bactériennes avec des souches concurrentes, ce qui est une question importante pour comprendre la dynamique des biofilms ou des écosystèmes bactériens dans les sols.

Le deuxième problème traité dans ma thèse est inspiré par le comportement collectif des moteurs moléculaires se déplaçant le long des microtubules dans le cytoplasme des cellules eucaryotes. Un modèle pertinent pour le mouvement des moteurs moléculaires est donné par un système paradigmatique de non-équilibre appelé Processus Asymmetrique d'Exclusion Simple, en anglais Asymmetric Simple Exclusion Process (ASEP). Dans ce modèle sur réseau unidimensionnel, les particules se déplacent dans les sites voisins vides à des taux constants, avec un biais gauche-droite qui déséquilibre le système. Lors-qu'il est connecté à ses extrémités à des réservoirs de particules, l'ASEP est un

exemple prototypique de transitions de phase unidimensionnelles guidées par les conditions aux limites. Les exemples réalistes, cependant, impliquent rarement une seule voie: les microtubules sont constitués de plusieurs pistes de tubuline auxquelles les moteurs peuvent s'attacher. Dans ma thèse, j'explique comment on peut théoriquement prédire le comportement de phase de systèmes à plusieurs voies complexes, dans lesquels les particules peuvent également sauter entre des voies parallèles. En particulier, je montre que la transition de phase unidimensionnelle vue dans l'ASEP survit cette complexité supplémentaire mais implique de nouvelles caractéristiques telles que des courants transversaux stables non-nulles et une localisation de cisaillement.

Mots cléfs:

1. systèmes hors-équilibre
2. matière vivante
3. morphogenèse
4. transitions de phase
5. formation des motifs
6. colonies de bactéries
7. moteurs moléculaires
8. particules auto-propulsées

Abstract

The first part of my thesis is devoted to studying the self-organization of engineered strains of run-and-tumble bacteria *Escherichia coli*. This project, carried out in collaboration with synthetic biologists at Hong Kong University, has as its objective the exploration and decipherment of a novel self-organization mechanism in multi-species bacterial colonies. This was inspired by the fascinating question of how bacterial ecosystems comprising several species of bacteria can self-organize in space. By considering systems in which two strains of bacteria mutually regulate their motilities, I was able to show that reciprocal density control is a generic pattern-formation pathway: if two strains tend to mutually enhance their motility (strain A moves faster when strain B is present, and conversely), they undergo a pattern formation process leading to demixing between the two strains. Conversely, mutual inhibition of motility leads to pattern formation with colocalization. These results were validated experimentally by our biologist collaborators. Subsequently, I extended my study to systems composed of more than two interacting species, finding simple rules that can predict the spatial self-organization of an arbitrary number of species whose motility is under mutual control. This part of my thesis opens up a new route to understand the self-organization of bacterial colonies with competing strains, which is an important question to understand the dynamics of biofilms or bacterial ecosystems in soils.

The second problem treated in my thesis is inspired by the collective behaviour of molecular motors moving along microtubules in the cytoplasm of eukaryotic cells. A relevant model for the molecular motors' motion is given by a paradigmatic non-equilibrium system called Asymmetric Simple Exclusion Process (ASEP). In this one-dimensional lattice-based model, particles hop on empty neighboring sites at constant rates, with a left-right bias that drives the system out of equilibrium. When connected at its ends to particle reservoirs, the ASEP is a prototypical example of one-dimensional boundary driven phase transitions. Realistic examples, however, seldom involve only one lane: microtubules are made of several tubulin tracks to which the motors can attach. In my thesis, I explained how one can theoretically predict the phase behaviour of complex multilane systems, in

which particles can also hop between parallel lanes. In particular, I showed that the one-dimensional phase transition seen in the ASEP survives this additional complexity but involves new features such as non-zero steady transverse currents and shear localization.

Key words:

1. non-equilibrium systems
2. living matter
3. morphogenesis
4. phase transitions
5. pattern formation
6. bacterial colonies
7. molecular motors
8. self-propelled particles

Contents

Introduction

Living systems belong to a world which is governed by the laws of biology, but, at the same time, they must obey the rules of physics. The efforts to decipher biological problems by the means of physical tools often clash with several complications that typically arise when dealing with living organisms: very noisy environments, large number of degrees of freedom, large temporal and spatial scale separations, are common situations that biophysicists have to cope with. Such situations, in fact, are not peculiar to the living world: indeed, solving the dynamics of systems of many interacting units and finding connections between microscopic and macroscopic properties are typical problems that can be treated by using the tools of statistical physics.

Living systems are, by definition, out of equilibrium. At all scales, from the replication of DNA inside cells, to the growth of multicellular systems, to the collective motion of groups of animals, energy is taken from the environment to supply all different kinds of chemical reactions, leading to the many and varied functions of the organism. The direct consequence of this "non-equilibriumness" is that there are no general approaches to analyse biological processes and one needs to resort to the study of case-specific dynamics, different for every system or problem. Moreover, even the identification of the relevant variables and degrees of freedom – necessary to establish a mathematical description of the dynamics – is often a very difficult task. Here lies the great challenge for statistical biophysics: it is first necessary to construct a model that describes the dynamics at a given scale and with a given degree of detail, and only then one can use the tools of non-equilibrium statistical physics to study the dynamics.

Despite the great variability of biological situations and the absence of general biophysical theories, it is possible to define some classes of problems that present conceptual similarities. One of these classes comprises systems composed of many motile units – which could be molecules, cells, animals, etc...– that, by interacting in various ways, exhibit collective behaviours at scales much larger than the size of the single unit. Independently of the internal mechanism – different for each system and that distinguishes these motile units from passive diffusing Brownian particles – each unit can be modeled as a self-propelled particle. These particles consume energy taken from the environment

in order to attain directed motion. Then, each particle carries an internal degree of freedom that corresponds to the state of its internal motor.

This class often goes under the name of "active matter", although the field of active matter actually expands beyond the borders of biology: experimentally, systems of synthetic self-propelled particles can be realized, for instance by combining mechanical or chemical energy sources with spatial anisotropy. Theoretically, active matter has attracted a lot of attention in recent years: thanks to the fact that active systems do not in general obey the laws of equilibrium thermodynamics, simple models can entail a very rich and new phenomenology.

This thesis lies within this framework of statistical physics of active matter. We investigate emergent collective behaviours of two different systems: first, at the cellular level, we study pattern formation in bacterial colonies; then, at the sub-cellular level, we consider molecular motors moving along the cytoskeleton filaments. For both systems, we show how it is possible to obtain hydrodynamic descriptions of the collective dynamics, starting from microscopic models, i.e., considering the dynamics of each single bacterium or motor. In particular, at the many-body level, we investigate how intrinsically non-equilibrium microscopic interactions can give rise to phase transitions at the population scale.

The thesis is divided into two parts: part I is dedicated to the study of pattern formation and spatial organization of populations of motile bacteria. This project is the result of a collaboration with a team of synthetic biologists from the university of Hong Kong. Chapter 1 is an introduction to the field of pattern formation in biology. Chapter 2 focuses on pattern formation in single-species bacterial colonies. We first recap some existing experimental results and a phenomenological theory to account for them. We then show how to build a bottom-up approach to establish a more faithful model and a more direct connection with the experiments. In chapter 3 we describe the multispecies experiments that we designed with our biologist collaborators and show that in this case it is possible to observe a richer phenomenology. We extend the single-species model to a multispecies case, and show the good agreement between experimental results and such model by performing numerical simulations. We then discuss in detail the underlying pattern formation mechanism in the case of two-species colonies. Finally, in chapter 4 we extend our analysis to systems comprising a larger number of species of self-propelled particles.

This part of my thesis will be published in three articles which are currently in preparation: a letter on the two-species project including both the experiments and their theoretical modelling, which should be submitted shortly; a technical account on the coarse-graining procedure in the one-species case, focusing on the role of finite tumble duration; and a last article on the phase-separation of N interacting species.

The work presented in part II of the thesis is published in [34] and was selected for the Journal of Physics A Highlights of 2016 collection. This project was inspired by the transport processes that take place in the cytoplasm of eukaryotic cells. We consider driven diffusive systems as a model for the motion of molecular motors and study their phase diagram in the general case of multilane systems. In chapter 5 we introduce the field of driven diffusive systems and we illustrate the importance of considering of multilane problems. In chapter 6 we present the general framework we used to describe multilane systems, at the level of continuum mean-field equations. We perform a linear analysis of these equations and in chapter 7 we use the results to formulate a general method for constructing phase diagrams. We then turn to concrete examples and present numerical simulations of microscopic models.

Part I

Spatial organization in multispecies bacterial systems

Chapter 1

Pattern formation in biology: a physicist's perspective

The formation of patterns in the living world is a phenomenon that occurs in the most varied scales and contexts: the dots and stripes on the coats of many animals, the spirals of plant organs along the stem, or our fingerprints are common examples of the emergence of ordered structures in living organisms. Understanding how patterns are formed is a major challenge. The variety of situations in which they arise suggests that a large number of different mechanisms could be responsible for their formation, despite the fact that often, due to symmetry arguments, the emergent structures look very similar (see Fig. 1.1). In addition, these mechanisms are usually very complicated, involving mechanical as well as chemical interactions, at different scales and at different grades of complexity: an event, that could be a chemical reaction, the expression of a gene or a change in physical conditions, produces physical and biochemical signals that trigger the occurrence of other intermediate events, and the formation of the patterns is just the result of a long, layered, and in general overwhelmingly complicated process. Another challenge that one faces is the need of increasingly innovative technologies to observe a specific behaviour, identify the signals that induced it, and quantify them. The technological progress achieved in the past fifty years is rather astonishing. For instance, in the sixty years since the discovery of DNA, scientists have learnt to decipher and manipulate genes so as to control some pattern formation processes using the tools of synthetic biology, something that cells learned to do in billions of years of evolution. And yet it is still a long way for technology to match the ability of living organisms in recognizing the "right" signals and respond to them in an organized way.

In the context of experimental investigation, the exchange of knowledge between biology and physics has undeniably been very successful. Many modern experiments in biology partly rely on techniques based on physical properties of light and matter. In turn,

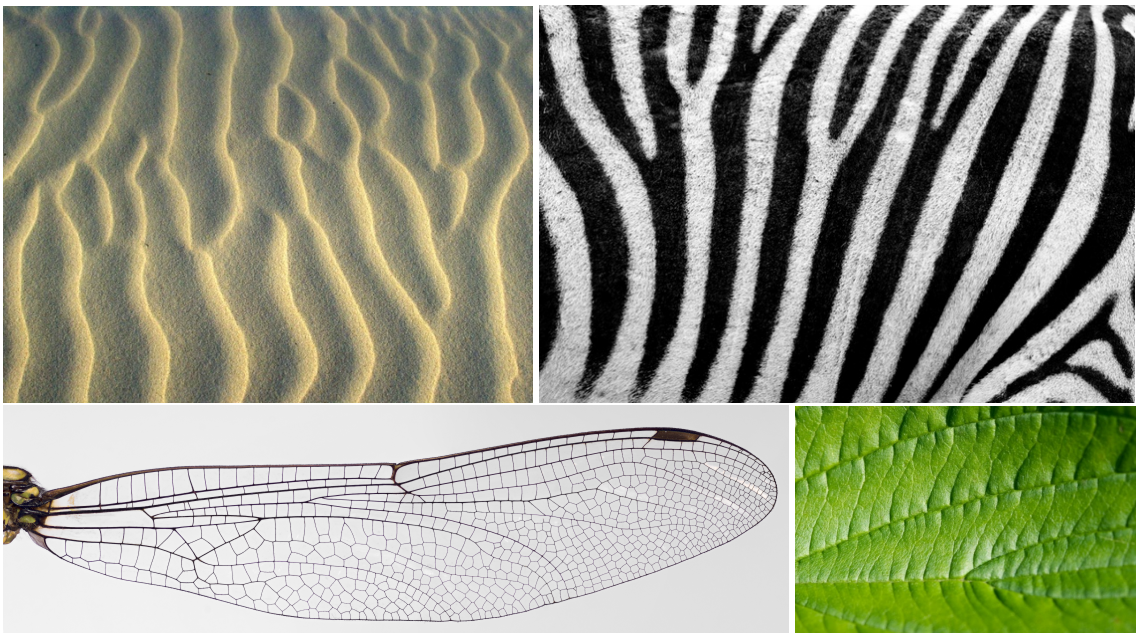

Figure 1.1 – Different systems exhibit similar patterns. **Top**: Stripes. Left: sand ripples. Right: zebra coat. **Bottom**: Venations. Left: dragonfly wing (courtesy of Massimo Demma). Right: leaf.

this has motivated new developments in experimental physics [96]. In the field of theoretical biology and biophysics, the two communities' occasions and reasons to interact have unfortunately been more scarce. This could stem from the questions and the ways to answer them being usually quite different in biology and physics [14]. While biologists' questions are usually problem specific, physicists are more interested in knowing if some general principles and mechanisms are at play. Consequently, biologists' answers are often based on observation and aimed at providing quantitative results, while physicists try to be more predictive, at the cost of often being only qualitative.

In the field of pattern formation and more generally that of developmental biology (the branch of biology that studies the growth and development of multicellular organisms) biology and physics often stand far apart from each other [73]. It is useful to briefly review the steps that led to the present situation to understand why the interactions between biology on one side and physics and mathematics on the other are so important in the study of morphogenesis and pattern formation.

1.1 A brief history of developmental biology

Until the beginning of the 20th century, the limited understanding of how a single cell leads to a fully developed animal or plant still led some scientists to believe in the existence of a vital force (see, e.g., [42] and [8] for a short review), which would set a clear barrier between living and non-living matter. This philosophy of vitalism was not accepted by another part of the scientific community (see, e.g., [4]) which was convinced that no such forces existed and that the origins of morphogenesis (the formation of shapes and structures), and development in general, were to be found in purely physical and chemical forces, those same forces that apply to inorganic matter. Among the most fervent supporters of the physico-chemical origin of morphogenesis was Stéphane Leduc (see [30] for an overview of his work), who not only claimed that life could originate spontaneously from the inanimate world [85], but even performed experiments, described in his book "La biologie synthétique" [86]. By using simple inorganic setup, (e.g. adding salts in a colloidal medium) he was able to reproduce, thanks to the simple effects of diffusion and osmosis, shapes and structures very reminiscent of plants, fungi and even cellular tissues.

Even though some of his theories have since been proven wrong – like for example that of spontaneous generation – the idea that physical and chemical forces alone are responsible for the spatial self-organization of cells were shared by many, as for example D'arcy Thompson and Julian Huxley who tackled the problems of growth and development with mathematical modelling [142, 65]. These are few examples of the first attempts to change the original observational and descriptive nature of developmental biology and make it a more formal science with a stronger predictive power. The underlying suggestion of the use of mathematics and physics to build theories for the development of living organisms is that these processes are governed by general rather than case-specific principles.

The discovery of the structure of DNA in 1953 [151] and the consequent rapid development of the field of genetics and molecular biology provided new tools for the study of development and morphogenesis. It seemed then that it was just a matter of time before the genome of different organisms – and in particular the human genome – would be completely sequenced and the understanding of many biological problems – such as the origin of some deseases, the theory of evolution and of course developmental biology – finally clarified. Indeed, genetics and molecular biology allowed scientist to make huge steps forward in identifying the origin of genetic diseases such as albinism or color blindness, caused by the malfunctioning of specific genes. It is however unlikely that genetic instructions alone are able to control the formation and development of multicellular structures [153, 100]: there must exist various flexible feedback mechanisms which make the interacting cells orchestrate their motion and spatial organization in response

to external mechanical and chemical stimuli. Molecular biology and physical models can then be used together in order to study these processes: the identification of the different genes, the proteins they express, and their function, which could in principle give us an *a priori* information of how the cell grows and differentiates, must be complemented by the analysis of the shapes and structures and the *a posteriori* postulation of the most likely mechanisms that lead to them.

1.2 From mathematics to biology and physics

The standard physics approach to the study of patterns is to look for the mechanism or the change in the system's properties that cause a symmetry breaking in an initially homogeneous condition [33, 64]. The paradigmatic example of pattern formation in physics is the Rayleigh-Bénard convection where a temperature gradient between two flat horizontal plates may cause the fluid between them, initially at rest, to start moving and form spatial patterns, known as stripes or convection rolls. This symmetry breaking (the appearance of stripes in an initially homogeneous fluid) occurs when the control parameter (the temperature gradient) is such that the initial condition becomes unstable to small random fluctuations (linear instability). In this regime all unstable modes grow exponentially and the most unstable mode (the one that grows fastest) selects the initial wavelength of the pattern. The direction of the stripes, or the shape of the more complex patterns that the fluid can form (hexagons and squares), is determined by both the geometry of the container and by successive symmetry breaking events (nonlinear instabilities).

Similarly, patterns in biological systems often emerge from the breaking of an underlying symmetry. While the Rayleigh-Bénard stripes are controlled by an external parameter (the temperature gradient), in a developing organism it is not at all clear what causes the linear instability. Even before starting to wonder what kind of patterns a system can form (if stripes, dots or more complicated structures), it is first necessary to identify the mechanisms that initiate the pattern formation process.

1.2.1 Turing patterns

One of the most well-known mechanisms was proposed by Alan Turing in 1952 [144], when he postulated that patterns could be formed in a developing embryo as a consequence of the interaction between two diffusing and reacting chemical substances, which he called *morphogens*. In his simplified model of the developing embryo, Turing describes the initial homogeneous state of the system (an idealized blastula) as a ring of cells or as a continuous ring of tissue. Two – or more – morphogens can react with one another

and diffuse along the ring. If the diffusion constants and the reaction rates vary in such a way that the homogeneous ring becomes unstable, then small fluctuations – due, e.g., to Brownian movement or irregularities of the form – cause the morphogens to rearrange spatially to form concentration gradients, whence breaking the symmetry. As in Rayleigh-Bénard convection, the pattern can appear in any direction, depending on the random fluctuations that caused the instability to set in: the differentiation between the dorsal and ventral regions of the embryo can occur in any direction, as long as the two regions are opposed to each other. Once the morphogens prepattern is established, cells can grow, differentiate and move accordingly.

Typical reaction-diffusion equations for the dynamics of the concentration fields of two chemicals $X(\mathbf{r}, t)$ and $Y(\mathbf{r}, t)$ are of the form

$$\begin{aligned} \dot{X} &= f(X, Y) + D_X \Delta X \\ \dot{Y} &= g(X, Y) + D_Y \Delta Y, \end{aligned} \tag{1.1}$$

where D_X and D_Y are the two diffusivities and $f(X, Y)$ and $g(X, Y)$ are nonlinear functions describing the rates at which X and Y increase, respectively. The nonlinearities of the reacting terms are required to saturate the exponential growth of the unstable modes. Eqs. (1.1) are very general and allow for different families of solutions (stationary or oscillatory) depending on the functions $f(X, Y)$ and $g(X, Y)$ [87]. These functions can be obtained either from the exact chemical reactions or by phenomenological considerations. In his original paper, Turing considers "imaginary reactions which give rise to the required functions by the law of mass action" [144, p. 43], where the "required function" is simply to make the system linearly unstable.

This function is summarized in the simple principle of *local self-enhancement and long-range inhibition* [52, 77]: in a two-chemical-species reaction-diffusion system, one species is an *activator*, while the other is an *inhibitor*. The activator enhances both the inhibitor and its own production, while the inhibitor suppresses the activator. If the inhibitor diffuses much faster than the activator, a small unbalance in the relative concentration of the two chemicals is sufficient to cause their segregation.

Following this principle, Turing showed that it is possible to obtain several different solutions of Eqs. (1.1) at the linear level by simply exploring the parameter space in the unstable region. Since then, the practice of classifying the spatio-temporal patterns according to the linear instability has become commonly accepted in the community of non-equilibrium physicists [33].

Although the author himself wrote that "this model will be a simplification and an idealization, therefore a falsification" [144, p. 37], Turing's mechanism of reactive-diffusive

chemicals has been observed in several and rather different experimental systems, for example in coupled chemical reactions where the system presented periodic oscillations [9, 157, 71]. The question remains as to whether the mechanism can be found in biological systems and, in particular, if it is responsible for the formation of patterns in organisms. Early investigations came from the study of the developing embryo of *Drosophila melanogaster* [43], a model system in embryogenesis, in which a protein (*bicoid*) has been identified as a good candidate for a prepatterning morphogen. More recent studies in mice hair follicles [127], periodic barbs of bird feathers [58], and ridges of the mammalian palette [45] investigated the role of other pairs of proteins acting as Turing's activators and inhibitors. It is however not clear if the prepatterns observed in experiments originates from Turing's mechanism of local self-enhancement and long-range inhibition [80, 63]. Moreover, the model does not give any explanation of how the cells responsible of morphogenesis actually sense the morphogens and are able to respond to them in the "correct" way.

Turing's contribution to the theory of pattern formation and morphogenesis is precious for at least two reasons: it inspired a lot of research in reaction-diffusion mechanisms in both theoretical and experimental systems in biology and chemistry and it emphasized the usefulness of mathematical formalism of partial differential equations (PDEs) in the investigation of patterns in biology. This has become very common in the field of mathematical biology, whose main approach is to find appropriate phenomenological equations to describe some observed processes. A great help comes from simulations of reaction-diffusion equation, whose solutions indeed resemble patterns found in nature, e.g. on the coat of animals like leopards or fish [100, 79]. However, one must be careful not to consider the similarities between the observed natural phenomena and the results of simulations of phenomenological PDEs as a proof of the correctness of the underlying model. As the same type of patterns can emerge due to very different microscopic mechanisms, the practice of "pattern matching" is a dangerous strategy.

More realistic models to explain pattern formation, i.e. based on more precise biological observations, have been formulated in other contexts. In particular, chemotaxis and quorum sensing are two biological mechanisms which are known to cause cells to collectively move and interact. It is thus natural to explore the collective behaviours they allow and look for possible pattern-forming processes. Note that chemotaxis and quorum sensing are mechanisms that influence the cells' behaviour at single cell level. Since we are interested in collective behaviours, our goal is to show what are the consequences of these mechanisms at macroscopic scales and how this scale separation can be treated using the tools of statistical physics.

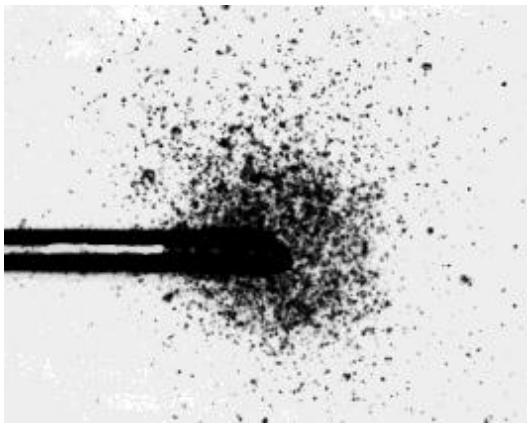

Figure 1.2 – A capillary assay invented by W. Pfeffer in the 1880's. The test chemical diffuses from the capillary mouth, establishing a steep gradient that attracts bacteria to the entrance.

From now on we consider the formation of patterns in a specific subset of living system: bacterial colonies. Bacteria are among the simplest cells, which makes them paradigmatic organisms to investigate problems in the field of molecular biology and genetics. They can show very complex collective behaviours, from the formation of biofilms to fractal shapes in growing colonies [10, 72]. Although very different from multicellular organisms, bacterial colonies undergo growth, differentiation and spatial self-organization [126, 149]. The formation of bacterial aggregates, observed in many different species (such as *Pseudomonas aeruginosa* [37], *Bacillus subtilis* [17], or *Escherichia coli* [112]) and environments (such as oceans, soil, or the human body [31, 36]), is caused by a plethora of different processes and mechanisms. As in the case of morphogenesis in multicellular organisms, structures and forms in bacterial colonies can emerge naturally as a consequence of complicated interactions and identifying underlying mechanisms is, once again, a major challenge.

In the next two sections we discuss some widely investigated mechanisms that can give rise to collective behaviour in bacterial colonies. The first is chemotaxis, the ability of cells to respond to a chemical gradient, and the second is quorum sensing, the ability of single cells to coordinate their gene regulation according to population density.

1.2.2 Chemotaxis

Chemotaxis is a biological function which allows organisms to move towards or away from chemicals. It has been observed in many different living systems and in particular bacteria. It has received a lot of interest in the past fifty years not only to explain cells spatial

organization, but also as a paradigm for sensory system[1].

It is known that bacteria are able to accumulate in the vicinity or away from a chemical source (see fig. 1.2). They can also form patterns and structures, as observed for instance in the pioneering experiments by Adler [1], in the form of macroscopic bands inside a capillary tube or concentric rings in an agar plate: for instance bacteria can create gradients in the nutrient and then move preferentially in the direction of higher nutrient concentration, hence generating swarming rings. How do these extremely simple cells achieve directed motion? Bacteria[2] swim by performing a series of *runs*, persistent motion in a specific direction, separated by events called *tumbles*, during which the direction of motion changes abruptly. Berg and Brown [13] found that the durations of the runs and of the tumbles follow an exponential distribution and that the mean tumbling rate decreases when cells are swimming in the direction of increasing attractant concentration. The longer steps made by the bacteria when they swim up-gradients then generate a mean drift towards chemoattractants.

Following the experimental observations, a semi-phenomenological model was introduced in the 70's to explain the peculiar collective behaviour of chemotactic bacteria [75]. In the model, motile bacteria of density b undergo diffusion and chemotactically respond to a substrate of density s. The equations governing the dynamics are of the form

$$\begin{aligned} \dot{s} &= -k(s)b + D\Delta s \\ \dot{b} &= -\nabla(b\chi(s)\nabla s) + \nabla(\mu(s)\nabla b). \end{aligned} \tag{1.2}$$

The first of equations (1.2) is purely phenomenological: it takes into account the diffusion of the substrate ($D\Delta s$) and the rate at which the substrate is consumed by the bacteria ($k(s)b$). The second equation is derived from a simple model of Brownian motion with chemotaxis [74]: the last term on the right side represents the diffusion while the first term is the chemotactic response of the bacteria to the gradient of the substrate concentration. By choosing appropriate initial and boundary conditions, the authors were able to find a rather good agreement between their theoretical results and the experimental ones (e.g. regarding the speed of the bands).

[1] It is indeed remarkable how such small organisms can be sensitive to gradients of chemicals on much larger scales and scientists are putting a lot of effort in trying to understand in depth the underlying mechanism(s) [136, 38, 29, 69, 26].

[2] Here we consider the motion of bacteria such as *E. coli*, which can self-propel in liquid or semisolid (e.g. soft agar gel) environments thanks to their flagella [12]. More details on *E. coli* motion are given in the next chapter.

Formation of diverse patterns has been observed in several experiments on *Salmonella typhimurium* and *Escherichia coli* in different environmental conditions. Consequently, phenomenological variations of chemotactic models have been formulated, using a combination of ad hoc parameters – and functions – and experimentally measured ones [145, 146, 20, 154]. Once again linear analysis is the tool used to predict the type of instability and indeed the striking similarities between the patterns simulated and experimentally observed suggest that the models could capture at least some important features of the underlying mechanism. However, we stress the fact that pattern matching should be considered more as a proof of concept than as an actual identification of the correct model.

To study how general or system-dependent these mechanisms are, more rigorous derivations of the macroscopic equations of chemotactic bacteria have been obtained [123, 122] using the tools of statistical physics. Statistical physics indeed plays a major role in trying to fill the gap between the micro and the macro worlds: understanding how the cells collectively move involves understanding how they individually respond to the environment and its fluctuations and how they interact with each other.

Constructing more rigorous mesoscopic models is possible in situations in which we have access to (some of) the microscopic details. Turing patterns are very difficult to observe in biological systems because the potential morphogens responsible for their emergence are molecules and chemicals which are not easy to track and observe. Moreover, this model is based on reasonable but rather arbitrary assumptions and it was formulated without any real biological proof. In the case of chemotactic bacteria, instead, theory and experiments have gone along since the beginning and one has inspired and completed the other.

1.2.3 Quorum sensing

Bacteria can perform tasks other than detecting gradients of nutrients, for example they are able to detect[3] concentrations of chemicals. In particular, they can synthesize, release, and detect small molecules – called autoinducers – whose concentration ("quorum") acts as a signal for an individual cell to communicate with the whole population, allowing the cell to coordinate its gene expression according to the population density [95, 56]. Collective behaviour can then be attained.

[3] We stress that the processes we indicate with the term "detection" must not be thought of as active processes: it merely indicates the passive absorption of some molecules by the cell and the integration of such molecules into the cell's biochemical machinery. The probability of "detecting" a molecule is proportional to the concentration of these molecules in the environment.

A well-known example of bacteria collective self-organization is the formation of biofilms, i.e. dynamical heterogeneous structures that grow near surfaces[4] (see fig. 1.3-Left). Compared to morphogenesis and developmental biology, the study of biofilm formation is a more recent field, due to the fact that bacteria have historically been regarded as individual cells not capable of interesting social behaviours [32].

Despite a simpler context, it remains very difficult to understand what are the main factors that influence the formation and the structure of biofilms. Quorum sensing in particular seems to be a relevant communication mechanisms (see [105] and references therein). It is often not clear, however, what are the relative contributions of genetics, physics, and chemistry, for instance in the investigation of biofilm development [125]. Once again, theoretical models are very useful to decipher – and one day maybe design – biofilms. However, due to the complexity and the large range of scales present in the problem, full-scale biofilm models are still missing [148, 62].

Another example of bacterial patterns and structure formation, where quorum sensing plays an important role, is their ability to organize into macroscopic motile structures (see [35] and references therein): among the other molecules, bacteria can produce surfactants (substances that lower the surface tension) which can allow them to move as a macroscopic organism and colonize a surface much more rapidly than they could do as individual cells (see fig. 1.3-Right). A phenomenological model involving partial differential reaction-diffusion equations describing the dynamics of the density of the bacteria, of the nutrients, and of other substances produced by the cells was proposed in [93] that qualitatively reproduces the dendritic patterns observed. However, the model is very system-specific and many important details are not taken into account, such as wetting phenomena or the motion of single bacteria.

1.3 Inducing patterns with synthetic biology

Collective behaviours *in vivo* and natural pattern formation are the result of the interplay of many different factors: biological factors (the struggle to survive, the search for nutrients and the colony growth), chemical factors (the interaction and communication via chemical substances), and physical ones (steric or hydrodynamic interactions, environment properties). Moreover, we have seen in the previous sections the importance of bridging the gap between experimental observations and theory to make progress. Nevertheless, because of their complexity, modelling these processes is very hard and often incomplete.

[4] Biofilms are usually described in opposition to planktonic cultures, where instead of sticking to a surface, bacteria float freely in the environment.

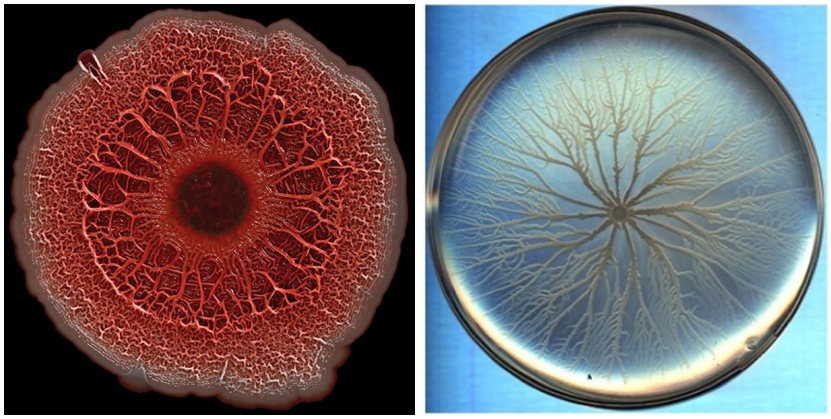

Figure 1.3 – Left: *Pseudomonas aeruginosa* biofilm, picture by Scott Chimileski and Roberto Kolter, Harvard Medical School, Boston. **Right**: Dendritic profiles for *Bacillus subtilis*, reprinted from [93].

To better understand which underlying mechanisms can trigger pattern formation, an alternative strategy is to work in well controlled environments, where interactions can be carefully designed and tuned. Synthetic biology provides the tools to implement this strategy (see [89, 99] for reviews on the different implementations and applications): by introducing synthetically designed plasmids[5] inside the cells, or by integrating designed DNA sequences directly into chromosomal DNA, it is possible to actively manipulate the genetic circuit of bacteria in order to obtain the desired effect or behaviour. The main advantage of working with genetically engineered cells is the possibility to control many different aspects of bacterial behaviour such as the mechanisms for intracellular communication or the role of the presence of specific genes and molecules both at microscopic and macroscopic scales.

In the study of pattern formation, different approaches are possible. First, synthetic biology can be used to try and generate patterning systems: bacteria can be engineered in such a way that they respond to specific and well controlled stimuli. The external stimuli act as a prepattern[6]: it can be a morphogen gradient [7, 81] or, e.g., light [138] at which bacteria adapt. The ability to program cellular patterns has the potential application of designing new techniques to control spatial organization of biomaterials [81]. A second approach, more investigative and less applied, is to use synthetic biology to try to decode design principles of pattern formation: in these case the manipulation does not aim at creating the pattern directly, but rather at testing mechanisms that could underlie them and which would be too hard to observe in *in vivo* conditions [106, 118, 21].

[5] Plasmids are small DNA molecules, separated from the chromosomal DNA, that are replicated and whose genes can be expressed independently.

[6] Here the term prepattern indicated a pattern formed by some molecules or chemicals. Cells are then stimulated by these chemicals to move or differentiate following the spatial organization of the prepattern.

Quorum sensing systems provide a very useful tool to engineer interactions in bacterial colonies. Coupling the sensory system to the regulation of the desired gene expression gives rise to density-dependent effects. The next two chapters are dedicated to the study of bacterial colonies with density-dependent motility. We will show how this particular type of interactions, together with the competition for nutrient resources, can lead to the formation of robust patterns.

Chapter 2

Pattern formation in single-species bacterial colonies

2.1 Introduction

This chapter is dedicated to the study of pattern formation in single-species bacterial colonies based on the interplay between the motility-induced phase separation (MIPS) and the population dynamics of the cells. A phenomenological model for pattern formation based on this interplay was formulated by Cates *et al.* in 2010 [23]. Shortly after Liu *et al.* [90] realized experiments involving engineered *Escherichia coli* capable of forming patterns very similar to the ones observed in [23]. The connection between these two works has remained elusive so far, and the topic of debate [49].

In the introductory part we recap the ideas and the results of the two papers, while in sections 2.2 and 2.3 we develop a theoretical model which, by taking into account experimentally relevant details, makes a direct connection between MIPS and the results obtained in [90].

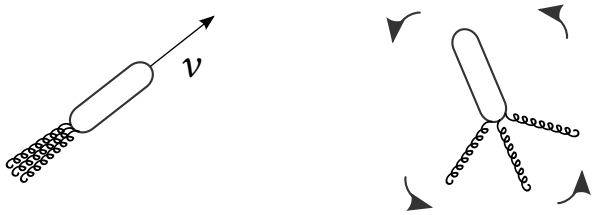

Figure 2.1 – Schematic representation of *E. coli*. **Left**: run. **Right**: tumble.

2.1.1 A model for pattern formation

2.1.1.1 Run-and-tumble dynamics

To begin with, we present the run-and-tumble model used to describe *Escherichia coli*'s dynamics. It is important to note that this model is a phenomenological description resulting from experimental observations [13]. It completely ignores the underlying biochemical machinery, which has also been well characterized [11].

E. coli is a flagellated bacterium able to self-propel by performing a series of runs and tumbles. During a run all the flagella rotate in the same direction (counter-clockwise, CCW) and form a bundle. The cell then moves persistently at speed v, assumed constant, and Brownian reorientation is small and usually neglected [22]. To change direction of motion the bacterium performs a tumble, during which one or more flagella starts rotating in the opposite direction (clockwise, CW). This causes the bundle of flagella to break and the cell's position remains roughly constant while its orientation changes rapidly. Note that this is an active reorientation and not solely the product of rotational diffusion.

As explained in section 1.2.2, the distributions of the durations of the run and tumble events are exponential. We assume the switching rates from one state to the other to be constant in time. We call α the tumbling rate and β the *running* rate, i.e. the rate at which a tumbling cell resumes running. For wild-type *E. coli*, these rates correspond to a mean run duration approximately 10 times larger than the mean tumble duration [13, 3], so that tumbles are often approximated as instantaneous events [122, 22, 18].

In run-and-tumble models, bacteria are persistent random walkers whose diffusion coefficient is much larger than the one of a regular passive Brownian particle of the same size (say, a dead bacterium) [22]. The diffusivity can be computed as

$$D \sim \frac{v^2}{d\alpha}, \tag{2.1}$$

where d is the number of spatial dimensions [12]. Note that (2.1) takes into account instantaneous tumbles.

2.1.1.2 Motility-induced phase separation

Motility-induced phase separation (MIPS[1]) is a process during which a system of active particles undergoes a change of state: the density of the system evolves from initially homogeneous to phase separated, with regions of high density and slowly moving particles

[1] See [25] for a review.

(liquid or even solid) and regions of low density and fast moving particles (gas). MIPS occurs in active systems in which the speeds of individual self-propelled particles decrease sufficiently fast as the local particle density increases. This effect results from the following feedback loop:

1. self-propelled particles accumulate where they go slower;

2. due to interactions, the particles' speeds decrease in high density regions.

The first condition is a property of self-propelled particles, whose steady-state probability density does not follow the Boltzmann distribution $p_{\text{eq}} \propto \exp\left(-\frac{H}{k_B T}\right)$ (where H is the hamiltonian of the system, k_B the Boltzmann constant and T the temperature). For these systems the steady-state probability $p_{\text{n-eq}}$ is instead proportional to the inverse of the speed. This fact can be seen by writing down the master equation for the single particle probability density $P(\mathbf{r}, \mathbf{u}, t)$ of finding the particle at position $\mathbf{r}$ with orientation $\mathbf{u}$ and at time t. For a particle with spatially varying speed $v(\mathbf{r})$ the master equation reads

$$\dot{P}(\mathbf{r}, \mathbf{u}, t) = -\nabla \cdot [v(\mathbf{r})\mathbf{u}P(\mathbf{r}, \mathbf{u})] + \Theta[P(\mathbf{r}, \mathbf{u})], \tag{2.2}$$

where $\Theta[P]$ accounts for an isotropic particle reorientation, due for instance to Brownian rotational diffusion or to tumbling events. If the steady-state probability is proportional to the inverse of the speed, $P_{\text{ss}} \propto 1/v(\mathbf{r})$, the isotropic reorientation terms vanish and Eq. (2.2) is always satisfied.

The second condition closes the feedback loop: suppose that the particle density becomes non-homogeneous, due, for instance, to random fluctuations. If in regions of high density the speed decreases sufficiently fast, due to some interactions, then in these regions there can be a further increase of density, which leads to a linear instability.

If no other dynamics compete with MIPS, the system then undergoes complete phase separation between two different coexisting densities ρ_H (high) and ρ_L (low) [141]: this happens through a process called *coarsening*. In practice, small droplets disappear and large domains become even larger in a process reminiscent of Ostwald ripening (see Fig. 2.2). In equilibrium systems, the reason for which coarsening occurs is the tendency of the system to decrease the contact line between the coexisting densities in order to minimize the energetically costly surface tension between them [107]. In section 2.2.2.1, we show that in non-equilibrium systems such as bacterial colonies, surface tension terms can arise from the non-locality of the interactions.

This mechanism was first introduced by Tailleur and Cates [139] for run-and-tumble particles with instantaneous tumbles and quorum sensing interactions, in one-dimensional space. Here we present the general model in d dimensions derived in subsequent

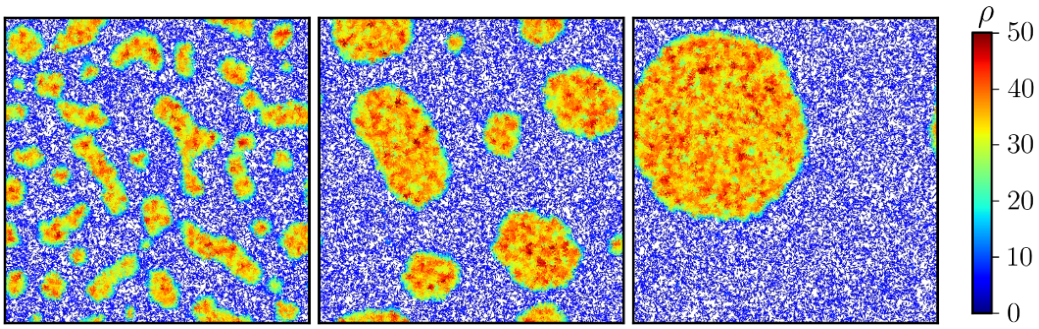

Figure 2.2 – Snapshots of motility-induced phase separation in a system of run-and-tumble particles. Reproduced from [132].

works [24, 132]. The idea is to start from the master equation for a single run-and-tumble particle with a spatially varying speed $v(\mathbf{r})$:

$$\dot{P}(\mathbf{r},\mathbf{u},t) = -\nabla\cdot[v(\mathbf{r})\mathbf{u}P(\mathbf{r},\mathbf{u})] - \alpha P(\mathbf{r},\mathbf{u}) + \frac{\alpha}{\Omega}\int \mathrm{d}\Omega' P(\mathbf{r},\mathbf{u}'), \tag{2.3}$$

where $\mathbf{r}$ is the position of the particle at time t, $\mathbf{u}$ is the unit vector indicating the orientation of the particle and tumbles are instantaneous. A coarse-graining procedure [132] then leads to a macroscopic partial differential equation for the single-body probability density in real space $C(\mathbf{r},t)$:

$$\dot{C}(\mathbf{r},t) = \nabla\cdot[D(\mathbf{r})\nabla C - \mathbf{V}(\mathbf{r})C] \quad \text{with} \quad D(\mathbf{r}) = \frac{v(\mathbf{r})^2}{d\alpha}, \quad \mathbf{V}(\mathbf{r}) = -\frac{v(\mathbf{r})\nabla v(\mathbf{r})}{d\alpha}. \tag{2.4}$$

The diffusivity D has the usual form of (2.1), but it is now a function of the spatial coordinate. The force-like term $\mathbf{V}$ is also a function of space and it emerges from non-constant $v(\mathbf{r})$. Note that α does not generate a drift. One then *assumes*[2] that Eq. (2.4) remains valid if v is a function of $\mathbf{r}$ through the N-body density field $\rho(\mathbf{r})$, which is assumed to evolve on much larger timescales, leading, at mean-field level, to

$$\dot{\rho}(\mathbf{r},t) = \nabla\cdot\left[D(\rho)\nabla\rho - \mathbf{V}(\rho)\rho\right] \quad \text{with} \quad D(\rho) = \frac{v(\rho)^2}{d\alpha}, \quad \mathbf{V}(\rho) = -\frac{v(\rho)\nabla v(\rho)}{d\alpha}. \tag{2.5}$$

If we rewrite the expression of $\mathbf{V}(\rho)$ as

$$\mathbf{V}(\rho) = -\frac{v(\rho)v'(\rho)}{d\alpha}\nabla\rho, \tag{2.6}$$

[2]Note that this assumption was never proven. It will be justified in section 2.2.1.

then Eq. (2.5) can be expressed as a standard diffusion equation

$$\dot{\rho}(\mathbf{r},t) = \nabla \cdot \left[D_{\text{eff}} \nabla \rho \right] \quad \text{with} \quad D_{\text{eff}} = D(\rho) + \rho \frac{D'(\rho)}{2}. \tag{2.7}$$

D_{eff} can turn negative when $v(\rho)$ decreases sufficiently fast:

$$\frac{v'(\rho)}{v(\rho)} < -\frac{1}{\rho}. \tag{2.8}$$

Then, small perturbations around the homogeneous solution $\rho(\mathbf{r}) = \rho_0$ can grow, which drives the system towards a phase-separated state with two coexisting densities. In this case, the interface between the two densities must be stabilized by higher order gradients that have been neglected in the derivation of Eq. (2.5).

2.1.1.3 Logistic growth

The first requirement for the formation of patterns, as introduced in section 1.2, is some kind of instability that breaks the translational invariance of the initially homogeneous state. In a colony of run-and-tumble bacteria interacting via quorum sensing this requirement can be fulfilled by the mechanism just described, namely by considering a negative effective diffusivity ($D_{\text{eff}} < 0$). This mechanism alone, however, cannot generate patterns: the steady state corresponds in fact to a complete phase separation with a dense and a dilute region composed of slow and fast particles respectively [141] (see Fig. 2.2). To obtain patterns further ingredients must be considered.

In section 1.2.2, we have seen how bacteria are able to explore the space by self-propelling in search of nutrient-rich regions. When they are in favourable conditions they are able to replicate by cell division [60], while they die – or rather become dormant, i.e. non-functional [78] – when they find themselves in starving conditions. Mathematically, this population dynamics is often modelled by a logistic equation for the density field [100]:

$$\dot{\rho} = \mu\rho\left(1 - \frac{\rho}{\rho_0}\right). \tag{2.9}$$

Here μ is the division rate of bacteria; it controls the typical timescale at which the system reaches the steady state where $\rho = \rho_0$, the carrying capacity. This value represents the target density: when $\rho < \rho_0$ (low competition, therefore favourable conditions) the population of active bacteria grows while when $\rho > \rho_0$ (high competition, therefore starving conditions) it decays.

This phenomenological formulation of the division and death dynamics is used by Cates *et al.* [23] to model the growth of a population of run-and-tumble particles with

density-dependent speed. They show that the coarsening observed in regular MIPS is in this case arrested and that the system self-organizes in arrays of regularly spaced dots or concentric rings (depending whether the initial density is homogeneous or a central inoculum). The complete phenomenological equation to model the density dynamics reads

$$\dot{\rho} = \nabla \cdot \left[D[\rho] \nabla \rho - \mathbf{V}[\rho] \rho \right] + \mu \rho \left(1 - \frac{\rho}{\rho_0} \right) - \kappa \Delta^2 \rho. \tag{2.10}$$

The last term proportional to the laplacian square is added to stabilize the interfaces during phase-separation. In [23], $\kappa > 0$ and its origin is purely phenomenological, but, as we show in section 2.2.2.1, it can be derived from a microscopic dynamics – in this case a function of the microscopic parameters v and α – by considering a slightly non-local coarse-grained density and approximating it by a gradient expansion.

The handwaving explanation of why the birth-and-death dynamics arrests the coarsening is that the two dynamics are in competition: while the mechanism of MIPS drives the system towards a non-homogeneous steady state with two coexisting densities, the logistic dynamics tends to homogenize the density around the constant value ρ_0. More specifically, we can consider the flux ϕ of bacteria through an interface between a droplet of density ρ_H and the surrounding environment at density ρ_L. The mass exchange between ρ_H and ρ_L, due to the bacteria's motility, is proportional to the length of the interface, and hence to the radius of the droplet. On the other hand, the mass variation inside the droplet, due to the birth and death events, is proportional to the area of the droplet, thus to the radius squared. At steady state the two contributions must balance and a characteristic length for the radius of the droplet – or, equivalently, for the width of a stripe or of a ring – is selected: the coarsening is arrested. The results of a simulation of Eq. (2.10) with the initial density following a gaussian distribution are shown in the top panel of Fig. 2.3 (taken from [23]).

2.1.2 Experimental realizations

The model described in section 2.1.1 has been shown to give rise to stable two-dimensional patterns [23]. Tackling the question whether the mechanism can produce the same results in real bacterial colonies requires being able to control the speed v of the bacteria as a function of their density ρ.

Liu *et al.* [90] constructed a genetic circuit to control the motility of *E. coli* as a function of their density; a schematic representation of the circuit is shown in Fig. 2.4. A

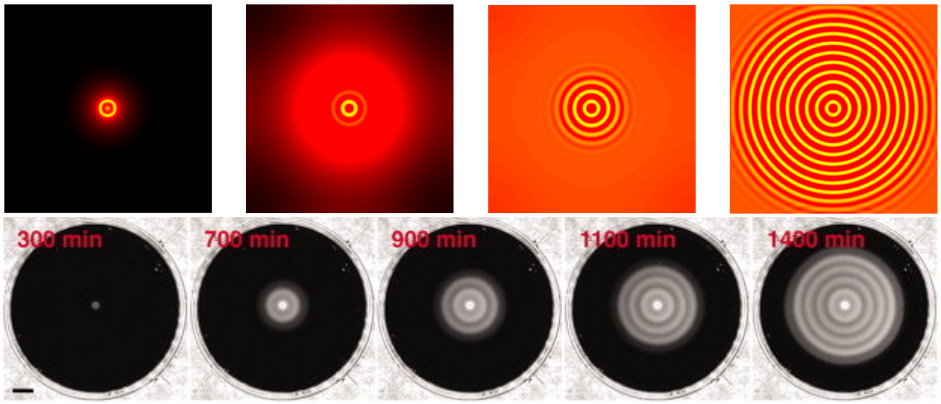

Figure 2.3 – Top: Dynamics of formation of patterns in 2D, starting from a single small bacterial droplet in the middle of the simulation sample. Simulation parameters in [23]. **Bottom**: Time-lapsed photographs of typical patterns obtained for the engineered strain. Experimental data in [90].

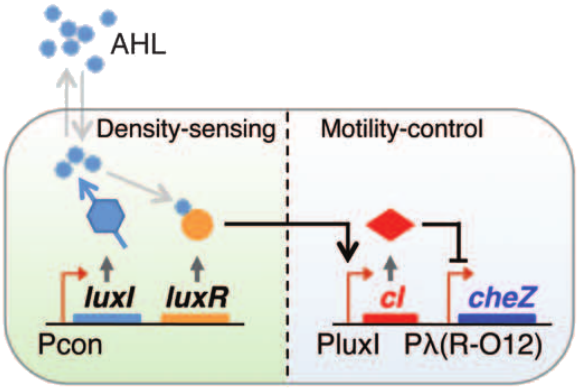

Figure 2.4 – Genetic circuit that couples the cell's motility to the density (reproduced from [90]).

"density-sensing module" synthesizes and excretes the autoinducer acyl-homoserine lactone (AHL). At high AHL concentration (hence high cell density) a "motility-control module" represses the transcription of the gene *cheZ*. When expressed, this gene encodes a phosphatase called CheZ, which accelerates the dephosphorylation of phosphorylated CheY (CheY-P). CheY-P is responsible for changing the direction of flagellar rotation from CCW to CW: its presence favours tumbling over running [15]. CheZ deletion therefore leads to an increase of CheY-P concentration, causing the cell to tumble incessantly [152, 115, 128]. The result is that at high densities the cells are less motile – because their tumble duration becomes large with respect to the run duration – while at low density they perform the regular run-and-tumble motion.

Liu *et al.* then inoculated a droplet containing the mutant strain depicted in Fig. 2.4 in the center of a petri dish containing semisolid agar. This is a gel whose pores are large

enough that bacteria can swim *in* the gel, but dense enough that convection of the solvent (water), and hence hydrodynamic interactions, are negligible. If the medium provides a sufficient amount of nutrients the bacteria are able to replicate, making the total population grow. Instead of expanding homogeneously[3], the colony self-organizes in a series of high and low density concentric rings, very reminiscent of the simulation of [23], as shown in the bottom panel of Fig. 2.3.

Although numerical and experimental results look very much alike (cf. Fig. 2.3), there are some important gaps between the theoretical model and the experiments. Firstly, there are technical issues which prevent the establishment of robust quantitative connections between theory and experiments. From the experimental point of view, only the cell density can be measured (by the means of a constitutively expressed fluorescent molecule and Continuous-Fluorescence-Photobleaching methods [88]). It is however much more complicated to track and measure the concentration of smaller molecules (AHL, CheZ, the agar medium), which would provide information about the interactions. Ideally, were these concentrations controllable, they could be used as a parameter to tune the strength of interactions, and hence sample the space of control parameters. From the point of view of the theory and numerical simulations, it is very easy to control these interactions, which are basically set manually, while a lot of (potentially important) experimental details are completely ignored (such as the presence of non-motile cells, the interactions with the agar gel, the concentration of nutrients, etc.). Indeed, it is the goal of a good model to retain only the fundamental ingredients; nevertheless, this often comes at the price of losing the possibility to establish quantitative connections with the experiments.

Another gap, more conceptual, between the works presented in [23] and [90] lies in the difference in the regulation of the bacterial motility by the density. While in the former the density controls the speed of the particle, in the latter the density controls the tumble duration. The final result of both strategies is to decrease the efficiency of transport when the density becomes large. The consequent phase separation is a signature of the non-equilibriumness of the systems that we are analysing. Kinetic parameters are in fact irrelevant in equilibrium systems, where the steady state distribution is solely determined

[3] In the context of population dynamics, the spread of a diffusing and reproducing population is described by the Fisher-KPP equation [48]:

$$\dot{\rho} = D\Delta\rho + \mu\rho\left(1 - \frac{\rho}{\rho_0}\right). \tag{2.11}$$

Starting from a central inoculum, the solution is a traveling front moving at speed $c = 2\sqrt{\mu D}$. A colony of wild-type *E. coli*, incapable of controlling their motility, inoculated in semisolid agar indeed expands homogeneously, qualitatively following the solution of (2.11) [90].

by thermodynamic quantities such as temperature, pressure, etc. In non-equilibrium systems, however, the role of kinetic parameters is unknown and no general theory has ever been formulated[4]. Consider for instance a system of bacteria with instantaneous tumbles, where now the tumbling rate can vary with the density, while the speed of bacteria is constant: $\alpha = \alpha(\rho)$ and $v = v_0$. In this case, the dynamics cannot lead to a density accumulation, and hence no phase separation can occur, as discussed in detail in section 2.2.2, page 35. This example shows that, at macroscopic scales, different kinetic parameters can play different roles, which cannot be deduced *a priori*. There is therefore no guarantee that considering a density-modulated speed in a system of instantaneously tumbling particles yields the same result as considering a density-modulated tumbling duration in a system of particles with finite tumble duration. In the following, we construct a model in which the finite duration of tumbles is taken into account and we show that in this case MIPS can emerge via the modulations of motility parameters other than the speed. In particular, a model in which the density modulates the tumble duration represent a more direct connection with the experiments of [90].

Section 2.2 is dedicated to the derivation of a macroscopic partial differential equation akin to Eq. (2.5), but which takes into account finite tumble duration. Moreover, we present a generalized coarse-graining procedure, which takes into account the interactions between particles from the beginning. Unlike previous derivations [139, 24, 132], which start from a non-interacting single-body problem and then assume that the results hold when considering a many-body system with interactions, our procedure overcomes the need of formulating such assumptions, as we explain in section 2.2.1.2. We then present a linear analysis of the equation we obtain, showing the role played by the finite tumble duration, and we validate our results with numerical simulations. Then, in section 2.3 we present the complete theory, and corresponding numerical simulations, for pattern formation.

2.2 The role of finite tumble duration

The finite duration of tumbling events has been investigated previously in, e.g., the study of jamming of two particles [129] or to explore its role in chemotaxis [69, 116]. Here we show how its regulation by the local density affects the motility of the cells and under which conditions it gives rise to MIPS and, once coupled with the logistic growth of the colony, to patterns.

[4] It is indeed likely that no such theory can even exist, non-equilibirum systems being out-of-equilibrium in many different ways, so that there cannot be a universal model able to describe them.

2.2.1 Coarse-graining procedure

In this section we present a coarse-graining procedure that allows us to obtain, by eliminating the appropriate degrees of freedom, a macroscopic description of the dynamics of run-and-tumble bacteria with finite tumble duration.

To model the run-tumble-stop dynamics explicitly, we assume that each bacterium can be in one of the two following dynamical states: a running state, during which it moves in a well defined direction, and a tumbling state, during which its position is fixed. When the bacterium resumes running, it does so with a new orientation, drawn from a uniform distribution. We note N the total number of bacteria. For each particle ℓ, the motility parameters v_ℓ (the speed), α_ℓ (the tumbling rate) and β_ℓ (the running rate) are functions of the positions of all particles, e.g. $v_\ell = v_\ell(\{\mathbf{r}_n\})$, where $\{\mathbf{r}_n\} \equiv \mathbf{r}_1, \mathbf{r}_2, \ldots, \mathbf{r}_N$.

To distinguish a running bacterium from a tumbling one we introduce a discrete degree of freedom (the dynamical state): $\sigma_\ell = 0, 1$ for the tumbling and running states, respectively. We call $P = P(\{\mathbf{r}_n, \theta_n, \sigma_n\}, t)$ the joint probability of the configuration $\{\mathbf{r}_n, \theta_n, \sigma_n\}$ (position, orientation and dynamical state) for the colony. The master equation then reads:

$$\begin{aligned}\dot{P}(\{\mathbf{r}_n, \theta_n, \sigma_n\}, t) = &\sum_{\ell=1}^{N} \sigma_\ell \left[-\nabla_\ell \cdot (v_\ell \mathbf{u}_{\theta_\ell} P) - \alpha_\ell P + \frac{\beta_\ell}{2\pi} \int \mathrm{d}\theta'_\ell P_{\sigma_\ell=0} \right] \\ &+ \sum_{\ell=1}^{N} (1 - \sigma_\ell) \left[-\beta_\ell P + \alpha_\ell P_{\sigma_\ell=1} \right]\end{aligned} \tag{2.12}$$

Here $P_{\sigma_\ell=1}$ and $P_{\sigma_\ell=0}$ correspond to $P(\{\mathbf{r}_n, \theta_n, \sigma_n\})$ but in which the value of the variable σ_ℓ has been fixed to 1 or 0. The first sum (first line) in Eq. (2.12) takes into account the dynamics of running bacteria: the first term is due to the flux of probability ($\mathbf{u}_{\theta_\ell}$ is the unit vector in the direction θ_ℓ), the second is a loss term due to particles that stop running to enter a tumbling state while the third is a gain term due to particles that stop tumbling and start running in direction θ_ℓ. The second sum (second line) takes into account the dynamics of tumbling bacteria: the loss term is due to particles that switch from tumbling to running (in a new random direction) while the gain term is due to particles switching from running to tumbling.

The coarse-graining procedure is divided into two parts, detailed in sections 2.2.1.1 and 2.2.1.2. In the first one we integrate out the degrees of freedom $\{\sigma_n\}$ and $\{\theta_n\}$ that describe the dynamical states and the orientations of all particles. By using a fast variable approximation and a truncated gradient expansion we obtain the dynamics for the joint probability density $C_0(\{\mathbf{r}_n\}, t)$ of the positions of all the particles, which obeys a Fokker-Planck equation. In the second part of the procedure we use Itō calculus (following [39, 139]) to go from the Fokker-Planck equation for the probability density $C_0(\{\mathbf{r}_n\}, t)$ to a

stochastic partial differential equation for the N-particles density field $\rho(\mathbf{r},t) = \sum_i \delta(\mathbf{r} - \mathbf{r}_i(t))$.

2.2.1.1 Diffusion-drift approximation

The two degrees of freedom that have to be integrated out when passing from the microscopic to mesoscopic scales are the orientations of the particles and their dynamical states. The latter is a discrete variable and therefore, in order to eliminate it, we can simply sum over its possible values: $\sigma_\ell = 0, 1$. On the other hand, in order to eliminate the angular dependence $\{\theta_n\}$ from our dynamics, we express the joint probability P in a "joint" Fourier basis: $\{\exp\left(i\sum_{j=1}^N k_j\theta_j\right)\}$, which takes into account the orientation of all the particles, and then project the master equation on this basis. The use of this generalized 2-dimensional Fourier basis instead of a generalized d-dimensional basis of spherical harmonics is justified by assuming that we consider an almost 2D system: all bacteria are assumed to swim in a plane and their directions are defined by only one angle: $\mathbf{u}_{\theta_\ell} = (\cos\theta_\ell, \sin\theta_\ell)$. This assumption, although not completely faithful to the experiments (we know that in the experiments bacteria swim in 3D inside the agar gel), greatly simplifies the calculations and gives results which are in qualitative agreement with the experimental observations; extending the computation to 3D is doable but would only alter quantitatively the results.

We thus express P in the joint Fourier basis:

$$P(\{\mathbf{r}_n, \theta_n, \sigma_n\}) = (2\pi)^{-N} \sum_{\{k_n\}} c_{k_1 \dots k_N}(\{\mathbf{r}_n, \sigma_n\}) \exp\left(i \sum_{j=1}^N k_j \theta_j\right). \tag{2.13}$$

In the following we use the notation:

$$\begin{aligned} C_0 &= c_{k_1=0 \dots k_N=0} \\ C_{\pm\ell} &= c_{k_1=0 \dots k_\ell=\pm1 \dots k_N=0} \\ C_{\pm2\ell} &= c_{k_1=0 \dots k_\ell=\pm2 \dots k_N=0} \\ C_{\pm\ell\pm m} &= c_{k_1=0 \dots k_\ell=\pm1 \dots k_m=\pm1 \dots k_N=0} \\ &\dots \end{aligned} \tag{2.14}$$

We call these quantities moments: they are the components of P along the basis vectors

$$\{1, \exp(\pm i\theta_\ell), \exp(\pm 2i\theta_\ell), \exp(i(\pm\theta_\ell \pm \theta_m)), \dots\} \tag{2.15}$$

that we from now on refer to as "harmonics".

The dynamics of the moments (2.14), which are functions of the positions $\{\mathbf{r}_n\}$ and the dynamical states $\{\sigma_n\}$ of all the particles, but not of their orientations $\{\theta_n\}$, can be obtained by projecting the master equation on the different harmonics:

$$\begin{aligned} &\langle 1, \dot{P}\rangle = \dot{C}_0 \\ &\langle \exp(\pm i\theta_\ell), \dot{P}\rangle = \dot{C}_{\mp\ell} \\ &\dots \end{aligned} \tag{2.16}$$

with

$$\langle f(\{\theta_n\}), g(\{\theta_n\})\rangle \equiv \int \mathrm{d}\theta_1 \dots \mathrm{d}\theta_N f(\{\theta_n\}) g(\{\theta_n\}) \tag{2.17}$$

the scalar product on our joint Fourier basis.

We are in particular interested in the dynamics of the zeroth moment C_0, i.e. the probability density in real space $\{\mathbf{r}_n\}$, since it is the only conserved quantity, or slow variable: its relaxation time diverges with the system size. Projection on the zeroth harmonic and sum over the $\{\sigma_n\}$ variables leads to the equation governing the evolution of the probability density $C_0(\{\mathbf{r}_n\}, t)$:

$$\dot{C}_0 = -\sum_\ell \nabla_\ell \cdot \left[\frac{v_\ell}{2} \left(C_{-\ell}^{\sigma_\ell=1} \begin{pmatrix} 1 \\ -i \end{pmatrix} + C_{+\ell}^{\sigma_\ell=1} \begin{pmatrix} 1 \\ i \end{pmatrix} \right) \right]. \tag{2.18}$$

The details of the derivation can be found in Appendix A.1.1. As we can see, Eq. (2.18) involves the higher modes $C_{\pm\ell}^{\sigma_\ell=1}(\{\mathbf{r}_n\}, t)$. Note that this notation with the superscript $\sigma_\ell = 1$ indicates that all variables $\{\sigma_{n\neq\ell}\}$ have been summed over, while σ_ℓ takes value 1. In practice, this notation indicates a moment where all particles are in any dynamical state (run or tumble), while particle ℓ is in a running state.

To obtain a closed equation involving only the probability density C_0 we need to express the modes $C_{\pm\ell}^{\sigma_\ell=1}$ in terms of C_0 and then re-inject them into Eq. (2.18). Unlike C_0, all the other higher modes are non-conserved – and hence fast – variables. Their relaxations indeed occur on timescales of the order of $t \sim 1/\alpha$: at a mesoscopic scale ($t \gg 1/\alpha$) their dynamics have relaxed, and one can therefore assume $\dot{C}_{\pm\ell} = \dot{C}_{\pm 2\ell} = \dot{C}_{\pm\ell\pm m} = \dots = 0$. This is a fast variable approximation. The expression for the moment $C_{\pm\ell}^{\sigma_\ell=1}$, whose derivation is again detailed in Appendix A.1.1, reads

$$C_{\pm\ell}^{\sigma_\ell=1} = -\frac{1}{\alpha_\ell} \nabla_\ell \cdot \left[\frac{v_\ell}{2} C_0^{\sigma_\ell=1} \begin{pmatrix} 1 \\ \mp i \end{pmatrix} \right] + \mathcal{O}\left(\nabla^3 C_0^{\sigma_\ell=1}\right). \tag{2.19}$$

Once injected in Eq. (2.18), it gives

$$\dot{C}_0 = \sum_\ell \nabla_\ell \cdot \left[\frac{v_\ell}{2\alpha_\ell} \nabla_\ell \left(v_\ell C_0^{\sigma_\ell=1} \right) \right] + \mathcal{O}\left(\nabla^4 C_0^{\sigma_\ell=1} \right). \tag{2.20}$$

We now assume that the probability density C_0 is slowly varying *in space* so that we neglect the gradient terms of higher order. We thus truncate our gradient expansion at order 2.

Finally, by studying the dynamics of $C_0^{\sigma_\ell=0}$ (see Appendix A.1.1), we can express $C_0^{\sigma_\ell=1}$ in terms of $C_0 = C_0^{\sigma_\ell=1} + C_0^{\sigma_\ell=0}$ and obtain a closed expression for the probability density evolution:

$$\dot{C}_0 = \sum_\ell \nabla_\ell \cdot \left[\frac{v_\ell}{2\alpha_\ell} \nabla_\ell \left(\frac{v_\ell}{1+\frac{\alpha_\ell}{\beta_\ell}} C_0 \right) \right] = \sum_\ell \nabla_\ell \cdot \left(D_\ell \nabla_\ell C_0 - \mathbf{F}_\ell C_0 \right), \tag{2.21}$$

where

$$D_\ell = \frac{v_\ell^2}{2\alpha_\ell \left(1+\frac{\alpha_\ell}{\beta_\ell}\right)} \qquad \text{and} \qquad \mathbf{F}_\ell = -\frac{v_\ell}{2\alpha_\ell} \nabla_\ell \frac{v_\ell}{1+\frac{\alpha_\ell}{\beta_\ell}}. \tag{2.22}$$

The choice of the letters in Eq. (2.22) is not random: D_ℓ is the diffusion coefficient given by the usual $v^2/(2\alpha)$ [122] (the factor 2 in the denominator is due to the fact that we are operating in 2D), rescaled by the factor $(1+\alpha/\beta)^{-1}$, the fraction of time spent running. $\mathbf{F}_\ell$ is a drift term, which emerges from the gradient of some combination of the spatially-varying motility coefficients. Had we not considered space-dependent motility parameters, the dynamics at this mesoscopic scale would have been simple diffusion.

2.2.1.2 The role of interactions

As introduced in section 1.2.3, some bacteria – including the genetically modified *E. coli* studied in [90], which we are considering in this chapter as a model system – interact via quorum sensing: they are able to detect[5] the concentration of certain molecules (e.g. acyl-homoserine lactone, or AHL, in the experiments of [90]), secreted by all bacteria in the colony, and then modify their gene expression, depending on the detected concentration. In our case, the modification of gene expression results in a control of their motility.

At the beginning of section 2.2.1 we chose to make the motility parameters $v(\{\mathbf{r}_n\})$, $\alpha(\{\mathbf{r}_n\})$ and $\beta(\{\mathbf{r}_n\})$ depend on the position of all the particles. This choice can now be understood by noticing that each bacterium is surrounded by a gaussian cloud of AHL molecules – produced by the bacterium itself –, which move diffusively and eventually degradate. Hence, the motility parameters, which in the experiments are modulated by

[5] We recall that with the term "detection" we refer to the passive process of absorption of some molecules that then act on the bacterial biochemical machinery by enhancing or repressing gene expression.

the varying concentration of AHL, indirectly depend on the position of the particles. Then, it is perfectly legitimate to choose an appropriate function $f(\{\mathbf{r}_n\})$ for this dependence. In particular, we claim that a good approximation is to let f be the N-body density field of bacteria, defined as

$$\rho(\mathbf{r},t) = \sum_{i=1}^{N} \rho_i(\mathbf{r},t) = \sum_i \delta(\mathbf{r}-\mathbf{r}_i(t)), \tag{2.23}$$

where $\mathbf{r}_i(t)$ is the trajectory followed by particle i. We can then express the dependence of the motility parameters on the particles' positions through ρ, which gives

$$\begin{aligned} v_\ell(\{\mathbf{r}_n\}) &= v[\rho(\mathbf{r}_\ell)] \\ \alpha_\ell(\{\mathbf{r}_n\}) &= \alpha[\rho(\mathbf{r}_\ell)] \\ \beta_\ell(\{\mathbf{r}_n\}) &= \beta[\rho(\mathbf{r}_\ell)]. \end{aligned} \tag{2.24}$$

Microscopically, however, there are both a spatial and a temporal delay between the position and time at which AHL is produced and those at which it is sensed by another cell. Once the AHL molecules are sensed, the bacterial genetic machinery is activated and can then produce the proteins that control the motility. This adds a further delay in the response to the initial production of the molecule. To take these delays into account, the natural path would be to consider the presence of the AHL molecules as a concentration field mediating the interactions between cells. However, as we argued in section 2.1.2, we know that it will never be possible to make real quantitative connections between the model and the experiments. Increasing the complexity of the model by adding ingredients phenomenologically only makes the identification of basic mechanisms harder: any phenomenological fitting parameter introduced necessarily takes an arbitrary functional form, that may need to be adapted or fine tuned for different situations or setups, thus undermining our search for general principles.

We instead follow a different path, and assume that integrating out this extra field of molecules concentration leads to a non-local dependence of the motility parameters on the density field ρ: for instance, $v[\rho(\mathbf{r})]$ would become $v[\tilde{\rho}(\mathbf{r})]$ (the same holds for α and β), with

$$\tilde{\rho}(\mathbf{r},t) = \int \mathrm{d}\mathbf{y}\,\mathrm{d}s\, K(\mathbf{r}-\mathbf{y}, t-s)\rho(\mathbf{y},s). \tag{2.25}$$

This means that a bacterium at position $\mathbf{r}$ at time t feels the influence of bacteria that were at positions $\mathbf{y}$ at an earlier time s. Although it would be very interesting to study the effects of temporal delays, for practical purposes we neglect them in the following treatment: we therefore assume instantaneous interactions, so that $K = 0$ if $t \neq s$. In section 2.2.2.1 we

study the role of the spatial non-locality of the interactions, which we show to be important in phase-separating systems, when higher order gradients of the density stabilize the interfaces between coexisting densities.

2.2.1.3 Collective dynamics for the density field

To study the dynamics of the density field $\rho(\mathbf{r})$, we start by recasting the Fokker-Planck equation (2.21) into a Langevin process for each particle's trajectory. Basic Itō calculations [70] show the equivalence between a multivariate Fokker-Planck equation of the form

$$\dot{P}(\{\mathbf{r}_n\},t) = -\sum_\ell \nabla_\ell \left[\mathbf{f}[\tilde{\rho}(\mathbf{r}_\ell)]P - \nabla_\ell g[\tilde{\rho}(\mathbf{r}_\ell)]\,P\right] \tag{2.26}$$

and a system of N coupled Langevin equations of the form

$$\dot{\mathbf{r}}_\ell(t) = \mathbf{f}_\ell + \sqrt{2g_\ell}\,\boldsymbol{\eta}_\ell(t), \quad \langle \eta_i^\mu(t)\eta_j^\nu(t')\rangle = \delta_{\mu\nu}\delta_{ij}\delta(t-t'), \tag{2.27}$$

where we have simplified the notation by setting $\mathbf{f}_\ell = \mathbf{f}[\tilde{\rho}(\mathbf{r}_\ell)]$ and $g_\ell = g[\tilde{\rho}(\mathbf{r}_\ell)]$. We can then re-write Eq. (2.21) as

$$\dot{C}_0 = -\sum_\ell \nabla_\ell \cdot \left[\left(\frac{v_\ell}{1+\frac{\alpha_\ell}{\beta_\ell}}\nabla_\ell \frac{v_\ell}{2\alpha_\ell}\right)C_0 - \nabla_\ell\left(\frac{v_\ell^2}{2\alpha_\ell\left(1+\frac{\alpha_\ell}{\beta_\ell}\right)}C_0\right)\right] \tag{2.28}$$

which is equivalent to the system of Langevin equations (2.27) with

$$\mathbf{f}_\ell = \frac{v_\ell}{1+\frac{\alpha_\ell}{\beta_\ell}}\nabla_\ell \frac{v_\ell}{2\alpha_\ell} \quad \text{and} \quad g_\ell = \frac{v_\ell^2}{2\alpha_\ell\left(1+\frac{\alpha_\ell}{\beta_\ell}\right)}, \tag{2.29}$$

where we have adopted the Itō convention for the evaluation of the multiplicative noise, following [139, 70, 51].

Starting from Eq. (2.27), we use the properties of $\rho(\mathbf{r})$ and we derive in Appendix A.1.2 the many-body Langevin equation for ρ, which has the form

$$\begin{aligned} \dot{\rho}(\mathbf{r},t) &= \nabla\cdot\left[D[\tilde{\rho}]\nabla\rho - \mathbf{F}[\tilde{\rho}]\rho + \sqrt{2D[\tilde{\rho}]\rho}\,\boldsymbol{\Lambda}\right] \\ \Lambda_\mu(\mathbf{r},t)\Lambda_\nu(\mathbf{r}',t')\rangle &= \delta_{\mu\nu}\delta(\mathbf{r}-\mathbf{r}')\delta(t-t'). \end{aligned} \tag{2.30}$$

Here the formal expressions of D and $\mathbf{F}$ are those of (2.22), where the motility parameters are now functionals of the density field and ∇_ℓ has become simply ∇, the gradient with respect to the spatial variable $\mathbf{r}$. The last term is a noise term whose form cannot be chosen arbitrarily but must instead be derived from the run-and-tumble dynamics directly.

The multiplicative character of the noise is expected: the density cannot fluctuate when no particles are present [39]. To conclude, note that if the density is a slowly varying field, we can consider a gradient expansion of the coarse-grained density (2.25):

$$\begin{aligned}\tilde{\rho}(\mathbf{r}) &= \int d\mathbf{y}\, K(\mathbf{r}-\mathbf{y})\rho(\mathbf{y}) = \int d\mathbf{y}\, K(\mathbf{r})\rho(\mathbf{r}-\mathbf{y}) \\ &= \rho(\mathbf{r}) + \nabla\rho(\mathbf{r})\int d\mathbf{y}\, K(\mathbf{y})\mathbf{y} + \frac{1}{2}\Delta\rho(\mathbf{r})\int d\mathbf{y}\, K(\mathbf{y})\mathbf{y}^2 + \mathscr{O}\left(\nabla^3\rho(\mathbf{r})\right).\end{aligned} \tag{2.31}$$

Truncating the expansion at the second order in gradients and considering a symmetric kernel K, so that $\int d\mathbf{y}\, K(\mathbf{y})\mathbf{y} = 0$, gives

$$\tilde{\rho}(\mathbf{r}) = \rho(\mathbf{r}) + \frac{1}{2}\Delta\rho(\mathbf{r})\sigma^2, \tag{2.32}$$

where $\sigma^2 = \int d\mathbf{y}\, K(\mathbf{y})\mathbf{y}^2$. Re-injecting this result in the expressions for $D[\tilde{\rho}]$ and $\mathbf{F}[\tilde{\rho}]$ of Eq. (2.30) then yields

$$\dot{\rho}(\mathbf{r},t) = \nabla\cdot\left[D[\rho]\nabla\rho - \mathbf{F}[\rho]\rho + \sqrt{2D[\rho]\rho}\,\mathbf{\Lambda}\right] + h.o. \tag{2.33}$$

where the *h.o.* terms include gradients of order 4 and 6 (odd gradients vanish because of the choice of taking a symmetric function for the kernel K). Hence, from Eq. (2.33), we conclude that the effect of considering motility parameters that depend on a slightly non-local density $\tilde{\rho}(\mathbf{r})$, in the limit in which the density field $\rho(\mathbf{r})$ is a slowly varying function of $\mathbf{r}$, simply results in higher order gradient terms. We first neglect these higher order terms and discuss their role later in section 2.2.2.1.

2.2.2 Linear analysis

To study the phenomenology of the equation that we have derived, we perform a linear analysis of Eq. (2.33) around an homogeneous profile ρ_0. Note that in Eq. (2.33) the motility parameters have become simple functions of the density $h(\rho(\mathbf{r}))$. Spatial gradients are then treated with the standard chain rule: $\nabla h = \partial_\rho h \nabla\rho = h'\nabla\rho$.

Within a mean-field approximation, we neglect the noise and define the perturbed solution in Fourier space as

$$\rho(\mathbf{r}) = \rho_0 + \sum_q \delta\rho_q e^{i\mathbf{q}\cdot\mathbf{r}}. \tag{2.34}$$

The linearized equation then reads $\delta\dot{\rho}_q = -q^2 D_{\text{eff}}\delta\rho_q$, where

$$D_{\text{eff}} = D\left(1 + \rho_0\left[\log\frac{v}{1+\frac{\alpha}{\beta}}\right]'\right), \tag{2.35}$$

the prime indicates the derivative with respect to ρ and all the functions of ρ are evaluated at ρ_0. Here D is of the form (2.22). We have used here the same notation as the one introduced in Eq. (2.7). The form of D_{eff} is now more complicated, but the sole relevant ingredient is its sign: when $D_{\text{eff}} < 0$, perturbations grow triggering a phase separation, which happens when

$$\left[\log \frac{v}{1+\frac{\alpha}{\beta}}\right]' < -\frac{1}{\rho}. \tag{2.36}$$

To study the role of the different parameters, a simple strategy is to consider three separate cases, in each of which only one parameter among v, α, and β varies with the density.

In the first case we assume $v(\rho)$, while α and β are constants. Then $\alpha' = \beta' = 0$. In this case, the instability condition is exactly the same as in the case of a system with instantaneous tumbles (cf. Eq. (2.8)) and we recall it here:

$$\left[\log v\right]' = \frac{v'}{v} < -\frac{1}{\rho}. \tag{2.37}$$

This condition requires v to be a decreasing function of the density and it does not depend on the tumbling and running rates. We conclude that when the bacterial motility is modified through $v(\rho)$ and α and β are constant, the fact that the tumbles have finite duration only alters quantitatively the effective diffusivity – namely by rescaling it by a factor $(1+\alpha/\beta)^{-1}$ – but it does not play any role in the MIPS mechanism itself.

In the second case we assume $\alpha(\rho)$, while v and β are constants, so that $v' = \beta' = 0$. The instability condition then reads

$$\left[\log \frac{1}{\alpha+\beta}\right]' = -\frac{\alpha'}{\alpha+\beta} < -\frac{1}{\rho}. \tag{2.38}$$

This condition requires α to be an increasing function of the density: since $\alpha \sim \tau_{\text{r}}^{-1}$, the mean run duration decreases with the density, resulting in a reduced motility in highly populated regions. Note that a density-dependent tumbling rate $\alpha(\rho)$ leads to an instability only when the tumbles have a finite duration. For instantaneous tumbles, indeed, $\beta \to \infty$ and the condition (2.38) can never be satisfied. To understand why it is so, consider a run-and-tumble particle in 1D[6]. We assume that at time t the particle is at position $x \in (x_1, x_2)$, with $|x_1 - x_2| \ll v/\alpha$, the typical run length. If there is no tumbling event at time t, the particle performs a run and at time $t+\Delta t$ it has exited the interval (x_1, x_2), where Δt is such that $|x_1 - x_2| \ll v\Delta t \ll v/\alpha$. If instead a tumble occurs, we distinguish the two cases: if the tumble's duration is finite, at time $t+\Delta t$ the particle is still at position

[6] Generalization to $d > 1$ dimensions is straightforward.

$x \in (x_1, x_2)$; if the tumble is instantaneous, the particle simply reverses its direction of motion – since we are in 1D – and at time $t+\Delta t$ has exited the interval (x_1, x_2). Therefore there can be no effective accumulation due to density-modulated tumbling rate when tumbles are instantaneous.

Finally, we consider the case in which we assume $\beta(\rho)$, v and α constant, and therefore $v' = \alpha' = 0$. In this case the condition reads

$$\left[\log \frac{\beta}{\alpha+\beta}\right]' = \frac{\alpha\beta'}{\beta(\alpha+\beta)} < -\frac{1}{\rho} \tag{2.39}$$

and it requires β to be a decreasing function of ρ. This condition is of course only meaningful in the case of tumbles with finite duration. In section 2.1.2 we described the experiments performed on a colony of *E. coli* capable of modifying their tumble duration according to the local density. We are now able to relate, at least qualitatively, this experimental parameter to a theoretical one, i.e. the running rate β. Condition (2.39) is satisfied in the experiments described in [90], where the mean tumble duration $\tau_t = \beta^{-1}$ grows with the density in a step-wise manner. Note that, although the experiments correspond to the situation illustrated in the third case, with instability condition (2.39), the other two cases could potentially be relevant for different setups, where the quantities which are density-modulated are the speed or the tumbling rate.

2.2.2.1 Higher order gradients

In section 2.2.1.3 we have seen that a gradient expansion of the coarse-grained density $\tilde{\rho}$ leads to the equation of motion (2.33) involving the local density ρ – defined in (2.23). Because of this gradient expansion (2.31), terms of higher order in gradients appear. In particular, we choose to retain only terms until fourth order. Then, if we neglect the noise, within a mean-field approximation, and call $m_1 = \frac{v}{2\alpha}$ and $m_2 = \frac{v}{1+\alpha/\beta}$, Eq. (2.33) becomes

$$\begin{aligned}\dot{\rho}(\mathbf{r},t) = &\nabla\cdot\left[(m_1 m_2 + \rho m_1 m_2')\nabla\rho\right] \\ &+\nabla\cdot\left[\frac{1}{2}\sigma^2\Delta\rho\left[(m_1 m_2)' + \rho(m_1 m_2')'\right]\nabla\rho\right] \\ &+\nabla\cdot\left[\frac{1}{2}\sigma^2\rho m_1 m_2'\nabla\Delta\rho\right],\end{aligned} \tag{2.40}$$

where m_1 and m_2 are functions of ρ and the primes denote derivatives with respect to ρ. In the first line only gradients of order 2 appear: this line corresponds to a the local approximation of the coarse-grained density, considered in the previous linear analysis.

The terms appearing in the second and third lines are instead proportional to gradients of fourth order and correspond to taking into account a slightly non-local density.

We can linearize Eq. (2.40) to investigate the role of these higher order gradients, which determine the fate of the solution at small wavelengths (large q). We consider a small perturbation, like the one shown in Eq. (2.34), around a homogeneous profile ρ_0. Then, the terms appearing in the second line of Eq. (2.40) become negligible and the only fourth order contribution comes from the term in the third line. The linearized equation reads

$$\delta\dot{\rho}_q = (-q^2 D_{\text{eff}} + q^4\kappa)\,\delta\rho_q, \quad \text{with} \quad \kappa = \frac{1}{2}\sigma^2\rho D\left[\log\frac{v}{1+\frac{\alpha}{\beta}}\right]'. \tag{2.41}$$

The role of the term of order q^4 is determined by the sign of the coefficient κ. If κ is positive, the fourth order term is not stabilizing and higher order terms ($\mathcal{O}(q^6)$) are needed to saturate the instability. If instead κ is negative, its contribution stabilizes the solution at large q. We recall that the instability condition $D_{\text{eff}} < 0$ requires

$$\left[\log\frac{v}{1+\frac{\alpha}{\beta}}\right]' < -\frac{1}{\rho} < 0, \tag{2.42}$$

which thus yields $\kappa < 0$. In this case, the sign of D_{eff} determines the sign of κ. We conclude that the overall effect of the fourth order gradients is to stabilize the solution by saturating the instability at large q.

Some questions remain open: for instance, one could consider a system which is stable at small q, i.e. where $D_{\text{eff}} > 0$. This implies

$$\left[\log\frac{v}{1+\frac{\alpha}{\beta}}\right]' > -\frac{1}{\rho}. \tag{2.43}$$

The sign of κ is now independent on the sign of D_{eff}. One can have $\kappa < 0$ for

$$0 > \left[\log\frac{v}{1+\frac{\alpha}{\beta}}\right]' > -\frac{1}{\rho}, \tag{2.44}$$

as well as $\kappa > 0$ for

$$\left[\log\frac{v}{1+\frac{\alpha}{\beta}}\right]' > 0 > -\frac{1}{\rho}. \tag{2.45}$$

In the first case the solution is stable $\forall q$, while in the second case it is stable for small q and unstable for larger q. One therefore needs to analyse terms of higher orders (see

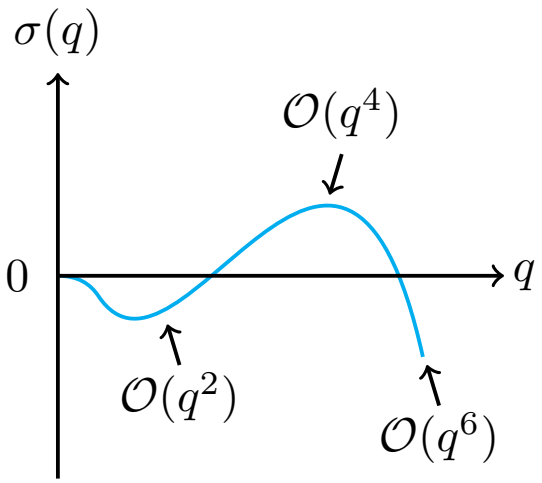

Figure 2.5 – Schematic representation of the growth rate as a function of q. Here the terms proportional to q^2 and q^6 are stabilizing, while the instability is caused by the terms of order q^4.

Fig. 2.5) and determine whether they can stabilize the solution. Looking for such an instability is left for future work.

In models like the one presented in [23], the contribution of the fourth order gradient terms is not derived from considerations on the microscopic interactions, but simply added as a phenomenological parameter required for the stability of the partial differential equation. In that case, κ is simply a positive constant and the equation governing the evolution of ρ reads

$$\dot{\rho} = \nabla \cdot \left[D_{\text{eff}} \nabla \rho \right] - \kappa \Delta^2 \rho. \tag{2.46}$$

Although simplified with respect to Eq. (2.40), Eq. (2.46) still contains the basic ingredients to observe a MIPS in the system, namely an instability given by $D_{\text{eff}} < 0$ and a saturation of such instability due to the term $-\kappa\Delta^2\rho$. Moreover, simulations of Eq. (2.46) are relatively easy to perform, while simulating the total Eq. (2.40) gives rise to stability problems. Since, in any case, Eq. (2.40) comes from an approximation and its form, in this sense, is not exact, we choose to use the simpler version (2.46) when performing numerical simulations (see section 2.3.1).

Note that in equilibrium, terms like $\kappa\Delta^2\rho$ stem from a free energy $\mathscr{F}_{\text{grad}} = \int dx \frac{\kappa}{2} (\nabla\rho)^2$. Here, the non-locality of the interactions hence generates an effective surface tension. This explains the coarsening seen in MIPS (cf. Fig. 2.2).

2.2.3 Numerical results: two types of microscopic simulations

In order to explore the fate of systems satisfying the linearly unstable conditions just derived, we can perform numerical simulations of microscopic models. Details about the numerical implementations are given in Appendix A.2.1. As we have done for the linear analysis in section 2.2.2, we consider three different cases where only one motility parameter varies with the density, while the other two are constant, and we choose their values in such a way that they satisfy the instability conditions (2.37), (2.38) and (2.39). The simulations show that the predicted phase separation occurs in the corresponding regimes (see Fig. 2.6). This result establishes a connection between the simple microscopic model we started from and the coarse-grained dynamics we obtained for the density field ρ, thus validating our coarse-graining procedure and the approximations carried out.

Fig. 2.6 shows that the coarsening dynamics for the three cases illustrated in section 2.2.2 are very similar (panels a, b and c). Some minor differences, e.g. in the coarsening timescale, the effective surface tension between dense and dilute regions or the value of the coexisting densities, are due to differences of the motility parameters chosen to satisfy the instability conditions (2.37), (2.38) and (2.39).

Off-lattice simulations (such as those whose results are shown in Fig. 2.6) are very computationally expensive. An alternative which is much more efficient is to consider on-lattice systems[7]. It is beyond the scope of our study to investigate the detailed conditions when on-lattice and off-lattice models become comparable. The goal of our work is to relate a microscopic mechanism involving few particles localized in space to a global behaviour which occurs at macroscopic scales. In this sense, the only important microscopic details are those which "survive" the coarse-graining and hence play a role in the macroscopic dynamics. Indeed, on-lattice models for run-and-tumble particles were shown to yield the same fluctuating hydrodynamics for the evolution of the coarse-grained density as those found starting from the off-lattice case, in the limit in which the run length v/α is much larger than the lattice spacing [141]. This result is validated by our simulations, which exhibit a phenomenology for the two cases which is definitely comparable (cf. Fig. 2.6 and Fig. 2.7). We can try and make a more quantitative analysis by, e.g., comparing the coexisting densities for the two types of microscopic simulations: as we show in Fig. 2.8, the two methods are in very good agreement.

[7] In our case, the differences in simulation time are roughly two orders of magnitude.

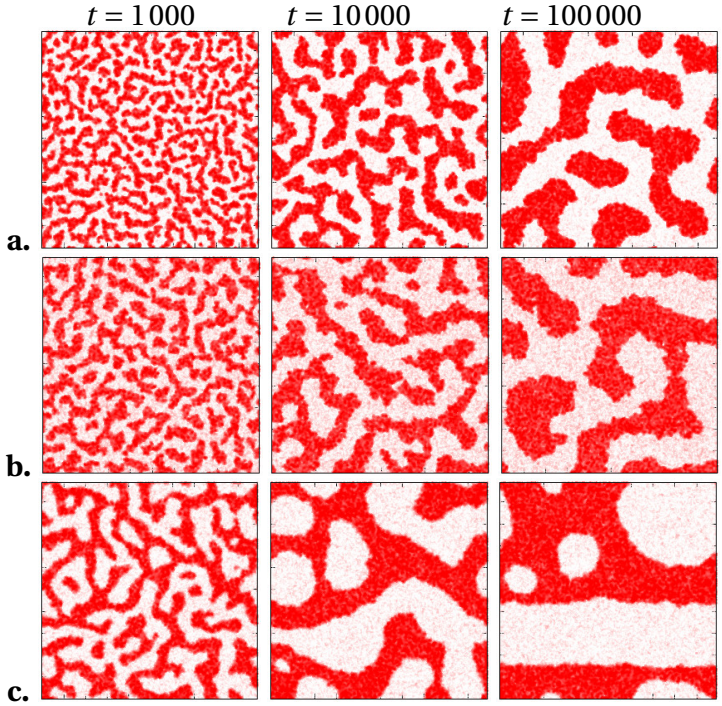

Figure 2.6 – Snapshots of off-lattice simulations with periodic boundary conditions and homogeneous initial density, comparison between different microscopic models. Box size $L = 100$, number of particles $N = 150\,000$.
a. Density dependent speed, constant tumbling rate, constant running rate: $v(\rho) = v_0 + \frac{v_1 - v_0}{2}\left(1 - \tanh\left(\frac{\rho - \rho_m}{L_f}\right)\right)$, $v_0 = 0.1$, $v_1 = 1$, $\rho_m = 12$, $L_f = 3$, $\alpha = 1$, $\beta = 1$.
b. Density dependent running rate, constant speed, constant tumbling rate: $\beta(\rho) = \beta_0 + \frac{\beta_1 - \beta_0}{2}\left(1 - \tanh\left(\frac{\rho - \rho_m}{L_f}\right)\right)$, $\beta_0 = 0.1$, $\beta_1 = 1$, $\rho_m = 12$, $L_f = 3$, $\alpha = 1$, $v = 1$.
c. Density dependent tumbling rate, constant speed, constant running rate: $\alpha(\rho) = \alpha_0 + \frac{\alpha_1 - \alpha_0}{2}\left(1 + \tanh\left(\frac{\rho - \rho_m}{L_f}\right)\right)$, $\alpha_0 = 0.1$, $\alpha_1 = 1$, $\rho_m = 15$, $L_f = 3$, $v = 1$, $\beta = 0.1$. The coarse-grained density ρ is computed with an interaction kernel $K(r) = \frac{1}{Z}\exp\left(-\frac{1}{1-(r/r_0)^2}\right)$, with Z a normalization constant and $r_0 = 1$ (see Appendix A.2.1 for more details).

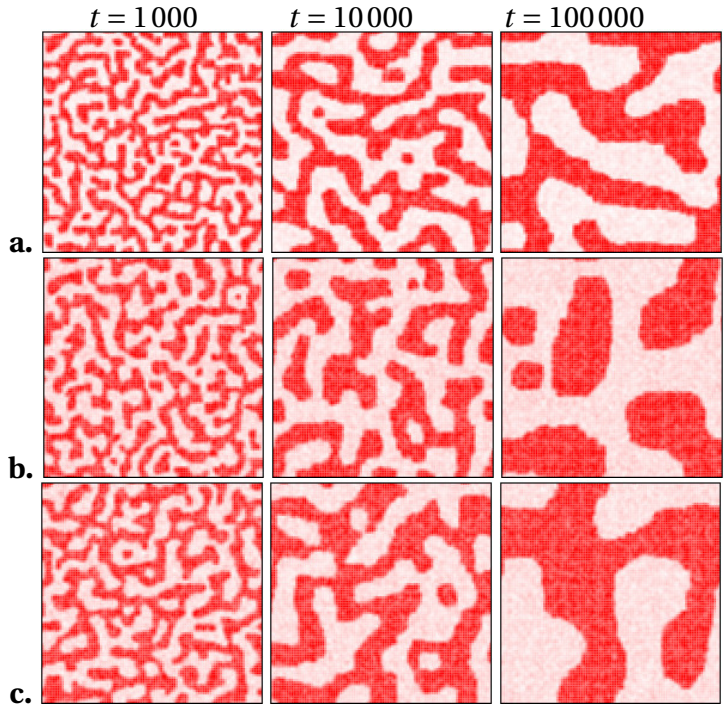

Figure 2.7 – Snapshots of on-lattice simulations with periodic boundary conditions and homogeneous initial density, comparison between different microscopic models. Box size $L = 100$, number of particles $N = 150\,000$.
a. Density dependent speed, constant tumbling rate, constant running rate: $v(\rho) = v_0 + \frac{v_1 - v_0}{2}\left(1 - \tanh\left(\frac{\rho - \rho_m}{L_f}\right)\right)$, $v_0 = 0.1$, $v_1 = 1$, $\rho_m = 12$, $L_f = 3$, $\alpha = 1$, $\beta = 1$.
b. Density dependent running rate, constant speed, constant tumbling rate: $\beta(\rho) = \beta_0 + \frac{\beta_1 - \beta_0}{2}\left(1 - \tanh\left(\frac{\rho - \rho_m}{L_f}\right)\right)$, $\beta_0 = 0.1$, $\beta_1 = 1$, $\rho_m = 12$, $L_f = 3$, $\alpha = 1$, $v = 1$.
c. Density dependent tumbling rate, constant speed, constant running rate: $\alpha(\rho) = \alpha_0 + \frac{\alpha_1 - \alpha_0}{2}\left(1 + \tanh\left(\frac{\rho - \rho_m}{L_f}\right)\right)$, $\alpha_0 = 0.1$, $\alpha_1 = 1$, $\rho_m = 15$, $L_f = 3$, $v = 1$, $\beta = 0.1$. The coarse-grained density ρ is computed with a quasi-circular interaction kernel of radius $r_0 = 1$ (see Appendix A.2.2 for more details).

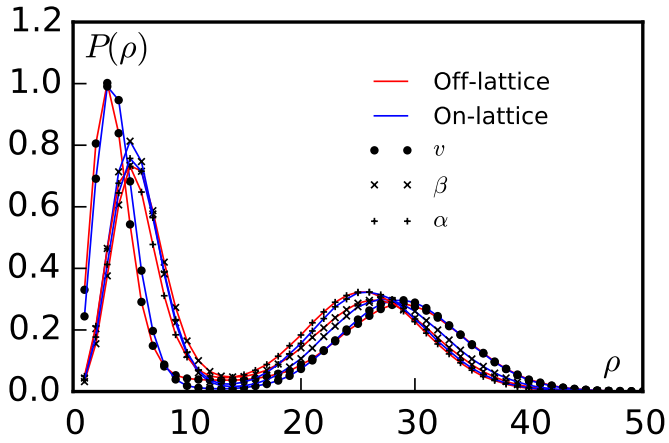

Figure 2.8 – Coexisting densities for microscopic on-lattice and off-lattice simulations. The legend indicates which of the three motility parameters is density-dependent. In the cases of density-dependent speed v and running rate β, simulation parameters are the same as in Figs. 2.6-a, 2.6-b, 2.7-a and 2.7-b. In the case of density-dependent tumbling rate α, the simulation parameters are the same as in Figs. 2.6-c and 2.7-c with the following modifications: $\alpha_0 = 0.01$, $\alpha_1 = 0.1$, $\beta = 0.01$. With this set of parameters, on-lattice and off-lattice simulations result comparable, while for the set of parameters as those in Figs. 2.6-c and 2.7-c the coexisting density show a bigger discrepancy. This could be due to the fact that in that case the lattice spacing is not small with respect to the run length, hence invalidating the continuous limit.

2.3 Pattern formation

To derive Eq. (2.30) we have considered the dynamics of the density field at timescales larger than $1/\alpha$ and $1/\beta$ (through a fast variable approximation). In experiments, this means $t \gg 1$s. At even larger timescales, the dynamics of the division and death of the bacteria become important. In experiments, this means $t \sim 2000$s (30 min). We model this birth-and-death dynamics with a logistic term of the form (2.9), following [23]. The mean-field equation reads

$$\dot{\rho}(\mathbf{r},t) = \nabla\left[D[\rho]\nabla\rho - \mathbf{F}[\rho]\rho\right] + \mu\rho\left(1-\frac{\rho}{\rho_0}\right) - \kappa\Delta^2\rho, \tag{2.47}$$

where μ and ρ_0 were defined in section 2.1.1.3 and we have considered a local approximation of the coarse-grained density.

We can perform a linear stability analysis for Eq. (2.47) by investigating the effect of a small fluctuation around a flat profile. Following [23], we consider a perturbation such as (2.34) around the fixed point of the logistic term ρ_0. This choice is not arbitrary: without MIPS, the dynamics would lead the density throughout the whole system to the fixed point ρ_0. If the homogeneous solution $\rho = \rho_0$ is unstable, then the two dynamics (the stabilizing logistic term and the unstabilizing MIPS) are in competition. The instability condition then reads

$$\sigma(q) = -\mu - q^2 D_{\text{eff}} - q^4\kappa < 0, \tag{2.48}$$

where $\sigma(q)$ is the growth rate of the perturbation: $\delta\dot{\rho}_q = \sigma(q)\delta\rho_q$. Note that because of the logistic term, small q modes are always stable. Unstable modes therefore start at a finite value q_0 (cf. Fig. 2.9).

In the following paragraph we present the results of simulations for a pattern-forming system, i.e. where birth-and-death dynamics are included. We only consider the case in which β is a function of the density, while v and α are constants, since this is the relevant case for the experiments.

2.3.1 Numerical results for pattern forming systems

We start by performing numerical simulations of the microscopic dynamics, where we now include the birth-and-death dynamics. We model the rates with linear functions: the division rate b_0 is a constant, while the death rate $d(\rho) = d_0 + d_1\rho$ is an increasing function of the density. With these definitions it is easy to relate these parameters with those of the

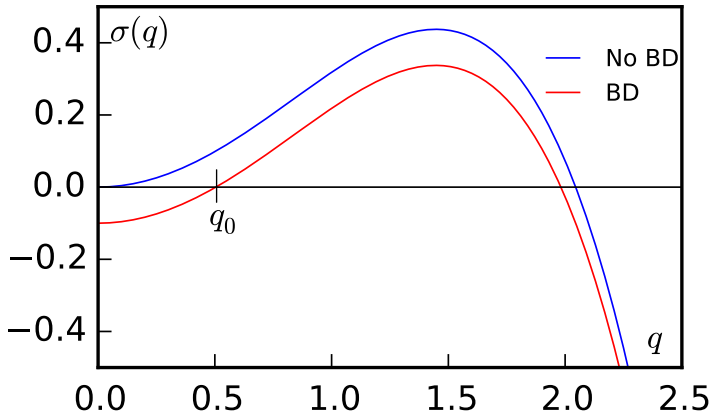

Figure 2.9 – Example of growth rates for systems with and without birth-and-death (BD) term, shown in red and blue, respectively. The large q modes are stabilized by the term $-\kappa\Delta^2\rho$.

logistic term in Eq. (2.47):

$$\mu = b_0 - d_0 \quad \text{and} \quad \rho_0 = \frac{b_0 - d_0}{d_1}. \tag{2.49}$$

Examples of off-lattice and on-lattice simulations are shown in Fig. 2.10 (left and center images, respectively). They show that, instead of the coarsening and complete phase separation of the dynamics (2.33) (cf. last column of Figs. 2.6 and 2.7), the system undergoes a micro-phase separation, and a typical lengthscale is selected. We observe a small difference in this typical lengthscale between off- and on-lattice numerical realizations: this is due to the difference in the way the coarse-grained density is computed in the two algorithms (see Appendix A.2).

Another possibility to test the results of our analysis is to simulate the evolution of the density field following the dynamics (2.47). This can be done by using, e.g., pseudospectral methods. As frequently stated earlier in this thesis, simulations of phenomenological partial differential equations can lead to solutions that qualitatively resemble experimental realizations, and we emphasized the importance of connecting the macroscopic results to microscopic models. In our case, Eq. (2.47) is constructed starting from a microscopic model and is validated by microscopic simulations, and by the fact that phase separation occurs where the linear analysis predicts it. Hence, we can safely consider numerical solutions of the macroscopic equations as a valid instrument to study the collective behaviour of our systems of interacting bacteria[8]. An example of such simulations is shown in the right image of Fig. 2.10 where, for simplicity, the parameter κ has been

[8]The most evident advantage of these simulations is the further reduction of computational cost: this speeds up simulations time by another order of magnitude.

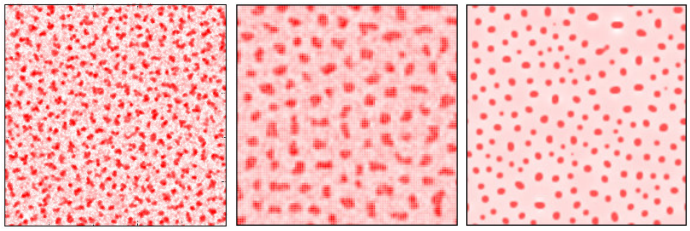

Figure 2.10 – Simulations of run-and-tumble particles with birth-and-death dynamics, periodic boundary conditions and homogeneous initial density. Box size $L = 100$.
Left: Off-lattice microscopic simulations. Initial number of particles $N = 150\,000$, $\beta(\rho) = \beta_0 + \frac{\beta_1-\beta_0}{2}\left(1-\tanh\left(\frac{\rho-\rho_m}{L_f}\right)\right)$, $\beta_0 = 0.1$, $\beta_1 = 1$, $\rho_m = 12$, $L_f = 3$, $\alpha = 1$, $\nu = 1$, $b_0 = 0.015$, $d_0 = 0$, $d_1 = 0.001$. Computation of the coarse-grained density as in Fig. 2.6.
Center: On-lattice microscopic simulation. Initial number of particles $N = 150\,000$, $\beta(\rho) = \beta_0 + \frac{\beta_1-\beta_0}{2}\left(1-\tanh\left(\frac{\rho-\rho_m}{L_f}\right)\right)$, $\beta_0 = 0.1$, $\beta_1 = 1$, $\rho_m = 12$, $L_f = 3$, $\alpha = 1$, $\nu = 1$, $b_0 = 0.015$, $d_0 = 0$, $d_1 = 0.001$. Computation of the coarse-grained density as in Fig. 2.7.
Right: Numerical solution of Eq. (2.47). Initial condition $\rho = 15 + \delta\rho$, where $\delta\rho$ is a random perturbation of the order 10^{-3}, $\beta(\rho) = \beta_0 + \frac{\beta_1-\beta_0}{2}\left(1-\tanh\left(\frac{\rho-\rho_m}{L_f}\right)\right)$, $\beta_0 = 0.1$, $\beta_1 = 1$, $\rho_m = 12$, $L_f = 3$, $\alpha = 1$, $\nu = 1$, $\mu = 0.015$, $\rho_0 = 15$, $\kappa = 0.01$.

taken as a constant (cf. discussion in section 2.2.2.1).

So far, following the linear analysis of the stable profile, we have only considered systems whose initial conditions are homogeneous. To reproduce the results of the experiments, we perform macroscopic simulations where we choose a central inoculum as initial condition for the density profile. Three snapshots of the simulation are shown in Fig. 2.11: the rings appear sequentially at regular distance from one another. Note that the condition for instability (2.39) is obtained by considering a perturbation of a homogeneous profile, while in the case of initial central inoculum the profile is highly non-homogeneous. However, the logistic term is responsible for the initial spreading of the colony through a propagating front described by Eq. (2.11). When the density profile enters the unstable range, the system undergoes pattern formation.

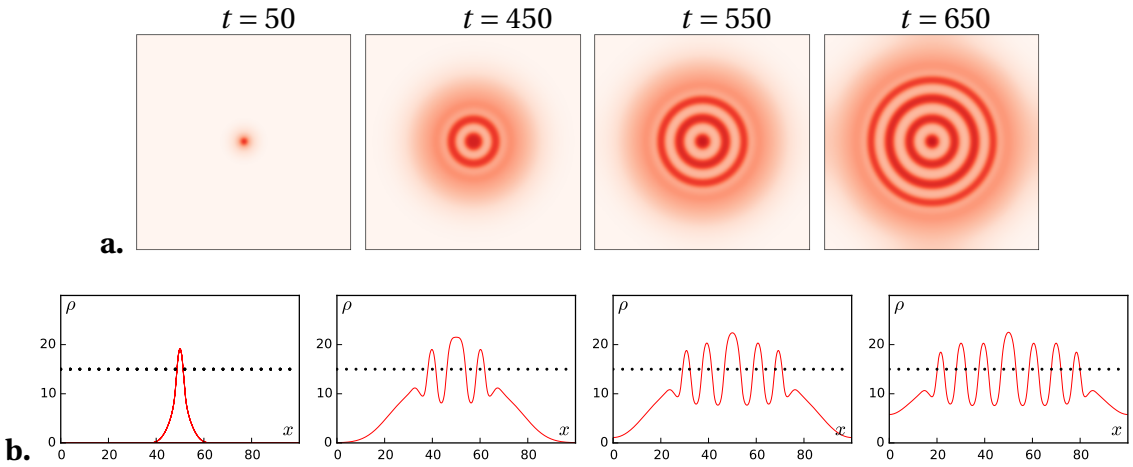

Figure 2.11 – Snapshots of a numerical solution of Eq. (2.47) starting from a central inoculum. Box size $L = 100$, $\beta(\rho) = \beta_0 + \frac{\beta_1-\beta_0}{2}\left(1-\tanh\left(\frac{\rho-\rho_m}{L_f}\right)\right)$, $\beta_0 = 0.1$, $\beta_1 = 1$, $\rho_m = 12$, $L_f = 3$, $\alpha = 1$, $\nu = 1$, $\mu = 0.015$, $\rho_0 = 15$, $\kappa = 0.1$. **a.** 2D view of the evolving density. **b.** Density profile along a cut at y = 50. The dotted line represents the target density $\rho_0 = 15$.

Chapter 3

Pattern formation in multispecies bacterial colonies

3.1 Introduction

In chapter 2 we have considered bacterial colonies in which cells interact by decreasing their motility when the local density is high enough. We have shown that this mechanism, coupled with population growth, can lead to the formation of spatial patterns. In the present chapter our study on the role of motility in pattern formation is extended to the case of bacterial colonies composed of several different species. To tackle the problem, we combined theoretical tools with *in vitro* experiments, in which synthetic biology allowed us to control the interactions. This part of my thesis was conducted in close collaboration with the group of Prof. Jiandong Huang from the university of Hong Kong.

3.1.1 Motivations

The motivations for investigating multispecies systems are numerous. Firstly, we recall that the question at the root of our study of pattern formation is how living organisms can attain spatial self-organization. Real systems are rarely composed of only one type of cells: highly varied bacterial communities are found, e.g., in soil [143] or in the human intestine [44] and the diversity of species in such communities is at the basis of many important functions [101, 91]. Considering multispecies systems is therefore important in the perspective of understanding spatial self-organization in *in vivo* bacterial colonies, or in multicellular organisms in general.

Another motivation, more theoretical, to study multispecies bacterial colonies, is to explore the fate of MIPS when several different types of particles interact. In particular, we wish to investigate what kind of new microscopic interactions can be implemented and how they affect collective behaviours at macroscopic scales.

Finally, from a more engineering point of view, finding new mechanisms – in this case based on the modulation of transport efficiency – capable of controlling or generating spatial structures could potentially be used to design functional communities.

3.1.2 The case of two species

In most of this chapter we focus on pattern formation in bacterial colonies composed of two species. This is a first necessary step before turning to more general multispecies systems, for at least two reasons: firstly, we want to gain a full understanding of collective behaviours in a two-species colony in order to get a clearer picture of what are the novelties introduced with respect to a system of identical particles, and thus to address more complicated cases advisedly. Secondly, we want to remain as close as possible to experimentally realizable setups, and the case of two species already presents a technical challenge, as explained in section 3.2.

Consider a colony composed of two different species of motile run-and-tumble *E. coli*, which from now on we call species A and species B. If considered isolated, the two species are identical: a single bacterium of species A is indistinguishable from a single bacterium of species B, and they behave in the same way. They become distinguishable – though maybe still interchangeable – when they can interact, which occurs via quorum sensing. As in the single-species case, the effect of quorum sensing interactions is a modification of bacterial motility, occurring through gene regulation, but in this case we consider a *reciprocal* quorum sensing interaction[1]. With this, we mean that bacteria of species A only respond to the presence of bacteria of species B, and viceversa. We call this interaction *mutual* regulation.

Given the standard mechanism of MIPS for a single-species system, one can imagine that, for both species, the effect of the mutual interaction is a reduction of the motility. We call this effect *mutual inhibition* of the motility. Note that even if the resulting effect is the same as the one in single-species systems, namely a decrease of transport efficiency in dense regions, the triggering mechanisms are quite different: in the single-species case it is motility self-regulation while in the two-species case it is motility mutual regulation.

The presence of two different species provides the possibility to investigate other types of interactions. For instance, instead of reducing each other's motility, the two species can interact by increasing it. In this case, we speak of *mutual activation* of the motility. This interaction has no counterpart in single-species systems, at least if one is interested in

[1] Systems of two self-interacting species would behave qualitatively as two isolated single-species systems, the only difference being that, because they have to cohabit in the same environment, they are in competition for nutrient resources.

systems that can undergo phase separation, as our linear stability analysis of section 2.2.2 shows. In the next sections we show that systems of two species that interact by mutually increasing their transport efficiency can indeed undergo phase separation.

Finally, one can consider the case of mixed mutual interactions for the two species: species A "activates" species B while species B "inhibits" species A, or viceversa. As we show in section 3.4, however, this particular mutual regulation mode cannot give rise to a phase separation.

This chapter is organized as follows: we start our analysis of a two-species system by presenting the experiments performed by our collaborators, in particular by Nan Zhou, a Ph.D. student in the group directed by Prof. Jiandong Huang at the University of Hong Kong. We did not directly perform the experiments, but we helped in their conception and design. We would like to point out that, unlike the experiments and theoretical models presented in the last chapter (sections 2.1.2 and 2.2.1, respectively) – where our theory was developed at a later stage, in order to better understand the experimental results – here the whole experimental procedure has been developed with our collaboration from the start. For the sake of clarity we present the experimental implementation and results first and the theoretical model and numerical simulations afterwards. We then discuss in detail the origin of patterns in two-species colonies. Finally, we present some preliminary results obtained with a three-species colony, and corresponding numerical simulations.

3.2 Experimental realizations

We now illustrate how it is possible to experimentally implement the two types of mutual interactions we just described, namely mutual inhibition and mutual activation, in a colony of motile *E. coli*. In order to implement mutual interactions, we need to construct two quorum sensing genetic circuits (one for each species) in such a way that the motility-control module of bacteria A responds only to signals produced by bacteria B, and vicecersa.

The two quorum sensing genetic circuits are constructed by adopting the quorum sensing systems *luxI-luxR* from *Vibrio fischeri* and *lasI-lasR* from *Pseudomonas aeruginosa*, which have been widely used as building blocks for engineering synthetic systems with intercellular signaling and density-dependent phenotypes [156, 5, 135]. Specifically, *lasI* in bacteria A and *luxI* in bacteria B separately synthesize and secrete two different AHL molecules (3oc12HSL and 3oc6HSL). The two types of AHL molecules then bind to and activate the transcriptional regulators *lasR* in bacteria B and *luxR* in bacteria A, respectively. The activation of these regulators induces gene expression [50, 53, 108], which,

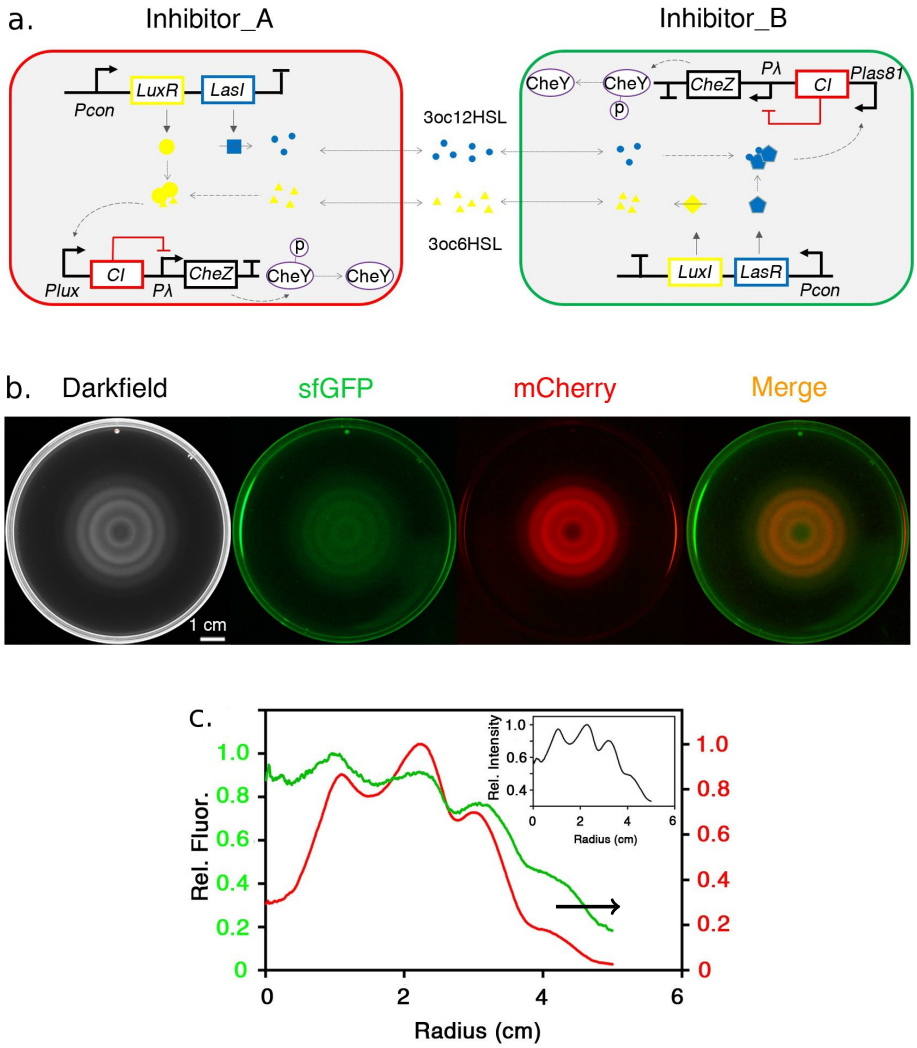

Figure 3.1 – a. Genetic circuit for the implementation of mutual inhibition. See main text for detailed description. **b.** Colocalized fluorescent stripe patterns formed by mutual inhibition strains. A darkfield snapshot shows the pattern resulting from the expansion of interacting *E. coli* strains. The separated strains are shown in mCherry (species A), sfGFP (species B), and merged fluorescent channels (see online version if contrast in printed version does not allow a clear view of the ring patterns). **c.** Propagating front. Relative fluorescent intensity of mutually inhibition strains at varying radius from the seeding center, quantified from the images in b. The inset shows a relative density profile of the bacteria populations at varying radius for the dark field snapshot in b. The intensity values were calculated as the average pixel intensity values across a 2π angle at fixed radius from the seeding center. The relative values are the pixel average relative to the maximum after background subtraction.

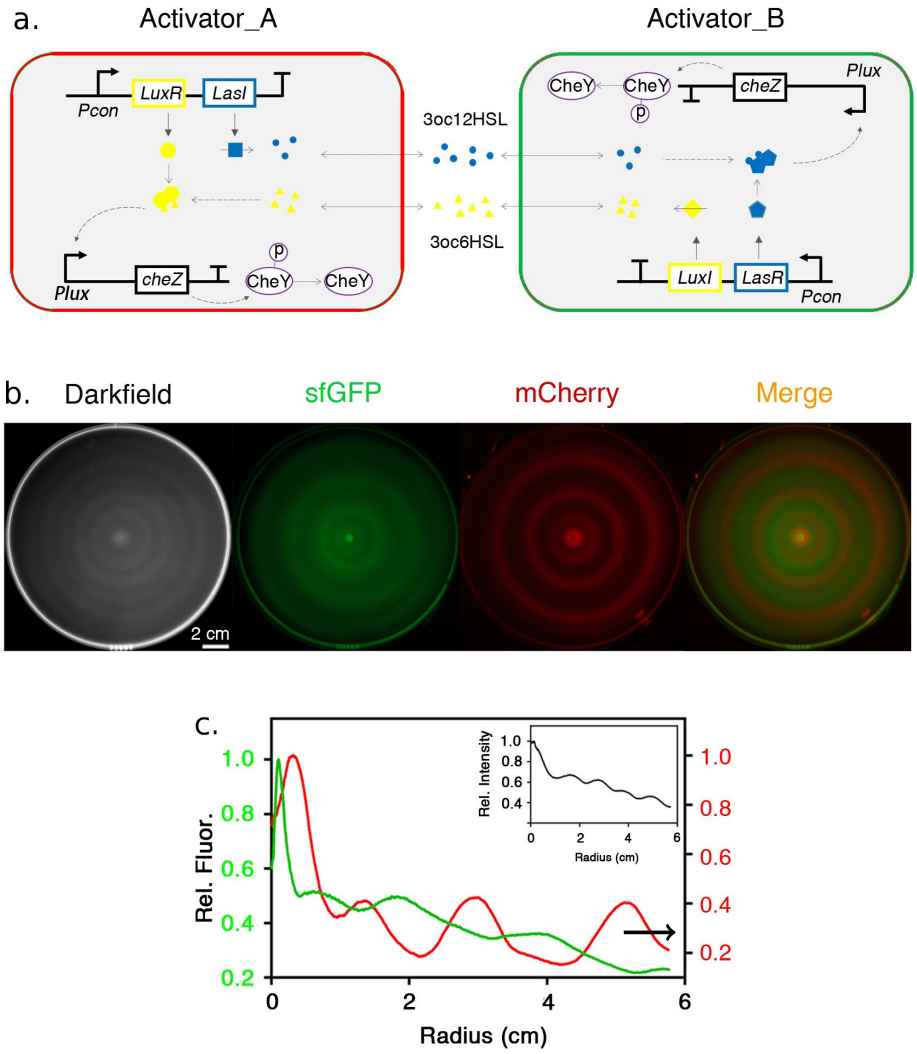

Figure 3.2 – a. Genetic circuit for the implementation of mutual activation. See main text for detailed description. **b.** Segregated fluorescent stripe patterns formed by mutual activation strains. A darkfield snapshot shows the pattern resulting from the expansion of interacting *E. coli* strains. The separated strains are shown in mCherry (species A), sfGFP (species B), and merged fluorescent channels (see online version if contrast in printed version does not allow a clear view of the ring patterns). **c.** Propagating front. Relative fluorescent intensity of mutually activating strains at varying radius from the seeding center, quantified from the images in b. The inset shows a relative density profile of the bacteria populations at varying radius for the dark field snapshot in b. The intensity values were calculated as the average pixel intensity values across a 2π angle at fixed radius from the seeding center. The relative values are the pixel average relative to the maximum after background subtraction.

in our case, results in motility control.

To reproduce mutual inhibition and mutual activation mechanisms, two types of motility-control modules need to be designed. For mutual inhibition, we follow an approach reminiscent of the single-species case: the transcription of *cheZ* is repressed and, in the presence of a high AHL level, cells tumble incessantly, with a consequent reduction of their transport efficiency. To implement a mutual activation interaction, the natural transcription of *cheZ* is deleted: in this case, then, the motility-control module is designed to restore *cheZ* transcription, hence increasing the cell transport efficiency in the presence of high AHL level. The genetic circuits just described are illustrated in Figs. 3.1-a and 3.2-a.

To distinguish between species A and B, each species is tagged with a different fluorescent molecule (mCherry for species A and sfGFP for species B). Pictures of the fluorescent bacteria are then taken after letting the light pass through two filters, sensitive to the typical frequencies of the emission spectrum of the two fluorescent molecules. We note two technical difficulties due to this setup: firstly, if the two species are in the same environment, which is the case when they interact, a fluorescent picture of the entire population cannot be taken: one needs to take images of the sample with one filter per species. Secondly, fluorescent molecules must emit at wavelength distant enough so that the signals can be resolved; these are some of the reasons why it is not trivial to increase the number of species in experiments.

The two species can then be engineered with the two mutual interaction mechanisms. Let us call the mutually inhibiting particles "inhibitors" and the mutually activating particles "activators". We first consider the case of a drop of a mixture of inhibitors inoculated at the center of a petri dish containing semisolid agar gel. The motile bacteria swim and reproduce, and 24 hours later the drop has spread in the radial direction and developed circular patterns (see Fig. 3.1-b). The circular patterns, or rings, are colocalized in space, i.e. the two species develop *in-phase* spatial oscillations (see Fig. 3.1-c). We note the similarity of these rings with the ones formed by single-species colonies (cf. bottom panel of Fig. 2.3), but stress that here the mechanism involves mutual regulation of motility.

We now consider the case in which a drop of a mixture of activators is inoculated at the center of a petri dish containing semisolid agar gel. After 24 hours, this colony has also spread and developed circular patterns (see Fig. 3.2-b). In this case, however, the rings are segregated, i.e. the two species develop *out-of-phase* spatial oscillations (see Fig. 3.2-c). This behaviour has no counterpart for single-species systems and it therefore represents a real novelty.

No experiment with mixed colonies, i.e. containing inhibitors and activators, was performed, since we do not expect to observe any spatial structures in such systems. We argue this point in section 3.4.

To conclude, note that the spreading diameter reached by the colony of inhibitors and activators are quite different. The activators spread much more than the inhibitors. Indeed, if we consider the case of mutual inhibition, the colony is divided into two types of regions: in one region both species are scarce and their transport efficiency high, while in the other one they are dense and their transport efficiency low. If we now consider the case of mutual activation, the colony is again separated into two types of regions: in this case, in each region one of the two species is dense and its transport efficiency is high. Therefore, on average, the motility in the colony of mutually inhibiting particles is lower than the motility in the colony of mutually activating particles. This explains the difference in the colony spreading in the two cases.

3.3 Theoretical model and results

In this section we construct a model for inhibitors and activators and develop a fluctuating hydrodynamics for the density fields ρ_A and ρ_B for the two species of bacteria. We then perform numerical simulations in order to validate the model and compare it with the experiments.

3.3.1 Coarse-graining procedure for a two-species system

In order to obtain a fluctuating hydrodynamics for the density fields ρ_A and ρ_B, we follow the steps of the coarse-graining procedure presented in section 2.2.1 and generalize it to the case of a system of two species of run-and-tumble bacteria with finite tumble duration and density-dependent motility.

As in the single-species case, we assume that each bacterium ℓ has a speed v_ℓ, a tumbling rate α_ℓ, and a running rate β_ℓ, and that it can be in two possible dynamical states, defined by the discrete variable σ_ℓ: a running state ($\sigma_\ell = 1$) and a tumbling state ($\sigma_\ell = 0$). The system is now composed of N_A bacteria of species A and N_B bacteria of species B, with total number of bacteria $N = N_A + N_B$. Since the choice of indices is arbitrary, we suppose that particles whose index is smaller than or equal to N_A are of species A, while particles whose index is between $N_A + 1$ and N are of species B. For each particle ℓ, the motility parameters v_ℓ, α_ℓ and β_ℓ are functions of the positions of the particle ℓ and of the positions of the particles of the species opposite to ℓ: for instance, $v_\ell = v_\ell(\mathbf{r}_\ell^A, \{\mathbf{r}_n^B\})$ if $\ell \leq N_A$, while $v_\ell = v_\ell(\mathbf{r}_\ell^B, \{\mathbf{r}_n^A\})$ if $\ell > N_A$, with $\{\mathbf{r}_n^A\} \equiv \mathbf{r}_1^A, \ldots, \mathbf{r}_{N_A}^A$ and $\{\mathbf{r}_n^B\} \equiv \mathbf{r}_{N_A+1}^B, \ldots, \mathbf{r}_N^B$. This dependence follows from the fact, implemented in the experiments, that the motility parameters of one species are affected only by the presence of bacteria of the opposite species, and of course of the bacterium they correspond to, through $\mathbf{r}_\ell^{A,B}$.

The dynamics of this system is described by a master equation formally identical to (2.12), with the difference that the sum now runs over the $N = N_A + N_B$ particles, describing the two types of bacteria. We recall it here for the sake of clarity:

$$\begin{aligned}\dot{P}(\{\mathbf{r}_n,\theta_n,\sigma_n\},t) = &\sum_{\ell=1}^{N}\sigma_\ell\left[-\nabla_\ell\cdot(v_\ell\mathbf{u}_{\theta_\ell}P)-\alpha_\ell P+\frac{\beta_\ell}{2\pi}\int \mathrm{d}\theta'_\ell P_{\sigma_\ell=0}\right]\\ &+\sum_{\ell=1}^{N}(1-\sigma_\ell)\left[-\beta_\ell P+\alpha_\ell P_{\sigma_\ell=1}\right].\end{aligned} \tag{3.1}$$

$\{\mathbf{r}_n\}$, $\{\theta_n\}$, and $\{\sigma_n\}$ now represent the position, orientation, and dynamical state of particles of both species A and B.

3.3.1.1 Diffusion-drift approximation

The goal of this coarse-graining procedure is to obtain the equations governing the time evolution of the two density fields $\rho_A(\mathbf{r},t)$ and $\rho_B(\mathbf{r},t)$. The first part of the procedure, i.e. the diffusion-drift approximation, can be carried out following the same steps as in the procedure for the single-species system, detailed in section 2.2.1.1. We recall here the main steps to obtain a Fokker-Planck equation for the probability density C_0:

1. expand the probability density P on a joint Fourier basis $\{\exp\left(i\sum_{j=1}^{N}k_j\theta_j\right)\}$;
2. project the master equation on the different harmonics to obtain the dynamics of the coefficients C_0, $C_{\pm\ell}$, etc...;
3. perform a fast-variable approximation and neglect the dynamics of the non-conserved variables, i.e. all coefficients except C_0
4. truncate the gradient expansion at the order $\mathcal{O}(\nabla^2 C_0)$[2].

The evolution of the probability density C_0 thus reads

$$\dot{C}_0 = \sum_\ell \nabla_\ell\cdot\left[\frac{v_\ell}{2\alpha_\ell}\nabla_\ell\left(\frac{v_\ell}{1+\frac{\alpha_\ell}{\beta_\ell}}C_0\right)\right] = \sum_\ell \nabla_\ell\cdot(D_\ell\nabla_\ell C_0 - \mathbf{F}_\ell C_0), \tag{3.2}$$

where

$$D_\ell = \frac{v_\ell^2}{2\alpha_\ell\left(1+\frac{\alpha_\ell}{\beta_\ell}\right)} \qquad \text{and} \qquad \mathbf{F}_\ell = -\frac{v_\ell}{2\alpha_\ell}\nabla_\ell\frac{v_\ell}{1+\frac{\alpha_\ell}{\beta_\ell}}. \tag{3.3}$$

The sum runs over all $N = N_A + N_B$ particles and the dependences of the diffusion and drift coefficients are $D_\ell = D_\ell(\mathbf{r}_\ell^A,\{\mathbf{r}_n^B\})$ and $\mathbf{F}_\ell = \mathbf{F}_\ell(\mathbf{r}_\ell^A,\{\mathbf{r}_n^B\})$ if $\ell \le N_A$, and $D_\ell = D_\ell(\mathbf{r}_\ell^B,\{\mathbf{r}_n^A\})$ and $\mathbf{F}_\ell = \mathbf{F}_\ell(\mathbf{r}_\ell^B,\{\mathbf{r}_n^A\})$ if $\ell > N_A$.

[2]Note that this truncations neglect gradient terms whose role we discuss later in section 3.4.2

3.3.1.2 The role of mutual interactions

In our system, the motilities of bacteria of species A depend on the AHL molecules secreted by bacteria of species B, and viceversa. Following the argument proposed in section 2.2.1.2, we define two local density fields, one for each species,

$$\begin{aligned}\rho_A(\mathbf{r},t) &= \sum_i \rho_i^A(\mathbf{r},t) = \sum_i \delta(\mathbf{r}-\mathbf{r}_i^A(t)) \\ \rho_B(\mathbf{r},t) &= \sum_i \rho_i^B(\mathbf{r},t) = \sum_i \delta(\mathbf{r}-\mathbf{r}_i^B(t)).\end{aligned} \tag{3.4}$$

We then define two coarse-grained densities $\tilde{\rho}_A$ and $\tilde{\rho}_B$ which take into account the concentration field of the AHL molecules, following the reasoning of section 2.2.1.2, and which take the form

$$\begin{aligned}\tilde{\rho}_A(\mathbf{r}_\ell^B) &= \int \mathrm{d}\mathbf{y} K(\mathbf{r}_\ell^B - \mathbf{y})\rho_A(\mathbf{y}) \\ \tilde{\rho}_B(\mathbf{r}_\ell^A) &= \int \mathrm{d}\mathbf{y} K(\mathbf{r}_\ell^A - \mathbf{y})\rho_B(\mathbf{y}).\end{aligned} \tag{3.5}$$

The motility parameters are then assumed to be simple functions of the coarse-grained densities (3.5):

$$\begin{aligned} v_\ell^A(\mathbf{r}_\ell^A,\{\mathbf{r}_n^B\}) &= v_A[\tilde{\rho}_B(\mathbf{r}_\ell^A)] \quad & v_\ell^B(\mathbf{r}_\ell^B,\{\mathbf{r}_n^A\}) &= v_B[\tilde{\rho}_A(\mathbf{r}_\ell^B)] \\ \alpha_\ell^A(\mathbf{r}_\ell^A,\{\mathbf{r}_n^B\}) &= \alpha_A[\tilde{\rho}_B(\mathbf{r}_\ell^A)] \quad & \alpha_\ell^B(\mathbf{r}_\ell^B,\{\mathbf{r}_n^A\}) &= \alpha_B[\tilde{\rho}_A(\mathbf{r}_\ell^B)] \\ \beta_\ell^A(\mathbf{r}_\ell^A,\{\mathbf{r}_n^B\}) &= \beta_A[\tilde{\rho}_B(\mathbf{r}_\ell^A)] \quad & \beta_\ell^B(\mathbf{r}_\ell^B,\{\mathbf{r}_n^A\}) &= \beta_B[\tilde{\rho}_A(\mathbf{r}_\ell^B)]. \end{aligned} \tag{3.6, 3.7}$$

Since ρ_A and ρ_B are functions of the positions of particles A and B, respectively, the substitutions performed in (3.6) for species A and (3.7) for species B are formally legitimate. We claim that they are relevant approximations of the experiments described in section 3.2.

3.3.1.3 Collective dynamics of the coupled density fields

In the last step of the coarse-graining procedure, we derive the dynamics of the density fields $\rho_A(\mathbf{r},t)$ and $\rho_B(\mathbf{r},t)$. As in the single-species case, we start by writing Eq. (3.2) as a Fokker-Planck equation

$$\dot{C}_0 = \sum_\ell \nabla_\ell \cdot \left[\frac{v_\ell^2}{2\alpha_\ell\left(1+\frac{\alpha_\ell}{\beta_\ell}\right)} \nabla_\ell C_0 + \frac{v_\ell}{2\alpha_\ell} \nabla_\ell \frac{v_\ell}{1+\frac{\alpha_\ell}{\beta_\ell}} C_0 \right] \tag{3.8}$$

that can then be recast in a system of coupled Langevin processes for the time evolution of the particles' trajectories. We separate the equations for the two species:

$$\begin{aligned}
\dot{\mathbf{r}}_\ell^A(t) &= \mathbf{f}_\ell^A[\tilde{\rho}_B(\mathbf{r}_\ell^A)] + \sqrt{2g_\ell^A[\tilde{\rho}_B(\mathbf{r}_\ell^A)]}\,\boldsymbol{\eta}_\ell^A(t) \\
\dot{\mathbf{r}}_\ell^B(t) &= \mathbf{f}_\ell^B[\tilde{\rho}_A(\mathbf{r}_\ell^B)] + \sqrt{2g_\ell^B[\tilde{\rho}_A(\mathbf{r}_\ell^B)]}\,\boldsymbol{\eta}_\ell^B(t) \\
\langle \eta_{i,\mu}^X(t)\eta_{j,\nu}^Y(t')\rangle &= \delta_{XY}\delta_{ij}\delta_{\mu\nu}\delta(t-t')
\end{aligned} \tag{3.9}$$

where the spatial dependence of the motility parameters is explicit and $\mathbf{f}_\ell^{A,B}$ and $g_\ell^{A,B}$ are of the form

$$\mathbf{f}_\ell^{A,B} = \frac{v_\ell^{A,B}}{1+\frac{\alpha_\ell^{A,B}}{\beta_\ell^{A,B}}}\nabla_\ell \frac{v_\ell^{A,B}}{2\alpha_\ell^{A,B}} \quad \text{and} \quad g_\ell^{A,B} = \frac{(v_\ell^{A,B})^2}{2\alpha_\ell^{A,B}\left(1+\frac{\alpha_\ell^{A,B}}{\beta_\ell^{A,B}}\right)}. \tag{3.10}$$

The last part of the procedure to obtain the evolution of ρ_A and ρ_B is now identical to the single-species case and is detailed in Appendix A.1.2. The two equations for the density fields can in fact be derived separately, starting from Eqs. (3.9) and applying Itō calculus and using the properties of the delta functions appearing in (3.4). The dynamics of ρ_A and ρ_B read

$$\begin{aligned}
\dot{\rho}_A(\mathbf{r},t) &= \nabla\left[D_A[\tilde{\rho}_B]\nabla\rho_A - \mathbf{F}_A[\tilde{\rho}_B]\rho_A + \sqrt{2D_A[\tilde{\rho}_B]\rho_A}\,\boldsymbol{\Lambda}_A\right] \\
\dot{\rho}_B(\mathbf{r},t) &= \nabla\left[D_B[\tilde{\rho}_A]\nabla\rho_B - \mathbf{F}_B[\tilde{\rho}_A]\rho_B + \sqrt{2D_B[\tilde{\rho}_A]\rho_B}\,\boldsymbol{\Lambda}_B\right],
\end{aligned} \tag{3.11}$$

where

$$D_X[\tilde{\rho}_Y] = \frac{v_X^2}{2\alpha_X\left(1+\frac{\alpha_X}{\beta_X}\right)}, \quad \mathbf{F}_X[\tilde{\rho}_Y] = -\frac{v_X}{2\alpha_X}\nabla\frac{v_X}{1+\frac{\alpha_X}{\beta_X}} \tag{3.12}$$

and

$$\langle \Lambda_X^\mu(\mathbf{r},t)\Lambda_Y^\nu(\mathbf{r}',t')\rangle = \delta_{X,Y}\delta_{\mu\nu}\delta(\mathbf{r}-\mathbf{r}')\delta(t-t'). \tag{3.13}$$

Finally, if the densities $\tilde{\rho}_A$ and $\tilde{\rho}_B$ are slowly varying fields, a gradient expansion yields the same results presented in Eq. (2.31). By considering a symmetric interaction kernel and a truncation at the second order of the gradient expansion of $\tilde{\rho}_A$ and $\tilde{\rho}_B$, Eqs. (3.11) then become

$$\begin{aligned}
\dot{\rho}_A(\mathbf{r},t) &= \nabla\left[D_A[\rho_B]\nabla\rho_A - \mathbf{F}_A[\rho_B]\rho_A + \sqrt{2D_A[\rho_B]\rho_A}\,\boldsymbol{\Lambda}_A\right] + h.o. \\
\dot{\rho}_B(\mathbf{r},t) &= \nabla\left[D_B[\rho_A]\nabla\rho_B - \mathbf{F}_B[\rho_A]\rho_B + \sqrt{2D_B[\rho_A]\rho_B}\,\boldsymbol{\Lambda}_B\right] + h.o.
\end{aligned} \tag{3.14}$$

We discuss the nature and the role of the emerging higher order terms in section 3.4.2.

3.3.2 Connection with the experiments

To establish a connection with the experiments, we need to consider the growth dynamics of the bacterial population. As we have done in the case of single-species bacterial colonies, we introduce a logistic term to model the spreading of the colony. We choose this term as a generalized form of the one species case (2.9):

$$\begin{aligned}\dot{\rho}_A &= \mu\rho_A\left(1-\frac{\rho_A+\rho_B}{\rho_0}\right)\\ \dot{\rho}_B &= \mu\rho_B\left(1-\frac{\rho_A+\rho_B}{\rho_0}\right),\end{aligned} \tag{3.15}$$

where μ is the growth rate of the two species and ρ_0 is the carrying capacity. Note that different metabolisms, for instance due to different genetic circuits or fluorescent molecules, could alter the form of the logistic term to

$$\begin{aligned}\dot{\rho}_A &= \mu_A\rho_A\left(1-\frac{\rho_A+\epsilon_A\rho_B}{\rho_0^A}\right)\\ \dot{\rho}_B &= \mu_B\rho_B\left(1-\frac{\epsilon_B\rho_A+\rho_B}{\rho_0^B}\right).\end{aligned} \tag{3.16}$$

For the sake of simplicity, and in order not to introduce too many phenomenological fitting parameters, we consider the simple form of (3.15).

When patterns arise, we also need to consider higher order gradient terms in order to stabilize the interfaces. The origin of these terms, which is not the same as in the case of single-species systems, is discussed in section 3.4.2. Here we limit ourselves to adding a term proportional to $\Delta^2\rho_{A,B}$ in the equations governing the dynamics of ρ_A and ρ_B, respectively.

The total system of noiseless coupled equations for the two density fields then reads:

$$\begin{aligned}\dot{\rho}_A(\mathbf{r},t) &= \nabla\left[D_A[\rho_B]\nabla\rho_A-\mathbf{F}_A[\rho_B]\rho_A\right]-\zeta\Delta^2\rho_A+\mu\rho_A\left(1-\frac{\rho_A+\rho_B}{\rho_0}\right)\\ \dot{\rho}_B(\mathbf{r},t) &= \nabla\left[D_B[\rho_A]\nabla\rho_B-\mathbf{F}_B[\rho_A]\rho_B\right]-\zeta\Delta^2\rho_B+\mu\rho_B\left(1-\frac{\rho_A+\rho_B}{\rho_0}\right).\end{aligned} \tag{3.17}$$

Simulations of Eqs. (3.17) with central inoculum initial conditions lead to the results shown in Figs. 3.3 and 3.4. We observe remarkable resemblance with the experimental results of Figs. 3.1 and 3.2, respectively. In the first case (see Fig. 3.3), we have implemented the interaction by making the two species inhibit each other's motility: $\beta_A(\rho_B)$ and $\beta_B(\rho_A)$ are decreasing functions of their arguments. As a result, we observe a colocalization of

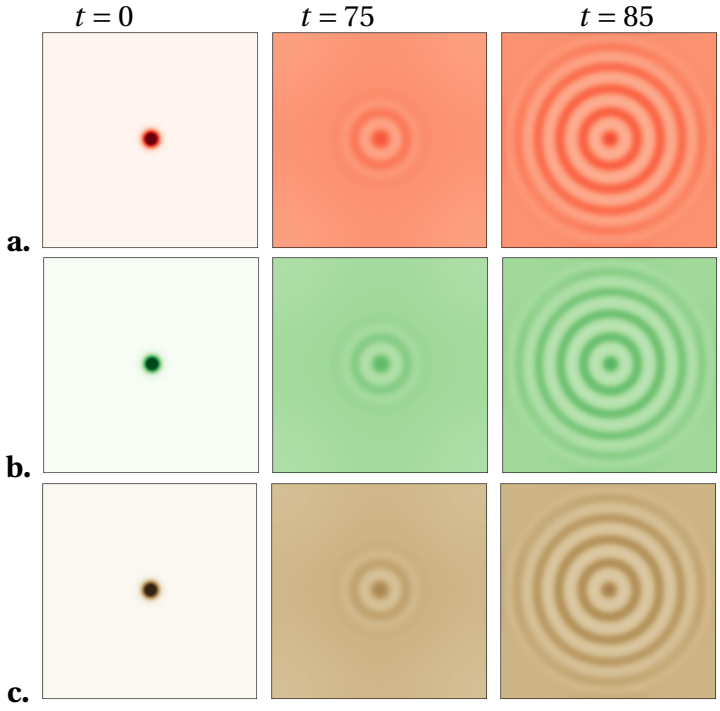

Figure 3.3 – Snapshots of a numerical solution of Eqs. (3.17) starting from a central inoculum for mutual inhibition interactions. The two species develop an in-phase radial oscillation: they are colocalized. Box size $L = 40$, initial conditions $\rho_A^0/\rho_B^0 = 1$, $\beta_i(\rho_j) = \beta_0 + \frac{\beta_1-\beta_0}{2}\left(1 - \tanh\left(\frac{\rho_j-\rho_m}{L_f}\right)\right)$, $\beta_0 = 0.5$, $\beta_1 = 7$, $\rho_m = 9$, $L_f = 3$, $\alpha = 1$, $\nu = 1.5$, $\zeta = 0.1$, $\mu = 0.1$. **a.** Density of species A. **b.** Density of species B. **c.** Total density $\rho = \rho_A + \rho_B$.

the two species, leading to an in-phase spatial oscillation in the radial direction. In the second case, (see Fig. 3.4), we have implemented a motility activation interaction: $\beta_A(\rho_B)$ and $\beta_B(\rho_A)$ are increasing functions of their arguments. As a result, we observe a segregation of the two species, leading to an out-of-phase spatial oscillation in the radial direction. In both cases the rings appear sequentially starting from the central inoculum, after the initial front propagation.

The strong similarity between experimental and numerical results indeed validates our model and our coarse-graining procedure. We stress that this is not a case of simple pattern matching: even though quantitative comparisons are very hard to make (cf. section 2.1.2), our interaction mechanisms of mutual inhibition and mutual activation used in simulations are directly connected with the quorum sensing and motility control implemented in the experiments. Moreover, the approximations and assumptions of our coarse-graining procedure are always physically justified. We can therefore argue that we have found a novel mechanism that can induce self-organization in colonies of multispecies bacteria with density dependent motility. At the end of this chapter we discuss the implication of our work for the possibility of controlling or inducing spatial organization

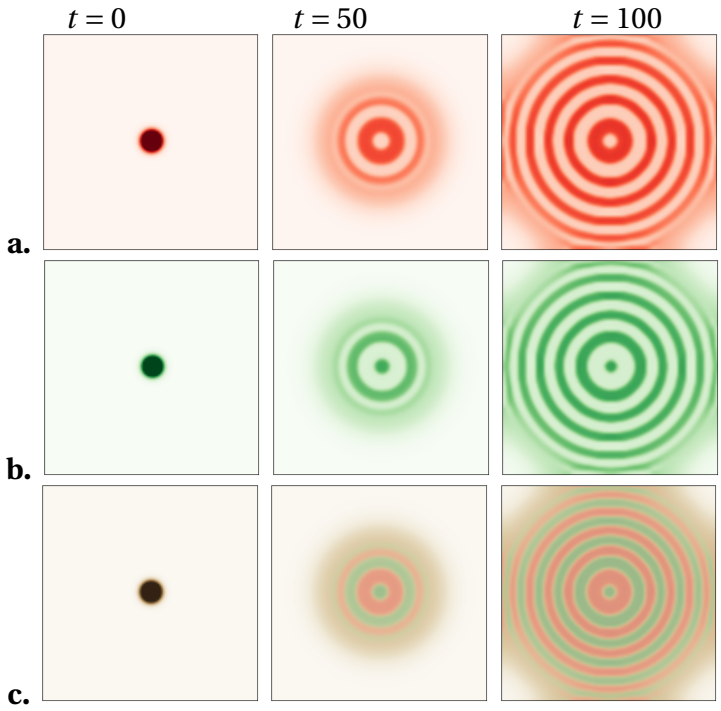

Figure 3.4 – Snapshots of a numerical solution of Eqs. (3.17) starting from a central inoculum for mutual activation interactions. The two species develop an out-of-phase radial oscillation: they are segregated. Box size $L = 40$, initial conditions $\rho_A^0/\rho_B^0 = 1.13$, $\beta_i(\rho_j) = \beta_0 + \frac{\beta_1-\beta_0}{2}\left(1+\tanh\left(\frac{\rho_j-\rho_m}{L_f}\right)\right)$, $\beta_0 = 0.5$, $\beta_1 = 5$, $\rho_m = 9$, $L_f = 3$, $\alpha = 3$, $\nu = 2.5$, $\zeta = 0.01$, $\mu = 0.1$. **a.** Density of species A. **b.** Density of species B. **c.** Total density $\rho = \rho_A + \rho_B$.

in systems of motile particles, showing an example involving a third species.

3.4 Origin of patterns

In the last section, we have introduced a model for a system of two interacting species and, by using two types of interactions, mutual inhibition and mutual activation, we have found two different behaviours: spatial colocalization or segregation. What is the origin of these behaviours? Why cannot we observe spatial structures with mixed inhibition and activation interactions?

In this section, we analyse in detail the interaction mechanisms giving rise to colocalization or segregation of the two species. We start by studying the linear stability of a homogeneous profile and discuss the origin of the higher order gradient terms appearing in Eq. (3.17). We then analyse the role of the logistic term and its interplay with the MIPS mechanism.

3.4.1 Linear analysis

We first consider the intermediate time dynamics such that $1/\alpha, 1/\beta \ll t \ll 1/\mu$, for which the dynamics of the density field is given by Eqs. (3.11). We consider its noiseless, mean-field, version – truncated at the second order in gradients – and perform a linear analysis of homogeneous profiles ρ_A^0 and ρ_B^0. Expanding ρ_A and ρ_B in Fourier modes

$$\begin{aligned} \rho_A &= \rho_A^0 + \sum_q \delta\rho_A^q e^{i\mathbf{q}\cdot\mathbf{r}} \\ \rho_B &= \rho_B^0 + \sum_q \delta\rho_B^q e^{i\mathbf{q}\cdot\mathbf{r}} \end{aligned} \tag{3.18}$$

and injecting this expansion in the dynamics (3.11) yields $\dot{\boldsymbol{\delta\rho}}_q = -q^2 M \boldsymbol{\delta\rho}_q$, where $\boldsymbol{\rho} = (\rho_A, \rho_B)$ and M is the 2×2 dynamical matrix whose entries read

$$\begin{aligned} M_{ii} &= D_i \\ M_{ij} &= D_i \rho_i^0 \left[\log \frac{v_i}{1+\frac{\alpha_i}{\beta_i}} \right]', \end{aligned} \tag{3.19}$$

where D_i is of the form (3.12). Note that the density-dependent parameters v_i, α_i and β_i are evaluated in ρ_j^0, and the prime indicates the derivative with respect to the density ρ_j. The stability of the system is then determined by the sign of the real parts of the eigenvalues of the matrix M. When those are positive, the system is stable, while when there is one

eigenvalue with a negative real part, an instability grows giving rise to phase separation[3]. This happens if the following condition in satisfied:

$$f'_A f'_B > \frac{1}{\rho^0_A \rho^0_B}, \tag{3.20}$$

where we have defined two functions f_A and f_B:

$$\begin{aligned} f_A &\equiv \log \frac{v_A}{1+\frac{\alpha_A}{\beta_A}} \\ f_B &\equiv \log \frac{v_B}{1+\frac{\alpha_B}{\beta_B}}. \end{aligned} \tag{3.21}$$

Condition (3.20) is reminiscent of condition (2.36) for a single-species system, but there are important differences: in (2.36) the derivative of the logarithm must be *negative*, thus the logarithm must be a *decreasing* function of ρ. We recall that this condition corresponds to a decreasing motility. Instead, in (3.20) the *product* $f'_A f'_B$ must be *positive*, which can be satisfied in two ways:

(i) both $f'_A < 0$ and $f'_B < 0$: f_A and f_B are *decreasing* functions of ρ_B and ρ_A, respectively. The motilities of both species are reduced, hence this case corresponds to mutual inhibition;

(ii) both $f'_A > 0$ and $f'_B > 0$: f_A and f_B are *increasing* functions of ρ_B and ρ_A, respectively. The motilities of both species are enhanced, hence this case corresponds to mutual activation;

Note that condition (3.20) does not allow f'_A and f'_B to have opposite signs, thus justifying the claim we made in the introduction section 3.1.2 that systems of mixed inhibition and activation interactions do not undergo phase separation.

We can now consider the eigenvector $(\delta\rho^-_A, \delta\rho^-_B)$, corresponding to the unstable eigenvalue $\sigma^- < 0$, whose properties are informative about how a small perturbation evolves. The expression of the unstable eigenvalue reads

$$\sigma^- = \frac{D_A + D_B - \sqrt{\Delta}}{2} \quad \text{where} \quad \Delta = (D_A + D_B)^2 - 4 D_A D_B \left(1 - \rho_A \rho_B f'_A f'_B\right), \tag{3.22}$$

[3] Recall the linearized dynamics $\dot{\boldsymbol{\delta\rho}}_q = -q^2 M \boldsymbol{\delta\rho}_q$: the system is stable when the real parts of all the eigenvalues of $-q^2 M$ are negative, hence when the real parts of all the eigenvalues of M are positive, and viceversa.

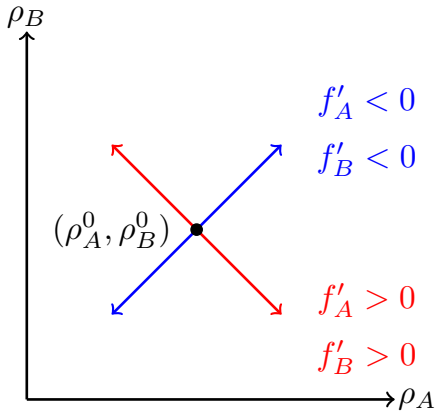

Figure 3.5 – Schematic representation of the the eigenvector associated to the unstable eigenvalue σ^- of the matrix M defined in Eq. (3.19). Starting from a homogeneous unstable condition $(\delta\rho^0_A, \delta\rho^0_B)$, a small perturbation can grow in two directions, here depicted in blue and red. The case represented in blue corresponds to mutual inhibition ($f'_{A,B} < 0$). In this case, in regions where ρ_A grows, ρ_B grows too and in regions where ρ_A decreases, so does ρ_B: the two species become colocalized. The case represented in red corresponds instead to mutual activation ($f'_{A,B} > 0$): In this case, in regions where ρ_A grows, ρ_B decreases and in regions where ρ_A decreases, ρ_B grows: the two species become segregated.

from which a form of its corresponding eigenvector can be easily derived:

$$\begin{pmatrix} \delta\rho^-_A \\ \delta\rho^-_B \end{pmatrix} = \begin{pmatrix} D_A \rho_A f'_A \\ \sigma^- - D_A \end{pmatrix}. \tag{3.23}$$

We observe that while the sign of $\delta\rho^-_B = \sigma^- - D_A < 0$ is fixed, the sign of $\delta\rho^-_A$ depends on the sign of f'_A. We study the two cases, also illustrated in Fig. 3.5:

(i) if $f'_A < 0$, which requires $f'_B < 0$ to observe an instability, then $\delta\rho^-_A$ and $\delta\rho^-_B$ have the same sign and in the regions where one density grows or decreases, so does the other. This hence corresponds to the case of colocalization of the two species;

(ii) if $f'_A > 0$, which requires $f'_B > 0$ to observe an instability, then $\delta\rho^-_A$ and $\delta\rho^-_B$ have opposite signs: in the regions where one density grows, the other decreases, and viceversa. This hence corresponds to the case of segregation of the two species.

The linear analysis therefore agrees with the experimental results: in mutually inhibiting systems the two species are colocalized while they segregate in mutually activating ones.

As we have done for single-species systems, we study the role of the three parameters v, α, and β by allowing only one out of them to vary with the density, while the other two

remain constant. We start by setting $\alpha_{A,B}$ and $\beta_{A,B}$ constant and allowing $v_{A,B}$ to depend on the densities $\rho_{B,A}$. The instability condition then reads

$$f'_A f'_B = [\log v_A]' [\log v_B]' = \frac{v'_A}{v_A}\frac{v'_B}{v_B} > \frac{1}{\rho_A \rho_B}. \tag{3.24}$$

When $v'_{A,B} < 0$, $v_{A,B}$ are decreasing functions of the densities and hence this case corresponds to mutual inhibition. Since $v'_{A,B} < 0$ implies $f'_{A,B} < 0$, (3.23) tells us that in this case A and B are colocalized. The converse reasonment applies to $v'_{A,B} > 0$, which hence corresponds to mutual activation and segregation. We observe that the details related to finite tumble duration, carried by the tumbling and running rates, do not affect condition (3.24).

We then consider the case where the tumbling rate α is density-dependent, while v and β are constant. In this case the instability condition reads

$$f'_A f'_B = \left[\log \frac{1}{\alpha_A + \beta_A}\right]' \left[\log \frac{1}{\alpha_B + \beta_B}\right]' = \left(-\frac{\alpha'_A}{\alpha_A + \beta_A}\right)\left(-\frac{\alpha'_B}{\alpha_B + \beta_B}\right) > \frac{1}{\rho_A \rho_B}, \tag{3.25}$$

where we have explicitated the minus signs in order to emphasize that $f'_{A,B}$ are proportional to $-\alpha'_{A,B}$. This was expected: transport efficiency decreases for high tumbling rates and increases for low tumbling rates. Therefore, when $\alpha'_{A,B} > 0$, and hence $f'_{A,B} < 0$, we are in the case of mutual inhibition and the two species colocalize; on the other hand, when $\alpha'_{A,B} < 0$, and hence $f'_{A,B} > 0$, we are in the case of mutual inhibition and the two species segregate (cf. Eq. (3.23) and its consequences (i) and (ii)).

Finally, we consider the case in which v and α constant and $\beta = \beta(\rho)$. We obtain the following instability condition:

$$f'_A f'_B = \left[\log \frac{\beta_A}{\alpha_A + \beta_A}\right]' \left[\log \frac{\beta_B}{\alpha_B + \beta_B}\right]' = \frac{\alpha_A \beta'_A}{\beta_A(\alpha_A + \beta_A)}\frac{\alpha_B \beta'_B}{\beta_B(\alpha_B + \beta_B)} > \frac{1}{\rho_A \rho_B}. \tag{3.26}$$

Here we have again that $f'_{A,B}$ are proportional to $\beta'_{A,B}$, from which we conclude that when $\beta'_{A,B} > 0$, the two species inhibit each other and hence colocalize, while when $\beta'_{A,B} < 0$, they activate each other and hence segregate.

To test our results, we perform on-lattice numerical simulations of microscopic systems. For simplicity, we choose to implement the dynamics of a system in which tumbles are instantaneous and where the interactions modulating the motility thus occur through the parameters $v_{A,B}(\rho_{B,A})$. This allows for faster calculations while not affecting the density-dependent-motility mechanism, which, as shown in the instability condition (3.24), does not depend on the tumbling and running rates. As expected, the two species

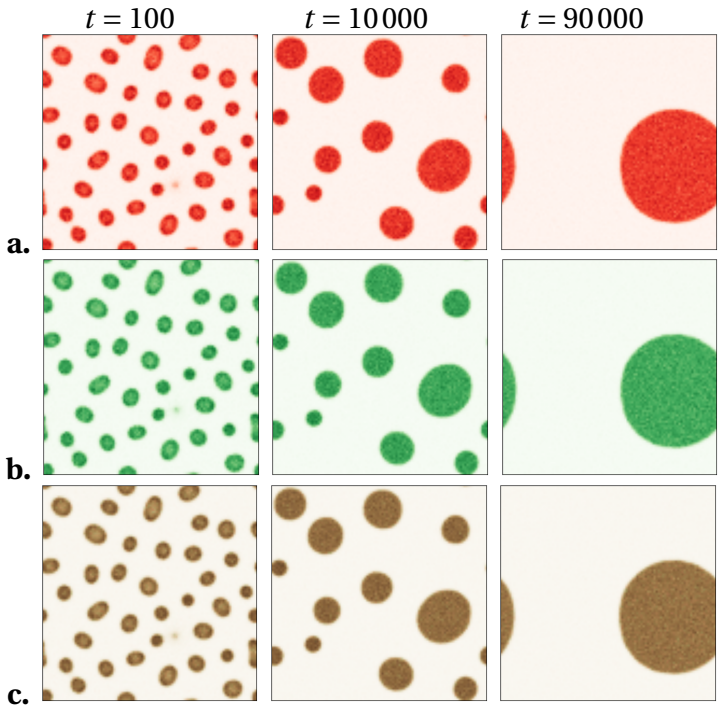

Figure 3.6 – Snapshots of an on-lattice simulation of a system with mutual inhibition interactions, starting from homogeneous densities. We observe colocalization of the two species and a complete coarsening at steady state. Box size $L = 100$, number of particles $N_A = N_B = 500\,000$, $v_i(\rho_j) = v_1 + \frac{v_0 - v_1}{2}\left(1 - \tanh\left(\frac{\rho_j - \rho_m}{L_f}\right)\right)$, $v_1 = 0.1$, $v_0 = 6$, $\rho_m = 50$, $L_f = 30$, $\alpha = 1$. The coarse-grained densities ρ_A and ρ_B are computed with a quasi-circular interaction kernel of radius $r_0 = 3$. **a.** Density of species A. **b.** Density of species B. **c.** Total density $\rho = \rho_A + \rho_B$.

are colocalized in the case of mutual inhibition (Fig. 3.6) and segregated in the case of mutual activation (Fig. 3.7), with a complete coarsening in the steady state.

3.4.2 Higher order gradients

In deriving Eq. (3.11), we have considered an expansion of the coarse-grained density of the type shown in (2.31). In the following we have neglected the higher order gradients that appear when (2.31) is substituted in Eq. (3.11). We now want to understand the role of these terms that we have so far neglected and which determine the stability of high wavenumbers q.

Consider the equation for the evolution of ρ_A. By keeping terms up to fourth order in gradients, its form would be very similar to Eq. (2.40). The important difference is that, since the motility parameters of species A depend on ρ_B, the higher order gradients appearing in the equation for ρ_A are derivatives of the density ρ_B. Calling $m_1^A(\rho_B) = \frac{v_A}{2\alpha_A}$ and

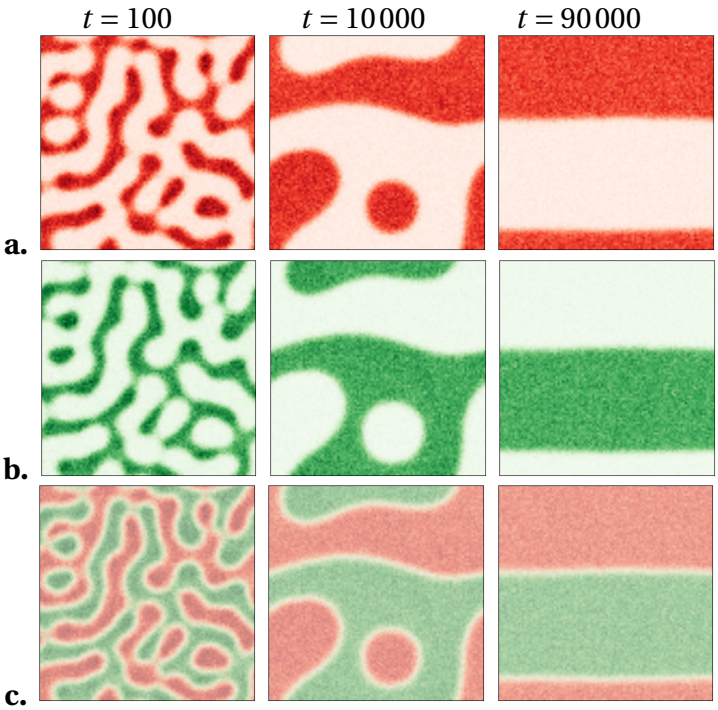

Figure 3.7 – Snapshots of an on-lattice simulation of a system with mutual activation interactions, starting from homogeneous densities. We observe segregation of the two species and a complete coarsening at steady state. Box size $L = 100$, number of particles $N_A = N_B = 500000$, $v_i(\rho_j) = v_0 + \frac{v_1 - v_0}{2}\left(1 + \tanh\left(\frac{\rho_j - \rho_m}{L_f}\right)\right)$, $v_0 = 0.1$, $v_1 = 6$, $\rho_m = 50$, $L_f = 30$, $\alpha = 1$. The coarse-grained densities ρ_A and ρ_B are computed with a quasi-circular interaction kernel of radius $r_0 = 3$. **a.** Density of species A. **b.** Density of species B. **c.** Total density $\rho = \rho_A + \rho_B$.

$m_2^A(\rho_B) = \frac{v_A}{1+\alpha_A/\beta_A}$, we obtain

$$\begin{aligned}\dot{\rho}_A(\mathbf{r},t) = &\nabla\cdot\left[\left(m_1^A m_2^A + \rho_A m_1^A\left(m_2^A\right)'\right)\nabla\rho_A\right]\\ &+\nabla\cdot\left[\frac{1}{2}\sigma^2\Delta\rho_B\left[\left(m_1^A m_2^A\right)' + \rho_A\left(m_1^A\left(m_2^A\right)'\right)'\right]\nabla\rho_B\right]\\ &+\nabla\cdot\left[\frac{1}{2}\sigma^2\rho_A m_1^A\left(m_2^A\right)'\nabla\Delta\rho_B\right].\end{aligned} \tag{3.27}$$

The converse holds for the dynamics of ρ_B. Considering a small perturbation around a homogeneous profile $\rho_{A,B} = \rho^0_{A,B} + \sum_q \delta\rho^q_{A,B} e^{iqx}$ yields the following dynamics for $\delta\rho^q_{A,B}$:

$$\dot{\boldsymbol{\delta\rho}}_q = (-q^2 M + q^4 M_4)\boldsymbol{\delta\rho}_q, \tag{3.28}$$

where M is defined in (3.19) and M_4 is an off-diagonal matrix such that

$$\begin{aligned}M_{4\,ii} &= 0\\ M_{4\,ij} &= \frac{1}{2}\sigma^2\rho_j m_1^j\left(m_2^j\right)' = \frac{1}{2}\sigma^2\rho_j D_j f_j',\end{aligned} \tag{3.29}$$

with f_j' as in (3.20). We also define for simplicity $\kappa_i \equiv M_{4\,ij}$. An instability then occurs when

$$q^4\kappa_A\kappa_B + q^2\left(D_A\rho^0_A f_A' + D_B\rho^0_B f_B'\right) - D_A D_B\left(1-\rho^0_A\rho^0_B f_A' f_B'\right) > 0. \tag{3.30}$$

Note that, when the system is unstable, $f_A' f_B' > 0$ and hence $\kappa_A\kappa_B > 0$ too. If we call the roots of the left hand side of (3.30) q_+^2 and q_-^2, then the inequality is satisfied for $q^2 > q_+^2$, which means that the instability is not saturated: all modes larger than q_+^2 are unstable. This fact is unexpected: in the single-species case, the fourth order gradients obtained from the expansion of the coarse-grained density are stabilizing at linear level (cf. (2.41) and (2.42)). Here, instead, they are not. Moreover, pushing the gradient expansion further (sixth order, eighth order in gradients, etc.) would give rise, at the linear level, to additional terms in Eq. (3.28) of the type $q^6 M_6$, $q^8 M_8$, etc. Just like M_4, all the matrices M_6, M_8, etc. are off-diagonal, and the leading q term in the instability condition will always result from the product of two coefficients of the same sign (in the case of truncation at fourth order, we have $\kappa_A\kappa_B > 0$).

Nevertheless, in microscopic simulations such as those shown in Figs. 3.6 and 3.7, we observe an instability where predicted and a corresponding instability saturation with smooth interfaces. Where do the stabilizing terms then come from? We note that during the coarse-graining procedure we carried out another gradient expansion, namely in the

steps where we performed the diffusion-drift approximation. In that case, we have neglected, in the equations for ρ_A and ρ_B, gradients of the density of the same species. In that approximation, the gradient expansion is truncated at the second order (cf. footnote at page 54). This approximation was done in order to be able to obtain the Fokker-Planck equation such as (3.8) and apply Itō calculus to derive the time evolution for the density fields ρ_A and ρ_B. Taking into account these higher order gradients would have required a completely different approach to our problem (see, for instance [47, 141]).

Then, within our derivation, we expect such corrections to be present in the equation for the dynamics of ρ_A and ρ_B as terms proportional to a fourth order gradient of ρ_A and ρ_B, respectively. The complete mean-field equation for phase separating systems with smooth interfaces then reads

$$\begin{aligned}\dot{\rho}_A(\mathbf{r},t) &= \nabla\left[D_A[\rho_B]\nabla\rho_A - \mathbf{F}_A[\rho_B]\rho_A\right] - \zeta\Delta^2\rho_A \\ \dot{\rho}_B(\mathbf{r},t) &= \nabla\left[D_B[\rho_A]\nabla\rho_B - \mathbf{F}_B[\rho_A]\rho_B\right] - \zeta\Delta^2\rho_B.\end{aligned} \tag{3.31}$$

3.4.3 Logistic growth in a two-species system

We now analyse more carefully the role of the logistic growth of the form (3.15), that we recall here:

$$\begin{aligned}\dot{\rho}_A &= \mu\rho_A\left(1 - \frac{\rho_A+\rho_B}{\rho_0}\right) \\ \dot{\rho}_B &= \mu\rho_B\left(1 - \frac{\rho_A+\rho_B}{\rho_0}\right).\end{aligned} \tag{3.32}$$

We claimed that this form is a reasonable approximation of the population growth in the experiments: the two species reproduce at the same rate μ, also called the birth rate, and compete for the same nutrients. Hence, a carrying capacity ρ_0 for the total population $\rho_A+\rho_B$. We now show that this choice entails a very subtle consequence.

3.4.3.1 Degeneracy of the solution

While in the single species case the fixed point $\rho=\rho_0$ is unique, in the case of two species – and in multispecies in general – the fixed point is given by $\rho_A+\rho_B=\rho_0$, which can happen for an infinite number of values of ρ_A and ρ_B. The fixed point of the dynamical system (2.9) is in fact a fixed line in the phase plane (ρ_A,ρ_B), as shown in Fig. 3.8.

To understand the properties of this line of fixed points, we study the behaviour of small perturbations around an arbitrary point on the line (ρ_A^0,ρ_B^0). The two eigenvalues of the dynamical matrix for the linearized system are $\sigma_1=0$ and $\sigma_2=-\mu$ and their corresponding eigenvectors are $\mathbf{x}_1=(1,-1)$ and $\mathbf{x}_2=(\rho_A^0,\rho_B^0)$. The first eigenvector is parallel to the line of fixed points: perturbations in that direction make the solution shift along

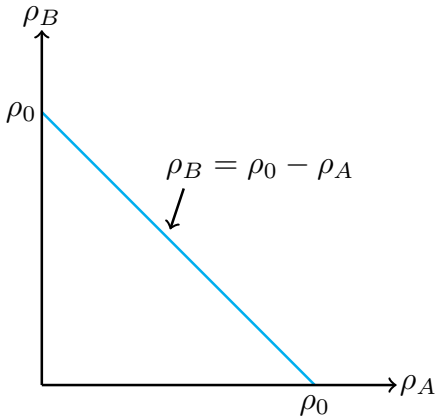

Figure 3.8 – Schematic representation of the line of fixed points such that $\rho_A + \rho_B = \rho_0$ in the phase plane (ρ_A, ρ_B).

the line without leaving it. On the other hand, the direction of the second eigenvector depends on the initial condition (ρ_A^0, ρ_B^0). Since σ_2 is negative, perturbations in the direction $\mathbf{x}_2$ decay bringing the solution back to the line of fixed points. Since one direction is neutral and the other one is stable, the line of fixed points is degenerate: in presence of noise, the solution may diffuse along the line.

3.4.3.2 The interplay with MIPS

In chapter 2 we have seen how the competition between the logistic growth and the MIPS mechanism can give rise to patterns with finite wavelength. The necessary condition for which the two dynamics are in competition is, of course, that the carrying capacity ρ_0 is within the instability range of the MIPS mechanism.

We now investigate the effect of a logistic term of the form (3.32) in a two-species system of run-and-tumble bacteria undergoing MIPS, obeying Eq. (3.17). Suppose that we start from a homogeneous unstable profile (ρ_A^0, ρ_B^0), such that $\rho_A^0 + \rho_B^0 = \rho_0$, the carrying capacity of Eq. (3.32). Then, a small perturbation grows, causing the system to separate in two phases which in principle do not lie on the line defined by $\rho_A^0 + \rho_B^0 = \rho_0$. In general, one of the two phases (let us call it phase 1) lies above the line of degenerate fixed points: $\rho_A^1 + \rho_B^1 = \rho_{\text{tot}}^1 > \rho_0$. The other phase (let us call it phase 2) lies instead below the line of degenerate fixed points: $\rho_A^2 + \rho_B^2 = \rho_{\text{tot}}^2 < \rho_0$. A schematic representation of a typical situation, underlying the differences between the case of mutual inhibition and mutual activation, is depicted in Fig. 3.9.

At this point, the instability due to the MIPS mechanism has lead the solution of Eq. (3.17) to a profile oscillating in space between two values $\rho_{\text{tot}}^1 > \rho_0$ and $\rho_{\text{tot}}^2 < \rho_0$, where 1 and 2 indicate the two phases. The logistic dynamics, on the other hand, tries to lead

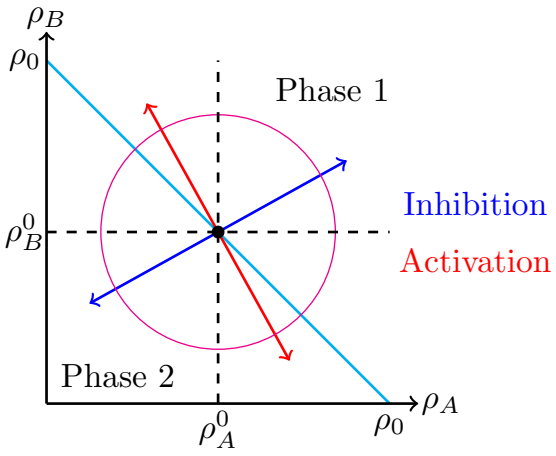

Figure 3.9 – Schematic representation, in the phase plane (ρ_A, ρ_B), of the MIPS phase diagram (the region inside the magenta circle is linearly unstable) with the line of fixed points (in cyan) such that $\rho_A + \rho_B = \rho_0$. The initial condition is at (ρ_A^0, ρ_B^0), in the unstable region and on the line of fixed points. A small perturbation causes the system to separate in two phases that lie outside the unstable region. In the case of mutual inhibition, the two phases are in the top-right and bottom-left quadrants (with respect to the initial condition), in the case of mutual activation they are in the top-left and bottom-right quadrants (with respect to the initial condition).

the solution towards a steady-state condition where $\rho_A^{ss} + \rho_B^{ss} = \rho_0$ everywhere. If the fixed point of the logistic dynamics $(\rho_A^{ss}, \rho_B^{ss})$ lies inside the unstable region, the two mechanisms are in competition, which once again gives rise to patterns of finite wavelength, as observed in experiments and simulations (cf. Figs. 3.1, 3.2, 3.3, and 3.4).

We recall that the typical size of a domain – that could be a droplet, a stripe, or a ring, depending on the initial conditions – is determined by the balance of two terms: the flux through the interface between phases 1 and 2, proportional to the length of the interface, and the creation or destruction of mass inside the different phases, proportional to the area of the domain. If for simplicity we assume that our pattern is an array of droplets, then at steady state, where there is no net mass transport, we have

$$0 = \dot{\rho}_{\text{tot}} = \pi R^2 \delta\rho - 2\pi R \phi, \tag{3.33}$$

where $\delta\rho$ is the rate of mass creation/destruction inside a droplet, ϕ the density flux through the interface, and R the typical radius of the droplet. From Eq. (3.33) we deduce the typical radius

$$R \propto \frac{\phi}{\delta\rho}. \tag{3.34}$$

Note now that the oscillation amplitude of $\rho_{\text{tot}} = \rho_A + \rho_B$ is in general larger in the case of

mutual inhibition, where the two oscillating profiles ρ_A and ρ_B are in-phase, than in the case of mutual activation, where the two oscillating profiles ρ_A and ρ_B are out-of-phase. In this last case, phases 1 and 2 may be such that the overall density $\rho_A + \rho_B$ is always very close to the carrying capacity (cf. Fig. 3.9). In the limit in which the coexistence densities lay on the line of fixed points, the mass production due to the logistic term tends to zero inside the droplet, and hence the radius of the droplet tends to infinity, as we can see from the relation (3.34). For finite systems, this corresponds to a radius comparable to the system size. We conclude that, for mutual activation, domains can become very large and eventually reach the size of any finite system. This case, which requires a symmetry of the system ($\rho_A \leftrightarrow \rho_B$ and ρ_{tot} in the two phases symmetric with respect to ρ_0), is illustrated in Fig. 3.10.

We stress that this fact does not exclude the scenario where the typical size of domains is smaller than the system size and patterns can be observed. In fact, for generic interactions, i.e. when $v_A(\rho_B) \neq v_B(\rho_A)$, we expect the coexistence phases[4] to be quite far from the line of fixed points[5]. This generically prevents arbitrarily large patterns. In addition, the coarsening dynamics is slow compared to the typical timescale at which the initial phase separation takes place [141], as we can observe in simulations (cf. Fig. 3.10). In the experiments, it is likely that at timescales where coarsening would take place, the colony has consumed most of the nutrients present in the environment and bacteria have become non-motile: the patterns are "frozen" in a metastable state, that cannot be exited unless energy is provided to reactivate the cells' functionality. To test this hypothesis, in future works it would be interesting to relate the bacterial motility to the concentration of nutrient.

We finally point out a subtlety caused by the degeneracy of fixed points discussed in section 3.4.3.1. In the single-species case, the fixed point ρ_0 is unique and can be chosen in such a way that it lies inside the MIPS unstable region, hence maintaining a competition between MIPS and logistic growth. In our model for multispecies systems, instead, it is perfectly plausible that among all the steady-state solutions $(\rho_A^{\text{ss}}, \rho_B^{\text{ss}})$, some lie outside the MIPS unstable region. Then, a rare fluctuation could make the system go from the pattern forming region to such an outlying profile, which could destroy the patterns

[4] It would indeed be very useful to be able to analytically compute the coexistence densities – binodals – for given interactions and initial conditions. Unfortunately, for non-equilibrium systems, no general methods are known for the analytical computation of the binodal lines. We show in section 4.2.1 a special case – of simple MIPS, i.e., without logistic growth – in which we are able to map our non-equilibrium active system to an equilibrium one at second order in gradients, highlighting the differences and similarities between the two.

[5] Note that this is what happens in the experiments, where the two species of bacteria are in general distinguishable. However, since we are not able to quantify the real interactions and their differences for different species, we adopt simple forms in order to limit the number of unknown fitting parameters.

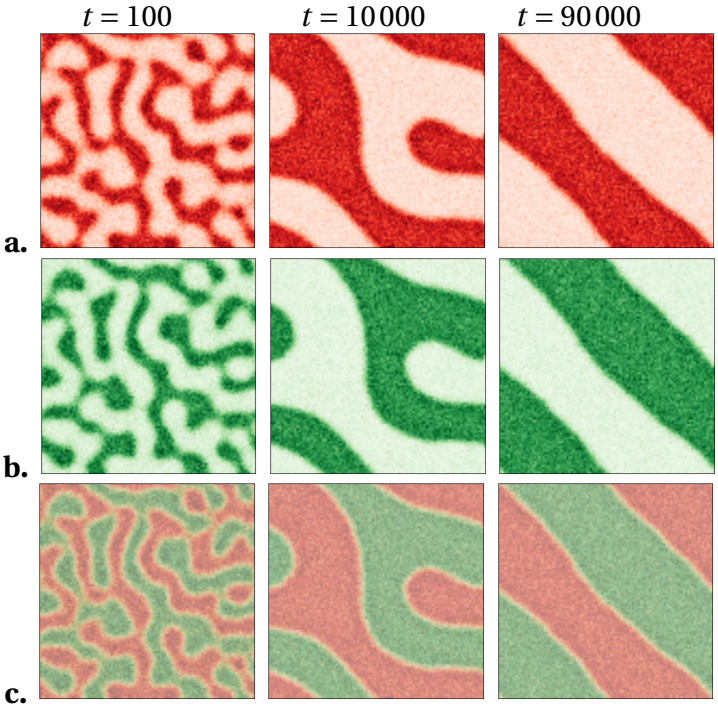

Figure 3.10 – Snapshots of an on-lattice simulation of a system with mutual activation interactions and birth-and-death dynamics, starting from homogeneous densities. We observe segregation of the two species and phase separation and a complete coarsening at steady state without formation of patterns with typical wavelength. We note that the two species are perfectly interchangeable in this simulation: this atypical symmetry makes the coexisting densities lie on the line $\rho_A + \rho_B = \rho_0$. Box size $L = 100$, initial number of particles $N_A = N_B = 500\,000$, $v_i(\rho_j) = v_0 + \frac{v_1 - v_0}{2}\left(1 + \tanh\left(\frac{\rho_j - \rho_m}{L_f}\right)\right)$, $v_0 = 0.1$, $v_1 = 4$, $\rho_m = 50$, $L_f = 30$, $\alpha = 1$, $b_0 = 0.1$, $d_0 = 0$, $d_1 = 0.001$. With this choice of birth and death rate we are introducing another symmetry: $\rho_0 = 100$, which corresponds to $2\rho_m$. The coarse-grained densities ρ_A and ρ_B are computed with a quasi-circular interaction kernel of radius $r_0 = 3$. **a.** Density of species A. **b.** Density of species B. **c.** Total density $\rho = \rho_A + \rho_B$.

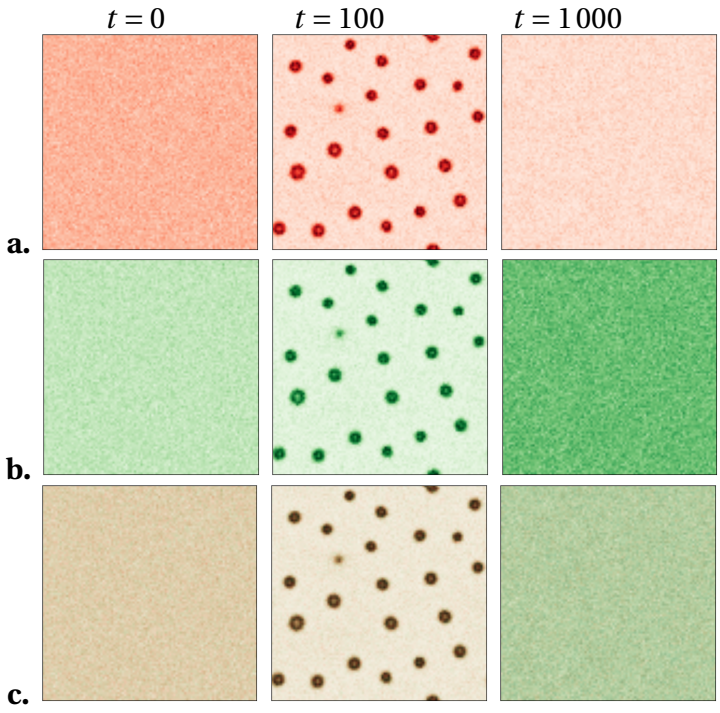

Figure 3.11 – Snapshots of an on-lattice simulation of a system with mutual inhibition interactions, starting from homogeneous densities. At intermediate state, we observe micro-phase separation with patterns with finite wavelength. At steady state, the system relaxes to stable homogeneous profiles whose values differ from the initial condition ones. Box size $L = 100$, initial number of particles $N_A = N_B = 400\,000$, $v_i(\rho_j) = v_1 + \frac{v_0 - v_1}{2}\left(1 - \tanh\left(\frac{\rho_j - \rho_m}{L_f}\right)\right)$, $v_1 = 0.1$, $v_0 = 8$, $\rho_m = 50$, $L_f = 20$, $\alpha = 1$, $b_0 = 0.1$, $d_0 = 0$, $d_1 = 0.001$. The coarse-grained densities ρ_A and ρ_B are computed with a quasi-circular interaction kernel of radius $r_0 = 3$. **a.** Density of species A. **b.** Density of species B. **c.** Total density $\rho = \rho_A + \rho_B$.

(cf. Fig. 3.9). An example of this situation is shown for the case of mutual inhibition in Fig. 3.11. We note, however, that for this particular situations to occur, a lot of mass needs to be moved from high density to low density regions, or created and destructed. Once again, in experiments, this typically happens at long times, by which the bacteria have already consumed the nutrients and have become non-functional.

3.5 Controlling patterns: the case of three species

We now present some results on systems of three different interacting species of *E. coli*. The goal of this work is to show that it is possible to control the spatial organization in bacterial colonies with density-modulated motility, using the principles deciphered for two species.

The strategy is the following: A and B are a couple of mutually inhibiting species. The engineered genetic circuits that produce this mutual interaction are the same as those shown in Fig. 3.1-a. Hence, when A and B interact, they develop colocalized patterns. Then, two other species, called sensor C and sensor D, are engineered in such a way that they respond to the signals produced by species B, namely the AHL molecules called 3oc6HSL. In particular, sensor C responds by suppressing the expression of *cheZ*, hence by reducing its transport efficiency: we can say that its motility is inhibited by B. Sensor D, on the contrary, responds by enhancing the expression of *cheZ*, therefore increasing its transport efficiency: its motility is activated by B.

The experimental results are shown in Fig. 3.12, where the geometry of the setup is different from previous experiments: instead of a central inoculum, the growth of cell mixture is initiated along a thin line in the middle of the semisolid agar plate. To visualize the different species, A and B are tagged with the sfGFP fuorescent molecule (green), while C and D are tagged with mCherry (red). The results are consistent with the generic strategy discussed so far. When the motility of sensor C is inhibited by the local density of species B, the population of sensor C shows synchronous in-phase oscillations with species A and B, resulting in colocalized stripe patterns. On the other hand, when inhibited, the population of sensor D exclusively aggregates in the low density regions, showing a major segregation from the high density stripes of species A and B. Numerical simulations are in agreement with the experimental results (see Figs. 3.13 and 3.14).

The three-species experiments show a novel mechanism allowing to control spatial organization in motile bacteria. Sensors C and D dynamically respond to the presence of an inducer, namely the AHL secreted by strain B, which controls their motility. In the experiment, the inducer is localized in sequential stripes, as a consequence of the inhibition interaction of species B with species A. To use the terminology of chapter 1, the couple of inhibitors A and B act as a prepattern that modulates the spatial organization of sensors C and D.

3.6 Conclusion and perspectives

Chapters 2 and 3 were dedicated to the study of pattern formation in bacterial colonies, where the leading interaction mechanism is the modulation of the motility of self-propelled particles depending on the local density. This mechanism allows particles to self-organize in space, without the need to impose any condition from the outside, such as external fields or spatial cues.

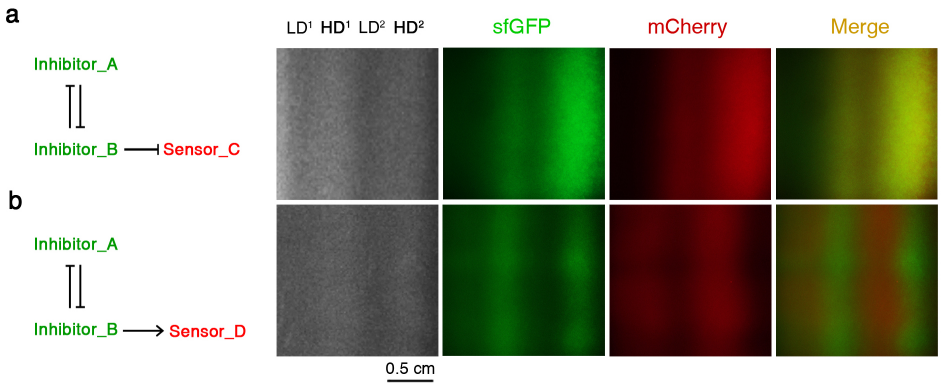

Figure 3.12 – Sensor strains C and D are respectively mixed by a low fraction (1%) with strains A and B, called "inhibitors". The three species mixture is linearly inoculated in semisolid agar plate. Left panels of **a** and **b**: schematic representations of the interaction loop among three engineered strains. Right panels: darkfield snapshots of stripe patterns (first column) formed by the three species systems. LD indicates a low density stripe, while HD indicates a high density stripe. The distributions of each strain are shown in sfGFP (inhibitors A and B), mCherry (sensors C and D), and merged fluorescent channels (see online version if contrast in printed version does not allow a clear view of the patterns).

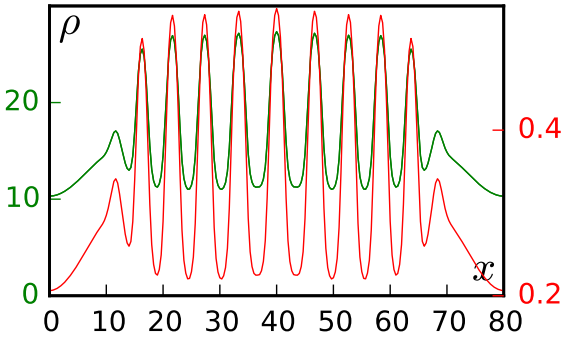

Figure 3.13 – Density profiles along a cut of a 2D numerical solution of Eqs. (3.17) for a couple of inhibitors A and B, with the addition of a third equation for sensor C, whose motility parameters depending on ρ_B. The initial condition is a linear central inoculum. The inhibitors' density is shown in green (A and B superposed): they form in-phase spatial oscillations. The sensor's density is shown in red: it oscillates in-phase with its inhibitor B. Box size $L = 80$, initial conditions $\rho_A^0/\rho_B^0 = 1$, $\rho_B/\rho_C^0 = 200$, $\beta_i(\rho_j) = \beta_0 + \frac{\beta_1-\beta_0}{2}\left(1 - \tanh\left(\frac{\rho_j-\rho_m}{L_f}\right)\right)$, $\beta_0 = 0.5$, $\beta_1 = 5$, $\rho_m = 15$, $L_f = 5$, $\alpha = 3$, $\nu = 2.5$, $\zeta = 0.1$, $\mu = 0.1$.

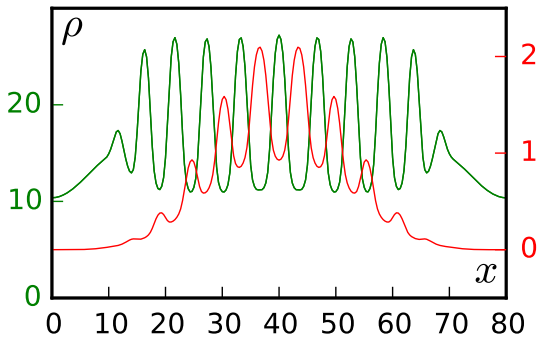

Figure 3.14 – Density profiles along a cut of a 2D numerical solution of Eqs. (3.17) for a couple of inhibitors A and B, with the addition of a third equation for species C, whose motility parameters depending on ρ_B. The initial condition is a linear central inoculum. The inhibitors' density is shown in green (A and B superposed): they form in-phase spatial oscillations. The sensor's density is shown in red: it oscillates out-of-phase with respect to its activator B. Box size $L = 80$, initial conditions $\rho_A^0/\rho_B^0 = 1$, $\rho_B/\rho_C^0 = 50$, $\beta_0 = 0.5$, $\beta_1 = 5$, $\rho_m = 15$ and $L_f = 5$, $\alpha = 3$, $\nu = 2.5$, $\zeta = 0.1$, $\mu = 0.1$.
$\beta_i(\rho_j) = \beta_0 + \frac{\beta_1-\beta_0}{2}\left(1 - \tanh\left(\frac{\rho_j-\rho_m}{L_f}\right)\right)$, with $i, j \in \{A, B\}$.
$\beta_C(\rho_B) = \beta_0 + \frac{\beta_1-\beta_0}{2}\left(1 + \tanh\left(\frac{\rho_B-\rho_m}{L_f}\right)\right)$.

The coarse-graining procedure developed in sections 2.2.1 and 3.3.1 allows to create a direct connection between the experiments and the underlying pattern formation mechanisms, by taking into account both the precise interactions among the particles and the finite tumble duration, which play a crucial role in the experiments. When two species are present, it is possible to implement mutual interactions. By examining in detail the characteristic of these interactions, we were able to predict the different behaviours that we observe in experiments. The remarkable resemblance of numerical simulations of the macroscopic equations with the experimental results not only validates our model and approximations, but suggest that this mechanism is very robust. Indeed, we neglected many details of the experiments, from the chemical fields to hydrodynamics, to behavioural polydispersity or the presence of agar. The fact that our theory still describes very well the experiments suggests that the underlying pattern formation mechanism should be very robust and hence generically encountered in Nature.

From a practical point of view, we have set the basis to start analysing how to tune the parameters in order to obtain desired patterns. The case of three species experiments and simulations, where a species is engineered in such a way as to follow a given prepattern, is an instructive example. Moreover, it would be interesting to study how patterns are modified by varying some conditions, such as for example the difference between the

transport efficiency in dense or dilute regions.

In the same train of thought, a very interesting perspective is that of bridging the quantitative gap between the experiments and the theory, by finding optimal fitting parameters for the model that could be measured in the real colonies of bacteria. This improvement is directly related to the progress in imaging techniques and algorithms capable of processing data relative to large numbers of particles and extracting the relevant fitting parameters. A good candidate for this purpose is Differential Dynamic Microscopy which allows to measure parameters such as the speed of the particles or the fraction of non-motile cells without the need of single-cell tracking [94].

Chapter 4

Motility-induced phase separation in multispecies systems

The results on two-species mutually interacting run-and-tumble bacteria found in chapter 3 open up exciting scenarios on the behaviour of multispecies systems of motile particles. We already showed in section 3.5 an interesting application of the MIPS mechanisms for systems of three species, where two mutually inhibitor species self-organize and control the spatial distribution of a third species. In this chapter we present some preliminary results on the general case in which N species coexist and interact, starting from the case where each species interacts with any other, but not with itself (no self-regulation of the motility). Note that in multispecies systems the interactions that we consider are still inhibition and activation of motility; the question, then, is if, and eventually how, it is possible to combine them between the different species in order to obtain a given self-organization of the system.

For the sake of simplicity, we work within the approximation of instantaneous tumbles, in order to deal with simpler equations. The theory developed in chapter 2 ensures that a generalization to systems with finite tumble duration is straightforward.

We study the stability of homogeneous profiles in simple cases for which general conditions can be found to observe phase separation and show how it is possible to predict the spatial organization of the different species in phase separated systems. At the end of the chapter we discuss a mapping to equilibrium systems, highlighting differences and similarities between such systems and our active ones.

4.1 Linear analysis and results

We consider a system composed of N species interacting by quorum sensing motility-regulation: a generic scenario is that motility of species i is modulated by the density of all species $j \neq i$, where we have not considered self-interactions. We hence assume

that the speed of particles of species i can vary with $\rho_{j\neq i}$: $v_i = v_i(\{\rho_{j\neq i}\})$, where $\{\rho_{j\neq i}\} = \rho_1,\dots,\rho_{i-1},\rho_{i+1},\dots,\rho_N$. In particular, we consider a speed v_i that depends on the *sum* of the densities $\sum_{j\neq i}\rho_j$: physically, this may indicate that species i responds to the integrated signal coming from all the other species.

We consider a coarse-graining such as the one performed in last chapters (cf. sections 2.2.1 and 3.3.1), which can be easily generalized to the N-species case, and start directly from the time evolution for the densities of the different species. Considering a mean-field approximation and locality of the interactions, the system of coupled equations reads

$$\dot{\rho}_i = \nabla\cdot\left[v_i^2\nabla\rho_i + \rho_i v_i \nabla v_i\right], \tag{4.1}$$

where the time derivative is performed with respect to a rescaled time $t' = d\alpha t$, where d is the number of spatial dimensions and α the tumbling rate (cf. Eq. (2.5)). We consider a solution $\rho_i = \rho_i^0 \forall i$ where all densities are homogeneous and study the effects of a perturbation around such profiles. The linearized system reads $\dot{\boldsymbol{\delta\rho}}_q = -q^2 M\boldsymbol{\delta\rho}_q$, where M is a $N\times N$ linear stability matrix, which takes the form

$$\begin{aligned} M_{ii} &= v_i^2 \\ M_{ij} &= v_i\rho_i^0\frac{\partial v_i}{\partial\rho_j}, \end{aligned} \tag{4.2}$$

where the speeds and their derivatives are evaluated at $\rho_1^0,\dots,\rho_N^0$.

In order to have an instability, M must have at least one eigenvalue with negative real part. Since $\operatorname{tr} M > 0$, there is always at least one positive eigenvalue. If $N = 2$, as in the previous chapter, a necessary and sufficient condition for another eigenvalue to be negative is than that $\det M < 0$. However, for $N > 2$, the condition $\det M < 0$ is sufficient, but not necessary: if there exist negative eigenvalues, but their number is even, then $\det M > 0$.

Suppose now that we have a non-interacting system or a very dilute one. Then M_{ij} can be neglected and M is a diagonal matrix with strictly positive eigenvalues v_i^2: the system is stable. Since the eigenvalues are continuous functions of the matrix elements, if we continuously increase the interactions or the densities, the onset of instability happens when the real part of one eigenvalue vanishes. If the eigenvalues are real, this is equivalent to $\det M = 0$. However, if there are complex eigenvalues, they always appear by complex conjugate pairs (because M is real). Therefore, their real part can vanish while the determinant remains positive.

Without some simplifications of the matrix M, not much can be said on its spectrum and hence on the stability of Eqs. (4.1). In the next two sections we consider particular cases where the eigenvalues can be calculated analytically and we discuss the nature of

the phase separations that we can obtain.

4.1.1 Fully-connected interactions

We start with a case where we assume that the functional forms of the speeds of all species are equal; this assumption thus requires that all species interact by either inhibition or activation of motility. We also assume that all the homogeneous profiles are the same: $\rho_j^0 = \rho_0 \ \forall j$. In this way, the speeds of all species and their derivatives are evaluated at the same value, i.e. $\rho_0^{\text{tot}} - \rho_0$, where $\rho_0^{\text{tot}} = N\rho_0$, since we assumed the speed to depend on the sum of the other densities. This choice allows for simpler calculations while not altering qualitatively the results: the instability conditions might be less general, but more informative about the expected behaviour (colocalization, segregation, others...).

The stability matrix in this case is composed of two constant terms, one for the diagonal entries, the other for the off-diagonal ones:

$$\begin{aligned} M_{ii} &= v^2 \\ M_{ij} &= v\rho_0 \frac{\partial v}{\partial \rho}, \end{aligned} \tag{4.3}$$

where $\rho = \sum_i \rho_i$ and v and $\partial_{\rho_j} v$ are evaluated in $\rho_0^{\text{tot}} - \rho_0$. The spectrum of the matrix (4.3) can now be easily calculated in the cases $N = 3, 4, \ldots$, and the general case deduced:

$$\begin{aligned} \sigma_1 = \sigma_2 = \cdots = \sigma_{N-1} &= v^2 - v\rho_0 \frac{\partial v}{\partial \rho} \\ \sigma_N &= v^2 + (N-1)\, v\rho_0 \frac{\partial v}{\partial \rho}. \end{aligned} \tag{4.4}$$

We observe that the stability of the system depends on the sign of $\partial_\rho v$. We start by considering the case $\partial_\rho v < 0$, i.e. where all species interact by inhibition of the motility. In this case the $N-1$ eigenvalues $\sigma_1 = \sigma_2 = \cdots = \sigma_{N-1}$ are positive, hence stabilizing, while the last eigenvalue σ_N can be negative and give rise to an instability. The eigenvector associated to σ_N is of the form $\mathbf{x}_N = (1, 1, \ldots, 1)$: if a perturbation makes the density of species i become larger (resp. smaller), then all the other densities increase (resp. decrease) with ρ_i one and we then observe colocalization of N species (see Fig. 4.1).

If we now consider the case $\partial_\rho v > 0$, we observe that the eigenvalue σ_N is positive, hence stabilizing, while the $\sigma_1 = \sigma_2 = \cdots = \sigma_{N-1}$ can become unstable. As for the eigenvectors, their general form is $\mathbf{x}_{ij} = (0, \ldots, 0, -1, 0, \ldots, 0, 1, 0, \ldots, 0)$, where the i^{th} entry is equal to -1 and the j^{th} to $+1$. If $\mathbf{x}_{ij}$ is one eigenvector, then the other $N-2$ are such that the entry -1 is fixed at position i, while the entry $+1$ is different for each eigenvector,

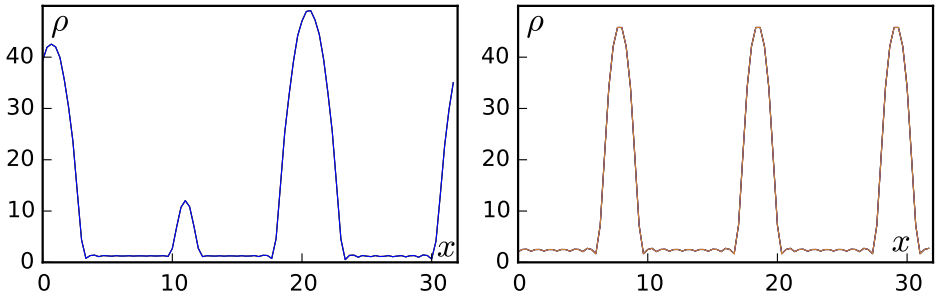

Figure 4.1 – Numerical solutions of Eqs. (4.1) with the addition of a stabilizing term of the type $-\zeta\Delta^2\rho_i$ (cf. discussion in 2.2.2.1) in 1D for a fully connected system: the case of colocalization. **Left**: three-species system. The three densities, colored in red, green, and blue are perfectly superposed. Box size $L = 32$, initial conditions $\rho_i = 11 + \delta\rho_i$, where $i \in \{1,2,3\}$ and $\delta\rho_i$ is a random perturbation of the order 10^{-2}, $v(\rho) = v_0 \exp\big(-\lambda\rho\big)$, $\rho = \sum_{i=1}^{3}\rho_i$, $v_0 = 1$, $\lambda = 0.2$, $\alpha = 1$, $\zeta = 0.001$. **Right**: four-species system. The four densities, colored in red, green, blue, and yellow are perfectly superposed. Box size $L = 32$, initial conditions $\rho_i = 11 + \delta\rho_i$, where $i \in \{1,2,3,4\}$ and the $\delta\rho_i$'s are smooth undulations of amplitude $A = 2$, $v(\rho) = v_0 \exp\big(-\lambda\rho\big)$, $\rho = \sum_{i=1}^{4}\rho_i$, $v_0 = 1$, $\lambda = 0.2$, $\alpha = 1$, $\zeta = 0.001$.

with $j \neq i$. For instance, they can take the forms:

$$\begin{aligned}
&\mathbf{x}_{1,2} = (-1,1,0,0,\ldots,0,0)\\
&\mathbf{x}_{1,3} = (-1,0,1,0,\ldots,0,0)\\
&\ldots\\
&\mathbf{x}_{1,N} = (-1,0,0,0,\ldots,0,1).
\end{aligned} \tag{4.5}$$

If a perturbation makes density of species i become, say, larger, then all the other densities tend to become smaller where ρ_i grows. Then, since all densities are interchangeable, the same dynamics is applicable to any of them: where any ρ_j accumulates, all the others become sparse. We then observe total segregation: the space is divided into N regions[1], each one densely populated by one species (see Fig. 4.2). Finally, note that the linear analysis does not tell us how the different domains are organized, i.e. which domains are in contact and which are instead far from each other.

4.1.2 "Chain interactions"

We now treat the case in which the motility of species $j-1$ is modulated only by the density of species j, and the motility of species j is modulated only by the density of species

[1]We note that at first there are $n > N$ regions where the presence of one species is predominant with respect to the others, then a coarsening dynamics makes small regions disappear and large regions become larger.

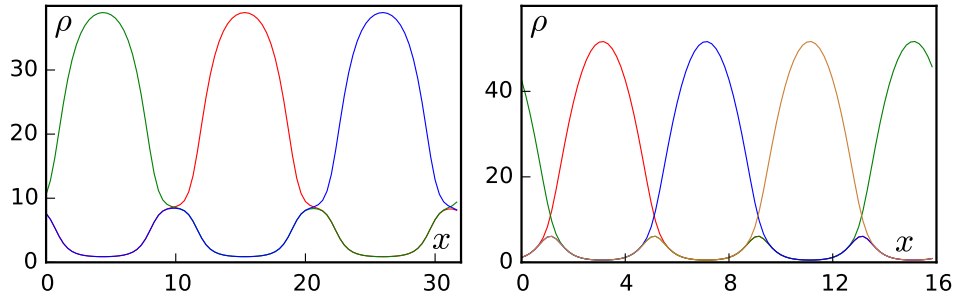

Figure 4.2 – Numerical solutions of Eqs. (4.1) with the addition of a stabilizing term of the type $-\zeta\Delta^2\rho_i$ (cf. discussion in 2.2.2.1) in 1D for a fully connected system: the case of total segregation. **Left**: three-species system. The three densities, colored in red, green, and blue organize in three domains, in each of which one species is dense and the other two are sparse. Box size $L = 32$, initial conditions $\rho_i = 11 + \delta\rho_i$, where $i \in \{1,2,3\}$ and $\delta\rho_i$ is a random perturbation of the order 10^{-2}, $v(\rho) = v_0 \exp(\lambda\rho)$, $\rho = \sum_{i=1}^{3}\rho_i$, $v_0 = 1$, $\lambda = 0.1$, $\alpha = 1$, $\zeta = 0.006$. **Right**: four-species system. The four densities, colored in red, green, blue, and yellow organize in four domains, in each of which one species is dense and the other three are sparse. Box size $L = 16$, initial conditions $\rho_i = 11 + \delta\rho_i$, where $i \in \{1,2,3,4\}$ and $\delta\rho_i$ is a random perturbation of the order 10^{-3}, $v(\rho) = v_0 \exp(\lambda\rho)$, $\rho = \sum_{i=1}^{4}\rho_i$, $v_0 = 1$, $\lambda = 0.1$, $\alpha = 1$, $\zeta = 3$.

$j+1$. We set $j-1 = N$ if $j = 1$ and $j+1 = 1$ if $j = N$ in order to close the loop, and refer to this model as "chain interactions". As in the previous case, we assume that the form of the speed v is the same for all species and that all species have the same initial density, so that v and its derivatives are evaluated in $(N-1)\rho_0$. The $N \times N$ linear stability matrix M now reads

$$M = \begin{pmatrix} v^2 & \rho v\partial_\rho v & 0 & \dots & 0 \\ 0 & v^2 & \rho v\partial_\rho v & \dots & 0 \\ 0 & 0 & v^2 & \dots & 0 \\ \vdots & \vdots & \vdots & \ddots & \vdots \\ \rho v\partial_\rho v & 0 & 0 & \dots & v^2 \end{pmatrix}. \tag{4.6}$$

The characteristic polynomial of M can be easily calculated by expanding with respect to the first column: $(v^2-\sigma_k)(v^2-\sigma_k)^{N-1} = (-1)^N(\rho v\partial_\rho v)(\rho v\partial_\rho v)^{N-1}$, which gives

$$(v^2-\sigma_k)^N = (-\rho v\partial_\rho v)^N, \tag{4.7}$$

where the σ_k's are the N eigenvalues of M. From (4.7) we compute their general form:

$$\sigma_k = v^2 + e^{\frac{2\pi ik}{N}}\rho v\partial_\rho v. \tag{4.8}$$

Note that

$$\sigma_k = \sigma^*_{N-k}, \tag{4.9}$$

where the star indicates the complex conjugate.

We now analyse the spectrum (4.8) by looking at the different values that k can take. We start by setting $k = N$. In this case we have that

$$\sigma_N = v^2 + \rho v \partial_\rho v, \tag{4.10}$$

which can lead to an instability qualitatively identical to the one of σ_N in (4.4), since their eigenvectors are of the form $\mathbf{x}_N = (1, 1, \dots, 1)$. Hence, when σ_N becomes negative, which can happen for $\partial_\rho v < 0$, the system evolves towards a colocalization of all species.

If N is even, then we can consider $k = N/2$. In this case, we obtain

$$\sigma_{\frac{N}{2}} = v^2 - \rho v \partial_\rho v, \tag{4.11}$$

which can lead to an instability when $\partial_\rho v > 0$. The eigenvector associated with $\sigma_{\frac{N}{2}}$ now takes the form $\mathbf{x}_{\frac{N}{2}} = (-1, 1, -1, \dots, 1)$, which can be interpreted in the following way: when a small perturbation makes ρ_j grow, then its "neighbours" ρ_{j-1} and ρ_{j+1}, i.e. the two species j interacts with, decrease. We therefore observe a "partial" segregation of the system in two domains: in one domain the non-interacting species $\{\rho_{2j}\}$ coexist, while in the other we find the remaining $\{\rho_{2j+1}\}$, also non-interacting. Even though some species in domain 1 do not interact with some species in domain 2, the two domains remain immiscible, thanks to the "chain interactions". The $N-2$ remaining eigenvalues for which $k \neq N, N/2$, are complex and cannot give rise to stationary phase separated solutions.

When N is odd no eigenvalue such as $\sigma_{\frac{N}{2}}$ exists, and hence the only real eigenvalue is σ_N, while the remaining $N-1$ eigenvalues with $n \neq N$ are complex. The fact that σ_N can be negative only for $\partial_\rho v < 0$ implies that if N is odd it is not possible to obtain stationary segregated profiles. This does not come as a surprise: we have seen that when N is even, activation interactions make the system organize in two separated domains, one containing the non-interacting species $\{\rho_{2j}\}$ and the other containing the non-interacting species $\{\rho_{2j+1}\}$. When N is odd, there is no way to arrange the system in such a way that two interacting species are not in the same domain; the system is *frustrated* and cannot be stationary, as predicted by the fact that the eigenvalues are complex. For example, if we take $N = 3$, we would have that species 1 and 2 become segregated, because 2 activates 1. Then, species 3, which is activated by species 1, would tend to segregate from it, going towards the regions occupied by species 2. By doing so, species 2, activated by species 3,

moves towards regions occupied by species 1 and the cycles starts over: the three mutually activating species cannot be stationary.

We now consider the general case (4.8). We rewrite it as

$$\sigma_k = v^2 + \cos\left(\frac{2\pi k}{N}\right)\rho v\partial_\rho v + i\sin\left(\frac{2\pi k}{N}\right)\rho v\partial_\rho v. \tag{4.12}$$

to emphasize the real and imaginary parts:

$$\begin{aligned} \mathrm{Re}(\sigma_k) &= v^2 + \cos\left(\frac{2\pi k}{N}\right)\rho v\partial_\rho v \\ \mathrm{Im}(\sigma_k) &= \sin\left(\frac{2\pi k}{N}\right)\rho v\partial_\rho v. \end{aligned} \tag{4.13}$$

We note that if N is a multiple of 4, then the eigenvalues with $k = N/4$ and $k = -N/4$ always have a positive real part:

$$\sigma_{k=\pm\frac{N}{4}} = v^2 \pm i\rho v\partial_\rho v \tag{4.14}$$

and therefore can never give rise to an instability. In all the remaining cases, i.e. when $k \neq N$, $k \neq N/2$, and $k \neq N/4$, the σ_k's always have a real part that can become negative and an imaginary part, which leads to oscillating solutions. In particular:

1. if $k < N/4$, $\cos\left(\frac{2\pi k}{N}\right) > 0$ and $\mathrm{Re}(\sigma_k) < 0$ for $\partial_\rho v < 0$;
2. if $k > N/4$, $\cos\left(\frac{2\pi k}{N}\right) < 0$ and $\mathrm{Re}(\sigma_k) < 0$ for $\partial_\rho v > 0$.

An example of oscillating solution is shown in Fig. 4.3 for the case $N = 3$. In the simulation, we first observe the appearance of travelling waves, until, at larger timescales, the solution becomes a standing wave. The final regime is shown in the figure.

4.1.3 Discussion

We have seen how spatial organization in multispecies systems is in general a highly nontrivial problem to treat analytically. Nevertheless, in the last two sections we have shown that in some cases the problem can be simplified and analytical solutions found. These cases give very strong insights on what type of macroscopic behaviours and structures we expect to observe, given a set of mutually inhibiting, activating, or mixed species.

We have indeed acquired enough knowledge in order to state a principle that can be used in order to predict the type of phase separation we expect to observe, given the interactions among the species: in general, when species i is "inhibited" by species j, the

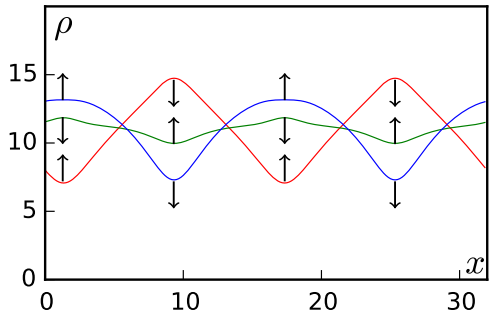

Figure 4.3 – Numerical solutions of Eqs. (4.1) with the addition of a stabilizing term of the type $-\zeta\Delta^2\rho_i$ (cf. discussion in 2.2.2.1) in 1D for a three-species system with chain interactions: the different densities oscillate. Box size $L = 32$, initial conditions $\rho_i = 11+\delta\rho_i$, where $i \in \{1,2,3\}$ and $\delta\rho_i$ is a random perturbation of the order 10^{-2}, $v_i(\rho_j) = v_0 \exp\big(\lambda\rho_j\big)$, with $\{i,j\}$ a cyclic permutation of $\{1,2,3\}$, $v_0 = 1$, $\lambda = 0.2$, $\alpha = 1$, $\zeta = 0.5$.

former tends to accumulate in the regions where the latter is dense; on the other hand, when species i is "activated" by species j, the former tends to accumulate far away from regions where the latter is dense. By using this principle, one can predict the colocalization and segregation of several different species, even in the case where mutual inhibition and mutual activation interactions are present. One expects to find steady configurations when all the interactions are "satisfied": consider for instance the case $N = 3$ with chain interactions. If species 2 activates species 1, then 1 segregates from 2. If we now take species 3 in such a way that it *is inhibited* by species 1 and that it *activates* species 2, then we see that it can colocalize with species 1, and we obtain a phase separated system where species 1 and 3 coexist and are segregated from species 2. We can play this game with a generic number of species, and observe that we can always find some combination of the interactions in such a way to obtain a phase separated steady state. Note that in general, when such a loop of colocalization/segregation cannot be closed, such as in the case of three "chain activating" species of Fig. 4.3, the system becomes frustrated and it cannot reach a steady state. We observe instead travelling or standing waves.

4.2 Mapping to equilibrium

In this section we show how it is sometimes possible to map our multispecies system of self-propelled particles with quorum sensing interactions to an equilibrium system whose dynamics derives from a free energy, at leading order in gradients. In the case of single-species systems of self-propelled particles, it has been shown that at the local

approximation level, i.e. neglecting higher order gradient terms arising from the non-locality of interactions (cf. section 2.2.2.1), the dynamics satisfy detailed balance at macroscopic scales [139, 24, 25]. Then, a free energy functional of the form

$$\mathscr{F}[\rho] = \int \mathrm{d}x \rho(\ln\rho - 1) + \mathscr{F}_{\mathrm{ex}}, \tag{4.15}$$

where $\mathscr{F}_{\mathrm{ex}}$ is the excess free energy, can be defined, and the steady state probability is given by $P[\rho] \propto \exp\big(\mathscr{F}[\rho]\big)$[2].

Following this approach, we consider a multispecies system with local interactions and work within a mean-field approximation. We look for the conditions under which a free energy functional $\mathscr{F}[\{\rho_n\}]$ of all the densities $\{\rho_n\}$ exists. In such a case, the dynamics of the density of species i satisfies:

$$\dot{\rho}_i = \nabla\left[\frac{v_i^2(\{\rho_{n\neq i}\})\rho_i}{2\alpha}\nabla\big(\ln\rho_i + \ln v_i(\{\rho_{n\neq i}\})\big)\right] = \nabla\left[M_i(\rho_i,\{\rho_{n\neq i}\})\nabla\frac{\delta\mathscr{F}}{\delta\rho_i}(\{\rho_n\})\right], \tag{4.16}$$

where we have considered non-self-interacting particles (the speed of species i does not depend on the density of species i). We look for free energy functionals of the form

$$\mathscr{F}(\{\rho_n\}) = \int \mathrm{d}x f(\{\rho_n\}), \tag{4.17}$$

where $f(\{\rho_n\})$ is the free energy density of all species $\{\rho_n\}$. From Eq. (4.16) we obtain

$$f(\{\rho_n\}) = \sum_n \rho_n(\ln\rho_n - 1) + f_{\mathrm{ex}}(\{\rho_n\}), \tag{4.18}$$

where $\sum_n \rho_n(\ln\rho_n - 1)$ is the free energy density for a perfect gas, and the function $f_{\mathrm{ex}}(\rho_A,\rho_B)$ is the excess free energy density, defined by

$$\partial_{\rho_i} f_{\mathrm{ex}} = \ln v_i(\{\rho_{n\neq i}\}). \tag{4.19}$$

Schwarz's theorem then states that if $\partial^2_{\rho_i\rho_j} f$ and $\partial^2_{\rho_j\rho_i} f$ both exist and are continuous at any given point $\{\rho_n^0\} = (\rho_1^0,\ldots,\rho_N^0)$, then

$$\frac{\partial^2}{\rho_i\rho_j} f(\{\rho_n^0\}) = \frac{\partial^2}{\rho_j\rho_i} f(\{\rho_n^0\}). \tag{4.20}$$

[2]Note that the local approximation does not correctly describe the coexisting densities in phase separated systems. To be able to make quantitative predictions, it is necessary to take into account higher order terms, as shown in [134]. Here, we limit ourselves to the study of the case of local interactions, leaving the treatment of higher order gradients for future work.

Eq. (4.20) is equivalent to

$$\frac{\partial^2}{\rho_i \rho_j} f_{\text{ex}}(\{\rho_n^0\}) = \frac{\partial^2}{\rho_j \rho_i} f_{\text{ex}}(\{\rho_n^0\}) \quad \Longrightarrow \quad \frac{\partial_{\rho_i} v_j(\{\rho_{n\neq j}\})}{v_j(\{\rho_{n\neq j}\})} = \frac{\partial_{\rho_j} v_i(\{\rho_{n\neq i}\})}{v_i(\{\rho_{n\neq i}\})}. \tag{4.21}$$

Since the left hand side of Eq. (4.21) cannot be a function of ρ_j and its right hand side cannot be a function of ρ_i, they must be equal to the same function $g_{i,j}(\{\rho_{n\neq i,j}\})$, constant with respect to the variables ρ_i and ρ_j. This yields

$$v_i(\{\rho_{n\neq i}\}) = v_i^0 \exp\big(\rho_j g_{i,j}\big) \quad \text{and} \quad v_j(\{\rho_{n\neq j}\}) = v_j^0 \exp\big(\rho_i g_{i,j}\big). \tag{4.22}$$

Since this must hold for all pairs (i, j), with $i, j \in \{1, \ldots, N\}$, we conclude that the function $g_{i,j}$ must be of the form

$$g_{i,j} = \lambda \prod_{n\neq i,j} \rho_n, \tag{4.23}$$

with λ a real constant, from which we obtain

$$v_i(\{\rho_{n\neq i}\}) = v_i^0 \exp\left(\lambda \prod_{n\neq i} \rho_n\right). \tag{4.24}$$

Our free energy density then takes the form

$$f(\{\rho_n\}) = \sum_n \rho_n(\ln \rho_n - 1) + \lambda \prod_n \rho_n. \tag{4.25}$$

In single-species systems, phase coexistence densities can be (relatively) easily computed by searching for concavities of the free energy density $f(\rho)$ and then performing a common-tangent construction. In the multispecies case, however, $f(\{\rho_n\})$ is an N-dimensional surface and the common tangent becomes a common N-dimensional plane, in general very hard to find. Combinations of analytical and numerical tools can be used in order to predict phase equilibria in polydisperse systems (see, for example, [130, 131] for an overview). In this thesis, we consider the simpler problem in which $N = 2$, and leave the general case for future investigation.

4.2.1 A special case: two-species systems

When $N = 2$, we come back to our notation where we call species 1 and 2, A and B, respectively. Our free energy density now reads

$$f(\rho_A, \rho_B) = \rho_A(\ln \rho_A - 1) + \rho_B(\ln \rho_B - 1) + \lambda \rho_A \rho_B \tag{4.26}$$

where the speeds of the two species have become

$$v_i(\rho_j) = v_0 \exp\big(\lambda \rho_j\big), \tag{4.27}$$

with $i, j \in \{A, B\}$. The sign of λ determines whether the two species are mutually inhibiting ($\lambda < 0$), or mutually activating ($\lambda > 0$).

4.2.1.1 Linear instability: spinodal lines

To begin with, we use the free energy density (4.26) to compute the onset of spinodal decomposition – i.e. the phase separation process occurring through the exponential growth of small fluctuations, eventually arrested by nonlinear effects – and we show, as expected, that it leads to the same condition for instability that we found with our linear analysis in section 3.4.1.

For a monodisperse system that admits a free energy, the spinodal region is determined by imposing that the second derivative of the free energy density is negative, corresponding to the regions where the free energy is concave. For bidisperse systems, the free energy is a function of ρ_A and ρ_B, hence a surface defined on the (ρ_A, ρ_B) plane. If we define the Hessian matrix H of f,

$$H_{ij} = \frac{\partial^2 f}{\partial \rho_i \partial \rho_j} \tag{4.28}$$

then f is concave whenever at least one of the eigenvalues of H is negative, or, equivalently, when $\det(H) < 0$. This condition leads to

$$\frac{\partial^2 f}{\partial \rho_A^2}\frac{\partial^2 f}{\partial \rho_B^2} - \left(\frac{\partial^2 f}{\partial \rho_A \partial \rho_B}\right)^2 < 0 \quad \Longleftrightarrow \quad \frac{v_A'(\rho_B)\, v_B'(\rho_A)}{v_A(\rho_B)\, v_B(\rho_A)} > \frac{1}{\rho_A \rho_B}, \tag{4.29}$$

where the right hand side of the "if and only if" implication follows from (4.26). This condition is the same of the one obtained in previous chapter (cf. condition (3.24)). Because of the form of the speed $v_i(\rho_j)$ (4.27), required for the existence of a free energy, condition (4.29) simply becomes

$$\lambda^2 > \frac{1}{\rho_A \rho_B}. \tag{4.30}$$

In Fig. 4.4 we show the differences between the free energy densities for mutual inhibition ($\lambda < 0$) and mutual activation ($\lambda > 0$) interactions. In particular, we note that the main difference is the direction, in the (ρ_A, ρ_B) plane, along which the free energy can have a negative curvature, and hence the direction in which the phase separation occurs. In the case of mutual inhibition (Fig. 4.4-Left), the free energy can have negative curvature in

the direction $\rho_A = \rho_B$. Then, an instability leads the system towards the coexistence of two phases, the first one with low densities ρ_A^ℓ and ρ_B^ℓ, the other with high densities ρ_A^h and ρ_B^h. In the case of mutual activation (Fig. 4.4-Right), the free energy can have negative curvature in the direction $\rho_A + \rho_B = \rho_0$. Then, an instability leads the system towards the coexistence of two phases, the first one with low ρ_A^ℓ and high ρ_B^h, the other with high ρ_A^h and low ρ_B^ℓ. This scenario is exactly the same we found in the linear analysis of the previous chapter (section 3.4) and depicted in Fig. 3.5.

4.2.1.2 Coexisting phases: binodal lines

To conclude our analysis, we compute binodals, or the curves of coexistent phases, in the case of mutual activation. Indeed, because of the form of v that we had to take in order to define a free energy, the coexistence phases in the mutual inhibition case are at $\rho_A^\ell, \rho_B^\ell \sim 0$ and $\rho_A^h, \rho_B^h \to \infty$. Because the system is finite, the high density phase does not occur at infinite densities, but we can observe very strong condensation.

In the case of mutual activation, instead, the free energy is confining in the direction $\rho_A + \rho_B = \rho_0$ and we are then able to apply a 2D version of the common-tangent construction, a standard tool to compute coexisting phases in equilibrium systems. The 2D version consists in constructing a common tangent plane for each value of ρ_A^1 where 1 stands for phase 1.

By imposing 3 conditions we are able to find the densities ρ_A^2, ρ_B^1 and ρ_B^2 as a function of ρ_A^1. The first two conditions correspond to imposing that the gradient of $F \equiv f(\rho_A, \rho_B) - z = 0$ in the two phases is the same:

$$\nabla F^1 = \begin{pmatrix} \partial_{\rho_A} f(\rho_A^1, \rho_B^1) \\ \partial_{\rho_B} f(\rho_A^1, \rho_B^1) \\ -1 \end{pmatrix} = \nabla F^2 = \begin{pmatrix} \partial_{\rho_A} f(\rho_A^2, \rho_B^2) \\ \partial_{\rho_B} f(\rho_A^2, \rho_B^2) \\ -1 \end{pmatrix}. \tag{4.31}$$

Hence,

$$\partial_{\rho_A} f^1 = \partial_{\rho_A} f^2 = \partial_{\rho_A} f \quad \text{and} \quad \partial_{\rho_B} f^1 = \partial_{\rho_B} f^2 = \partial_{\rho_B} f. \tag{4.32}$$

The third condition corresponds to imposing the same plane perpendicular to the gradients in the two phases:

$$\nabla F \cdot \begin{pmatrix} \rho_A^1 - \rho_A^2 \\ \rho_B^1 - \rho_B^2 \\ f(\rho_A^1, \rho_B^1) - f(\rho_A^2, \rho_B^2) \end{pmatrix} = 0. \tag{4.33}$$

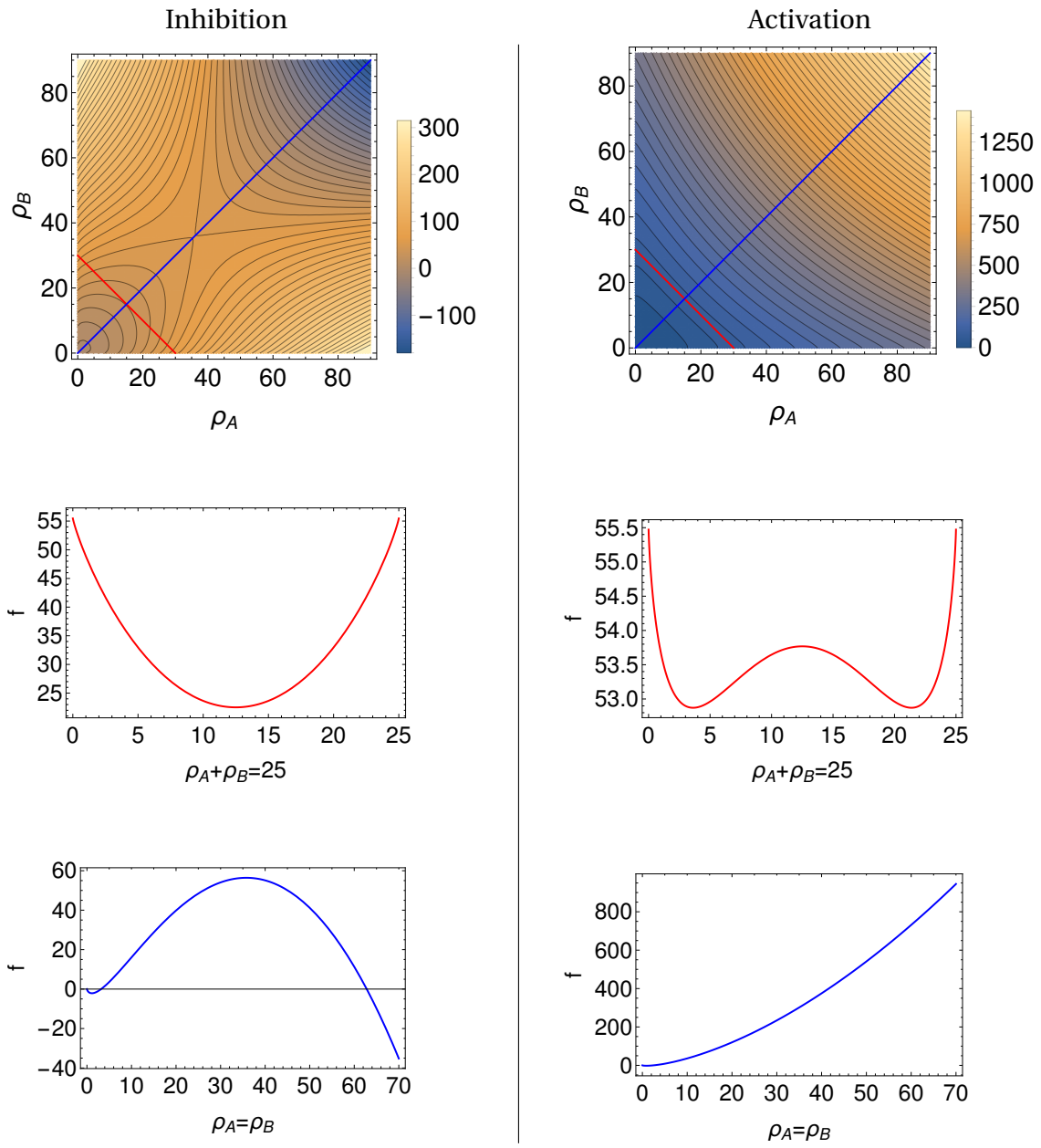

Figure 4.4 – Free energy density $f(\rho_A, \rho_B)$ defined in Eq. 4.26. **Left**: mutual inhibition: $\lambda = -0.1$. Top: contour plot, the colorcode corresponds to the values taken by f. Center: cut of the top image along the red line, corresponding to $\rho_A + \rho_B = 25$. In this direction, the curvature of the inhibition free energy is always positive. Bottom: cut of the top image along the blue line, corresponding to $\rho_A = \rho_B$. In this direction, the curvature of the inhibition free energy changes sign. **Right**: mutual activation: $\lambda = 0.1$. Top: contour plot, the colorcode corresponds to the values taken by f. Center: cut of the top image along the red line, corresponding to $\rho_A + \rho_B = 25$. In this direction, the curvature of the activation free energy changes sign. Bottom: cut of the top image along the blue line, corresponding to $\rho_A = \rho_B$. In this direction, the curvature of the activation free energy is always positive.

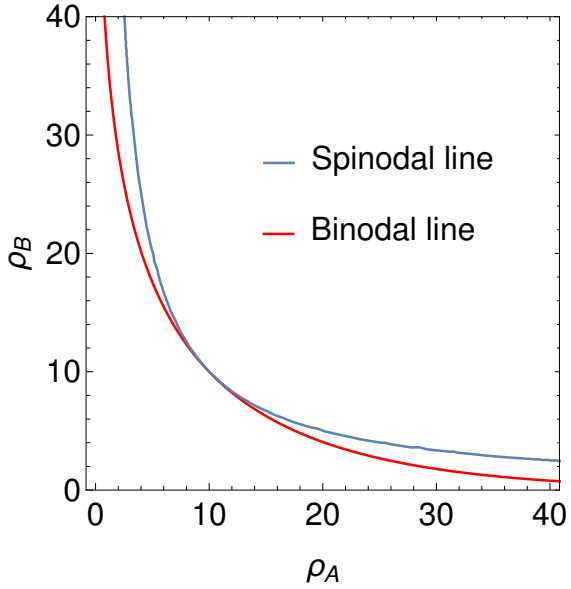

Figure 4.5 – Phase diagram for $\lambda = 0.1$ on the (ρ_A, ρ_B) plane. The spinodal line is given by Eq. 4.30. The binodal is calculated using the procedure detailed in section 4.2.1.2.

Hence,

$$\left(\partial\rho_A f\right)\left(\rho_A^1 - \rho_A^2\right) + \left(\partial\rho_B f\right)\left(\rho_B^1 - \rho_B^2\right) - \left[f(\rho_A^1, \rho_B^1) - f(\rho_A^2, \rho_B^2)\right] = 0. \tag{4.34}$$

Eqs. (4.32) and (4.34) allow to solve the system for ρ_A^2, ρ_B^1, and ρ_B^2 as a function of ρ_A^1. By letting ρ_A^1 vary we can then trace the binodal line, as shown in Fig. 4.5.

4.3 Conclusion

In this last chapter we have studied the fate of MIPS in multispecies systems of quorum sensing-interacting particles. We observed a much richer phenomenology than in monodisperse systems: the system can separate in up to N different phases, whose composition can vary depending on the interaction among different species.

Our mapping to equilibrium allowed us to derive a free energy from which we were able to derive the phase diagram for the case $N = 2$. This mapping indeed provide very powerful tools to predict phase equilibria. Interesting perspectives would then be to generalize the procedure to the $N > 2$ species problem, and to go beyond the local approximation, incorporating higher order gradient terms which are known to quantitatively shift the binodals.

In addition to the rich phenomenology of spatial structures, we observe new exciting phenomena when the interactions cause the system to become frustrated. In that case, oscillating solutions are possible. The natural next step in analysing those solutions

would be to characterize the travelling and standing waves that can emerge, for instance by considering a weakly nonlinear problem.

Finally, a practical consequence of characterizing MIPS mechanisms in multispecies colonies is the fact that we are now able to directly connect microscopic interactions between different species to given macroscopic spatial structures. The mechanism being very simple is an indication of generality, and we thus expect it to be possible to design interacting active particles – living ones, such as cells, or synthetic ones, such as self-propelled colloids – in order to obtain desired emergent macroscopic structures.

Part II

Multilane driven diffusive systems

Chapter 5

From single to multilane driven diffusive systems

Driven diffusive systems encompass a broad class of statistical physics models involving many interacting particles moving stochastically under dynamics that are driven in the bulk and hence, under general boundary conditions, do not respect detailed balance [121, 98]. As such, the stationary states attained in these systems are *non-equilibrium stationary states* (NESS) and exhibit currents both at the macroscopic level (particle currents) and microscopic level (probability currents in configuration space).

One-dimensional realizations have proven particularly informative. The general scenario is a one-dimensional lattice connected to particle reservoirs of fixed density at each end. The macroscopic current that flows through the system is determined by an interplay between the boundary reservoir densities and the bulk dynamics of the particles. As pointed out by Krug [82], this can lead to boundary-induced phase transitions, wherein the macroscopic current can be controlled by the boundary rather than bulk dynamics. Such transitions have no counterpart in equilibrium stationary states, which contain no currents.

The first model of this kind to be studied in detail was the Totally Asymmetric Simple Exclusion Process with open boundaries (TASEP) for which an exact phase diagram was derived [40, 41, 124]. For more general models, however, exact solutions are difficult to come by, therefore to make progress it is important to develop approximations such as mean-field theory [40] and heuristic approaches. For one-dimensional models a particularly useful approach uses an Extremal Current Principle (ECP) [82, 110, 57]. As we discuss in section 5.1, the principle uses the relation $J(\rho)$, between the particle current J and local particle density ρ, along with the boundary conditions, to derive the phase diagram. Its predictions are borne out by exact phase diagrams, for example in the case of the TASEP.

It is noteworthy that the TASEP had first been introduced some years ago as a model for ribosome dynamics in RNA translation [92]. Since then variants of the basic model

have been used as a description of various biophysical transport process, such as molecular motors moving on microtubules [2, 76], fungal hyphae growth dynamics [137], extraction of membrane tubes [140], and it has become a generic starting point to describe transport processes [117, 27]. However, many of these processes require a more complicated geometry than a single one-dimensional lattice. For example, motorway traffic involves several lanes with interchange between lanes and the motion of motor proteins along cytoskeletal filaments often has multiple tracks which may involve different hopping and boundary rates and possibly motors moving in different directions [54, 103]. Pedestrian flows often involve two "multi-lane streets" crossing perpendicularly and a collective dynamics arises in the crossing region [61]. Inspired by these contexts, multilane exclusion processes have been considered by several authors [111, 109, 113, 59, 120, 68, 114, 66, 28, 67, 119, 155, 150] (see for example [46] for an overview) and moreover exclusion processes on more complicated graphs such as trees and networks have been formulated and results obtained [6, 102, 97]. However, for these more complicated geometries exact solutions are few and far between, therefore approximate or heuristic approaches are essential.

In [46] a general class of two-lane models has been considered under the main restrictions that: (i) the transport within a lane is local, i.e. it depends only on the densities within that lane and not on those of neighbouring lanes, and (ii) the average transverse flux of particles from one lane to the other increases with the density of the departing lane and decreases with that of the arriving one. Under these conditions it was shown in [46], through a linear stability analysis of the continuum mean-field equations for the densities, how the phase diagram can be constructed. This construction turns out to be equivalent to an ECP which holds for the total particle current J_{tot}, defined as the sum of the particle currents in each lane.

In this work we generalize this stability analysis to the multilane case which naturally connects one-dimensional lattice gases to their two dimensional counterparts or to more general network topolgies. In addition to the *longitudinal* currents flowing along each lane, new steady *transverse* currents flowing between the lanes can be observed in such systems. Their impact on the phenomenology of multilane system has not been studied so far. By studying the eigenvalue spectrum of the linearized mean-field equations for the densities, we show how an ECP holds for the total longitudinal current. This result implies that a system with an arbitrary number of lanes (such as the motion of molecular motors along the protofilaments of microtubules) may effectively be described by a one-lane system with generally a non-trivial current density relation, validating an assumption that is commonly made (see for example [27] and references therein). A consequence of this effective description is that the transverse current does not enter into the determination of

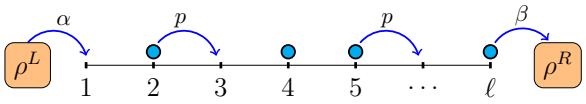

Figure 5.1 – Illustration of the one-dimensional totally asymmetric exclusion process with open boundaries (TASEP).

the phase diagram. Nevertheless, transverse currents can be associated with interesting new phenomena. For instance, one can consider "sheared" systems, in which boundary conditions impose different transverse currents at the two ends of the system. For diffusive bulk dynamics, the transverse current varies continuously, interpolating between its imposed boundary conditions. As we show in chapter 7, for systems driven in the bulk, one may observe a discontinuity in the transverse current corresponding to *shear localization*.

5.1 A brief recap of the TASEP

Before turning to the full multilane problem it is useful to recall the TASEP and its phase diagram. The TASEP consists of a one-dimensional lattice of length ℓ with totally asymmetric hopping dynamics of hard-core particles: at most one particle is allowed at each site and particles can only move in the forward direction with rate p which we may take to be unity (see Fig. 5.1). At the left boundary particles enter with rate α provided the first site is empty and when a particle arrives at the right boundary it leaves with rate β. For $\alpha, \beta \leq 1$ these boundary conditions correspond to a left reservoir with density $\rho^L = \alpha$ and a right reservoir with density $\rho^R = 1 - \beta$.

The phase diagram for the TASEP in the large ℓ limit is illustrated in Fig. 5.2. The different phases that can be observed are:

- a left phase (LP), corresponding to a bulk profile whose density is equal to that of the left reservoir and in which the current is $J = \rho^L(1-\rho^L)$
- a right phase (RP), corresponding to a bulk profile whose density is equal to that of the right reservoir and in which the current is $J = \rho^R(1-\rho^R)$
- a maximal current phase (MC), corresponding to a bulk profile whose density $\rho^M = 1/2$ in which the current is maximized at $J = 1/4$.

Note that historically the Left and Right phases have been referred to as low density (LD) and high density (HD). Here we use a different terminology that is more appropriate to systems that may include further phases.

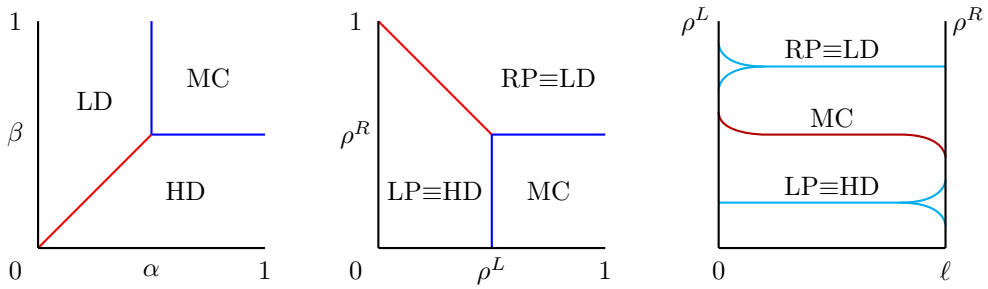

Figure 5.2 – Left: Phase diagram of the TASEP where the control parameters are the injection rate α and ejection rate β and the phases are Low Density (LD), High Density (HD) and Maximal Current (MC). **Center**: phase diagram where the control parameters are the left and right reservoir densities and the phases are Left Phase (LP), Right Phase (RP) and Maximal Current (MC). In both cases the blue lines represent a second order phase transition while the red lines represent a first order phase transition. **Right**: profiles corresponding to left, right and maximal current phases.

To determine the bulk density of single-lane systems, Krug [82] introduced a maximal current principle which was later generalized to an ECP [57] to describe systems in which the advected current $J(\rho)$ has more than one extrema. In practice, this principle states that, given two reservoir densities ρ^L and ρ^R, the dynamics select a constant plateau whose density ρ^B is intermediate between ρ^L and ρ^R, and tends to maximize or minimize the advected current $J(\rho^B)$:

$$J(\rho^B) = \begin{cases} \max_{\rho\in[\rho^R,\rho^L]} J(\rho) & \text{if} \quad \rho^L > \rho^R \\ \min_{\rho\in[\rho^L,\rho^R]} J(\rho) & \text{if} \quad \rho^L < \rho^R \,. \end{cases} \tag{5.1}$$

For the TASEP, the current density relation is $J(\rho) = \rho(1-\rho)$ which is most simply derived from a mean-field consideration that a particle, present with probability ρ, moves forward with rate 1 when there is an empty site ahead (which has probability $1-\rho$). The current-density relation for the TASEP has a single extremum which is a maximum of the current at $\rho = 1/2$. The ECP then allows one to easily derive the phase diagram shown in Fig. 5.2. Note that for more general current density relations, which may exhibit several extrema, the ECP predicts, in addition to the Left, Right and Maximal Current Phases exhibited by the TASEP, a new minimal current phase (mC). This phase corresponds to a bulk profile whose density ρ^m is a local minimum of the current-density relation $J(\rho)$.

Chapter 6

Analytical treatment of multilane systems: MF approximation

6.1 General framework

In this chapter, we consider driven diffusive systems in which particles hop along or between N parallel one-dimensional lattices each of ℓ sites. At both ends, each of these N 'lanes' is in contact with its own particle reservoir which acts as lattice site of fixed mean density denoted by $\rho_i^{L/R}$ for the left/right boundary site of lane i. One simple system falling in this class consists of the N parallel TASEPs shown in Fig. 6.1.

As a starting point of our analysis, we assume that the dynamics of the system is described by a set of N coupled nonlinear mean-field equations for the density $\rho_i(x,t)$ of particles in lane i:

$$\dot{\rho}_i(x,t) = -\partial_x \left[J_i(\rho_i(x,t)) - D_i \partial_x \rho_i(x,t) \right] + \sum_{j \neq i} K_{ji}(\rho_j(x,t), \rho_i(x,t)), \tag{6.1}$$

where $x = n/\ell$ is the position of site n along each lane, $J_i(\rho_i(x))$ and $-D_i\partial_x\rho_i$ are the advective and the diffusive parts of the mean-field current along lane i, and K_{ji} is the net transverse current flowing from lane j to lane i (with $K_{ij} = -K_{ji}$). Throughout our work, we always consider systems which satisfy

$$\partial_{\rho_i} K_{ij}(\rho_i, \rho_j) > 0 \quad \text{and} \quad \partial_{\rho_j} K_{ij}(\rho_i, \rho_j) < 0. \tag{6.2}$$

Physically, this means that the net flux of particles from lane i to lane j increases with ρ_i and decreases with ρ_j.

If the hopping rate of particles along lane i depends on the occupancies of lane $j \neq i$, then J_i depends on ρ_j and not solely on ρ_i. In our work, however, we restrict our attention to the case where the hopping rate along one lane depends only on the occupancies of this

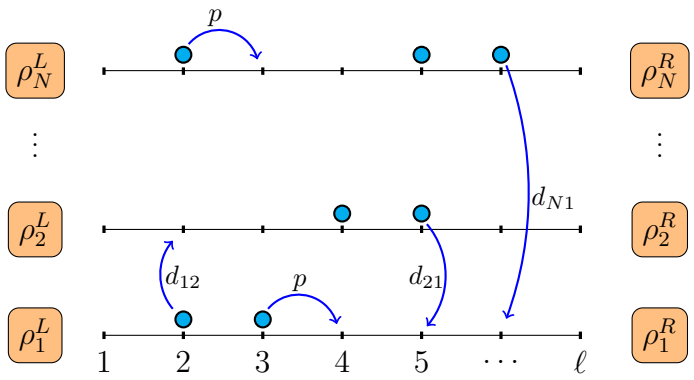

Figure 6.1 – Schematic representation of N parallel TASEPs which are connected at both ends to particle reservoirs of fixed densities. Particles hop along each lane, to the right, at rate p and can hop from lane i to lane $i \pm 1$ at rate $d_{i,i\pm1}$, giving rise to non-zero longitudinal and transverse currents.

lane, so that the mean-field longitudinal current depends only on the density of this lane: $J_i(\rho_i)$. The constraints we consider here thus preclude attractive interactions between particles on *different* lanes, while still allowing for generic interactions along each lane.

The derivation of Eq. (6.1) from the microscopic dynamics models follows a standard mean-field approximation comprising factorization of all density correlation functions which we review in next chapter, section 7.2. For illustrative purposes we consider the example presented in Fig. 6.1 of coupled totally asymmetric exclusion processes: particles hop forward longitudinally along lane i from site n to the next site $n+1$ if that site is vacant with rate p; particles can hop transversely to a vacant site at position n in a neighbouring lane $i \pm 1$ with rate $d_{i,i\pm1}$. Then $J_i(\rho_i) = p\rho_i(1-\rho_i)/\ell$, $D_i = p/(2\ell^2)$ and $K_{i\pm1,i} = d_{i\pm1,i}\rho_{i\pm1}(1-\rho_i) - d_{i,i\pm1}\rho_i(1-\rho_{i\pm1})$. The explicit form of J_i, D_i and K_{ij} for other models is given in next chapter, section 7.2.

Given reservoir densities we want to compute the average density profiles along each lane, i.e. the steady-state solutions of Eq. (6.1) satisfying $\rho_i(0) = \rho_i^L$ and $\rho_i(1) = \rho_i^R$. Solving this set of N coupled nonlinear equations is, however, very hard even in the steady state. Therefore we first consider the possible homogeneous solutions to Eq. (6.1) which are valid in the bulk, i.e. far from the boundaries. We refer to these solutions as *equilibrated plateaux*, since their densities are balanced by the exchange of particles between lanes.

As we shall see, these solutions, which we properly define in section 6.1.1, play a major role in constructing the form of the steady-state profiles and the phase diagrams. We show in section 6.1.3 how stationary profiles are typically made of equilibrated plateaux connected at their ends either to other plateaux (forming shocks) or directly to the reservoirs (see Fig. 6.3). For this to hold, the equilibrated plateaux have to be dynamically stable which we show in section 6.1.2 to be true for systems satisfying conditions (6.2).

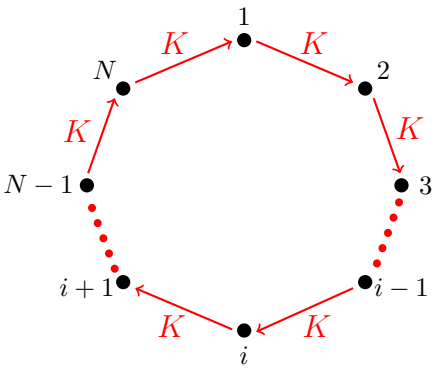

Figure 6.2 – In a system with N parallel lanes, organized on a ring, equilibrated plateaux can be realized with a steady loop of non-zero transverse current $K > 0$.

6.1.1 Plateau solutions

The plateaux solutions – homogeneous, steady-state solutions denoted $\rho_i(x) = \rho_i^{\mathrm{p}}$ – are found by setting time and space derivatives to zero in (6.1). The mean-field steady-state equations then reduce to

$$\forall i \qquad \sum_{j \neq i} K_{ji}(\rho_j^{\mathrm{p}}, \rho_i^{\mathrm{p}}) = 0. \tag{6.3}$$

Eq. (6.3) simply states that, for each site of lane i, the mean transverse flux of particles coming from all other lanes $j \neq i$ is equal to the mean transverse flux leaving lane i[1].

If there are only two lanes, the steady-state condition (6.3) implies

$$K_{12} = K_{21} = 0, \tag{6.4}$$

so that there is no net transverse current. However, for a number of lanes $N \geq 3$ the condition (6.3) can be satisfied by the presence of a non-zero steady loop of transverse current. For example, for $N = 3$, with $K_{12} = K_{23} = K_{31} = K \neq 0$, a non-zero steady transverse current is present (see Fig. 6.2 for an illustration with N lanes on a ring).

6.1.2 Dynamical stability of equilibrated plateaux

The plateaux solutions are only relevant to the steady state if they are dynamically stable. In B.1 we show, through a dynamical linear stability analysis, that a small perturbation

[1] Note that if one forgets the spatial structure of each lane and focuses on the exchange dynamics between lanes, the system amounts to a Markov process with N states which has, up to an overall normalization, a unique steady state unless it is reducible.

$\delta\rho_i(x,t)$ around the equilibrated plateau solution:

$$\rho_i(x,t) = \rho_i^{\mathrm{p}} + \sum_q \delta\rho_i^q(t)\exp\big(iqx\big), \tag{6.5}$$

where $q = 2\pi n$ with $n = 1,\dots,\ell-1$, vanishes exponentially rapidly in time if one considers systems in which

$$K_{ij}^i \equiv \partial_{\rho_i} K_{ij}(\rho_i^{\mathrm{p}},\rho_j^{\mathrm{p}}) > 0 \quad \text{and} \quad K_{ij}^j \equiv \partial_{\rho_j} K_{ij}(\rho_i^{\mathrm{p}},\rho_j^{\mathrm{p}}) < 0. \tag{6.6}$$

Note that this is slightly weaker than condition (6.2) since (6.6) only has to hold for equilibrated plateaux densities.

6.1.3 Equilibrated and unequilibrated reservoirs

In analogy with equilibrated plateaux, one can define *equilibrated reservoirs*, whose densities satisfy

$$\forall i \qquad \sum_{j\neq i} K_{ji}(\rho_j^{R,L},\rho_i^{R,L}) = 0, \tag{6.7}$$

where ρ_i^L and ρ_i^R correspond to the densities of the reservoirs at the left and right ends of lane i, respectively. If equilibrated reservoirs are imposed at both ends of the system, with $\rho_i^R = \rho_i^L$, a simple solution of the mean-field equations in steady state is found by connecting the reservoirs through constant plateaux. Even though these boundary conditions are exceptional, equilibrated plateau solutions play an important role in the steady state of driven diffusive systems. As we show, far from the boundaries, in a large system, the density profile is typically constant. With this in mind, in the following, we use the term "plateaux" to describe not only completely constant profiles, where the density is the same on all sites of the system, but also flat *portions* of density profiles, see Fig. 6.3, which can be connected to reservoirs or other density plateaux by small non-constant boundary layers.

As noted previously, when equilibrated reservoirs are imposed at the two ends of the system with the *same* densities $\rho_i^L = \rho_i^R$, one observes dynamically stable plateaux with $\rho_i(x) = \rho_i^L$. Two other more general classes of boundary condition are relevant.

First, left and right equilibrated reservoirs can imply different sets of plateaux densities in the bulk; how the density is then selected in the bulk is one of the central questions tackled in our work. In Fig. 6.4, we show examples of Left and Right phases, where the bulk density is controlled respectively by left and right reservoirs. In a left (resp. right) phase, a small modification of the right (resp. left) reservoir densities leaves the bulk part

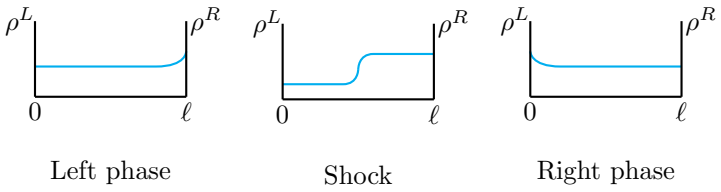

Figure 6.3 – Example of Left, Right and Shock phases

of the density profile unaffected; only the boundary layers connecting to the right (resp. left) reservoir change.

Second, the reservoirs can be unequilibrated, that is their densities do not obey (6.7). In this case both left and right reservoir densities are connected to bulk equilibrated plateaux by small boundary layers. In Fig. 6.5, we show examples of the corresponding left and right phases. Again, in a left (resp. right) phase, a small modification of the right (resp. left) reservoir densities leaves the bulk part of the density profile unaffected; only the boundary layers connecting to the right (resp. left) reservoir change.

Here we focus on how the densities of the equilibrated plateaux in the bulk are selected by the boundary conditions imposed by equilibrated reservoirs and only comment on unequilibrated reservoirs in the conclusion section 7.3 of next chapter. The boundary layers connecting reservoir to plateaux – or plateaux to other plateaux when a shock is observed, as in Fig. 6.3 – are beyond the scope of our work, but can be studied using asymptotic methods [99, 155, 55].

6.2 Linear stability analysis

The mean-field dynamics (6.1) evolves the density profiles towards flat plateaux which are connected at their ends either to other plateaux or to reservoirs. The acceptable plateaux solutions can thus be worked out by considering which types of stationary profiles can connect a bulk plateau to other densities at its right and left ends. For instance, in the bottom panels of Fig. 6.5, the steady-state solution of the mean-field equations is made up of a plateau connected on its left end to equilibrated reservoirs and on its right end to unequilibrated reservoirs. In practice, we only study whether such profiles can exist by looking at the vicinity of the equilibrated plateau. Namely, rather than solving the full non-linear problem, we carry out a linear analysis of the steady-state mean-field equations

$$0 = \partial_x \left[D_i \partial_x \rho_i(x,t) - J_i(\rho_i(x,t)) \right] + \sum_{j \neq i} K_{ji}(\rho_j(x,t), \rho_i(x,t)), \tag{6.8}$$

around equilibrated plateaux.

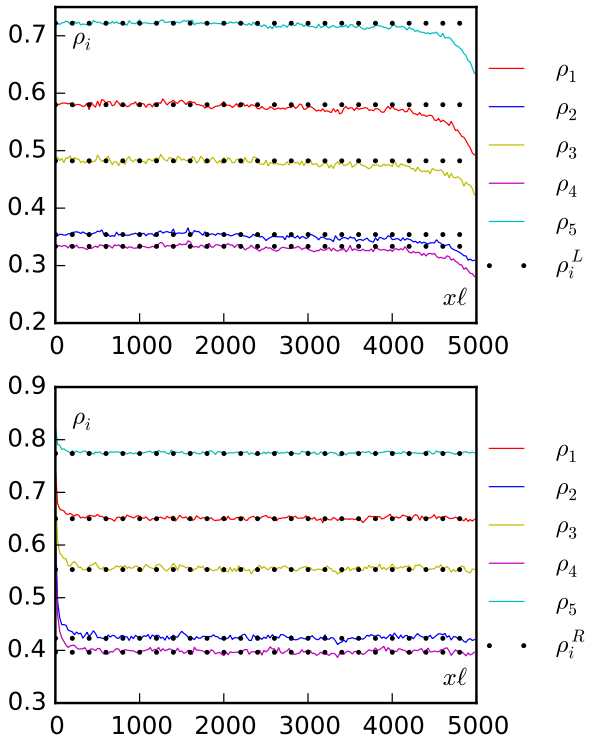

i	ρ_i^L	ρ_i^R
1	0.58	0.45
2	0.35	0.25
3	0.48	0.36
4	0.33	0.24
5	0.72	0.61

i	ρ_i^L	ρ_i^R
1	0.85	0.65
2	0.69	0.42
3	0.79	0.55
4	0.65	0.40
5	0.90	0.77

Figure 6.4 – Connections of equilibrated plateaux to equilibrated reservoirs, for five parallel TASEPs as in Fig. 6.1. Top and bottom figures correspond to Left and Right phases. **Top:** The density in the bulk is controlled by the left reservoirs; a small change of the right reservoir densities leaves the bulk plateau unchanged. **Bottom:** The density in the bulk is controlled by the right reservoirs; a small change of the left reservoir densities leaves the bulk plateau unchanged. For both cases, $p = 1$, $d_{12} = 10^{-3}$, $d_{23} = 9.10^{-3}$, $d_{34} = 2.10^{-3}$, $d_{45} = 8.10^{-3}$, $d_{51} = 3.10^{-3}$, $d_{15} = 7.10^{-3}$, $d_{21} = 4.10^{-3}$, $d_{32} = 6.10^{-3}$, $d_{43} = 5.10^{-3}$, $d_{54} = 2.10^{-3}$ and results are obtained using continuous time Monte Carlo simulations.

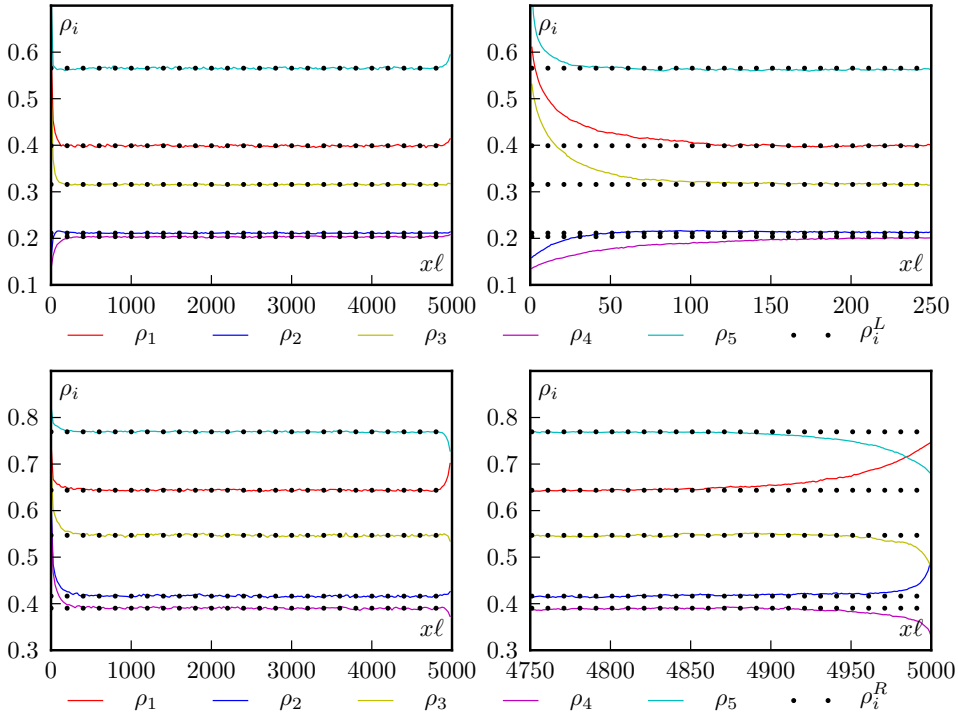

i	ρ_i^L	ρ_i^R
1	0.68	0.45
2	0.15	0.25
3	0.58	0.36
4	0.13	0.24
5	0.92	0.61

i	ρ_i^L	ρ_i^R
1	0.85	0.75
2	0.69	0.52
3	0.79	0.45
4	0.65	0.30
5	0.90	0.67

Figure 6.5 – Connections of equilibrated plateaux to equilibrated and unequilibrated reservoirs, for five parallel TASEPs as in Fig. 6.1. **Top-Left:** A bulk plateau is connected to an equilibrated reservoir on the right and an unequilibrated one on the left. This is a left phase and the the bulk density is insensitive to small modification of the density of the right reservoirs. There are thus two boundary layers: one connecting the bulk plateau to the left unequilibrated reservoir, which controls the bulk density, and one connecting the bulk plateau to the right reservoir. **Top-Right:** Close-up on the unequilibrated left reservoir. **Bottom:** The same with left equilibrated reservoirs and right unequilibrated reservoirs, in a Right phase. For both cases, $p = 1$, $d_{12} = 10^{-3}$, $d_{23} = 9.10^{-3}$, $d_{34} = 2.10^{-3}$, $d_{45} = 8.10^{-3}$, $d_{51} = 3.10^{-3}$, $d_{15} = 7.10^{-3}$, $d_{21} = 4.10^{-3}$, $d_{32} = 6.10^{-3}$, $d_{43} = 5.10^{-3}$, $d_{54} = 2.10^{-3}$ and results were obtained using continuous time Monte Carlo simulations.

We thus look for steady-state profiles of the form

$$|\rho(x)) = |\rho^{\mathrm{p}}) + |\delta\rho(x)), \qquad \text{where} \qquad |\rho(x)) \equiv \begin{pmatrix} \rho_1(x) \\ \vdots \\ \rho_N(x) \end{pmatrix} \tag{6.9}$$

is a compact notation for N-dimensional vectors with components $\rho_i(x)$ and $|\rho^{\mathrm{p}})$ corresponds to a set of equilibrated plateau densities. Since we have already established the *dynamical* stability of equilibrated plateaux in section 6.1.2 (and B.1), we are now only concerned with the existence of *spatial* stationary perturbations $|\delta\rho(x))$ around them. In the following, we simply refer to $|\delta\rho(x))$ as "perturbations", omitting their implicit stationarity.

Linearizing the steady-state mean-field equations (6.8) close to $|\rho^{\mathrm{p}})$ then yields

$$0 = D_i\partial_{xx}\delta\rho_i(x) - J_i^i(\rho_i^{\mathrm{p}})\partial_x\delta\rho_i(x) + \sum_{j\neq i}\left[K_{ji}^i\delta\rho_i(x) + K_{ji}^j\delta\rho_j(x)\right], \tag{6.10}$$

where $J_i^i = \frac{\partial J_i(\rho_i)}{\partial\rho_i}$ and K_{ji}^i, K_{ij}^j are defined in (6.6). Equation (6.10) can be seen as a first order ordinary differential equation $\partial_x|v\rangle = M|v\rangle$, where

$$M(\rho_1^{\mathrm{p}},\ldots,\rho_N^{\mathrm{p}}) = \left(\begin{array}{ccc|c} \frac{J_1^1}{D_1} & & & \\ & \ddots & & -M^K \\ & & \frac{J_N^N}{D_N} & \\ \hline \frac{1}{D}1 & & & \\ & \ddots & & 0 \\ & & \frac{1}{D}N & \end{array}\right), \quad |v\rangle = \begin{pmatrix} D_1\delta\rho_1'(x) \\ \vdots \\ D_N\delta\rho_N'(x) \\ \delta\rho_1(x) \\ \vdots \\ \delta\rho_N(x) \end{pmatrix} \tag{6.11}$$

Here, M^K is an $N\times N$ matrix defined as

$$M_{ii}^K = \sum_{j\neq i} K_{ji}^i \qquad M_{ij}^K = K_{ji}^j, \tag{6.12}$$

and $|v\rangle$ is a compact notation for $2N$-dimensional vectors and $\delta\rho_i'(x) \equiv \partial_x\delta\rho_i(x)$. When M is diagonalizable, solutions of this ordinary differential equation are of the form

$$|v(x)\rangle = \sum_{k=0}^{2N-1} \alpha_k e^{\lambda_k x}|v^k\rangle \tag{6.13}$$

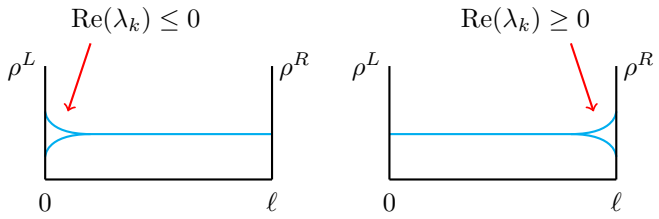

Figure 6.6 – Connecting a reservoir to an equilibrated plateau. With $\mathrm{Re}(\lambda_k) \leq 0$, one can construct perturbations connecting an equilibrated plateau to the left reservoirs. With $\mathrm{Re}(\lambda_k) \geq 0$, one can construct perturbations connecting an equilibrated plateau to right reservoirs.

where $|v^k\rangle = \left(D_1\lambda_k\delta\rho_1^k,\ldots,D_N\lambda_k\delta\rho_N^k,\delta\rho_1^k,\ldots,\delta\rho_N^k\right)$ are the $2N$ eigenvectors of the matrix M and λ_k the corresponding eigenvalues. This implies that the perturbation to the density profile (6.9) may be decomposed as

$$|\delta\rho(x)) = \sum_{k=0}^{2N-1} \alpha_k e^{\lambda_k x}|\delta\rho^k). \tag{6.14}$$

The study of the spectrum of the matrix $M(\rho_1^{\mathrm{p}},\ldots,\rho_N^{\mathrm{p}})$ reveals whether given boundary conditions can be connected to a set of bulk plateaux of densities $|\rho^{\mathrm{p}})$ through appropriate perturbations $|\delta\rho(x))$ (6.14). This allows us to construct the phase diagram, as we show in next chapter, section 7.1.

We now detail how the spectrum of M is organized and the role played by its eigenvectors. One might expect the study of the spectrum of a $2N$ dimensional matrix to be rather complex. But, as we show below, a simple result for the phase diagram, which is solely determined by the *number* of eigenvalues with positive (or negative) real part, can be obtained. This can be found using a simple criterion which does not require knowledge of the full spectrum.

Specifically, we show in section 6.2.1 that there is always one zero eigenvalue, λ_0, whose eigenvector corresponds to a (unique) uniform perturbation which preserves the equilibrated plateau condition. Then, in section 6.2.2, we show that the rest of the spectrum can be organized in two different ways: either with $N-1$ eigenvectors with $\mathrm{Re}(\lambda_k) < 0$ and N with $\mathrm{Re}(\lambda_k) > 0$, or with N eigenvectors with $\mathrm{Re}(\lambda_k) < 0$ and $N-1$ with $\mathrm{Re}(\lambda_k) > 0$. We show that the first case is compatible with a Left Phase and the second with a Right Phase (see Fig. 6.6). The separation between these two cases is thus controlled by the change of sign of the real part of an eigenvalue, which we show in section 6.2.3 to occur at extrema of the total current J_{tot} within the space of equilibrated plateaux.

Sections 6.2.1 to 6.2.3 thus establish the possibility, at the linear level, of a nonuniform profile $|\rho(x))$ connecting a plateau $|\rho^{\mathrm{p}})$ to other equilibrated density vectors at one of

its ends. In next chapter, then, by studying the dynamics of the shocks connecting the plateaux, we derive a simple recipe for constructing the phase diagram.

6.2.1 Uniform shift of equilibrated plateaux

We now show that the matrix M given in (6.11) always admits a unique $\lambda_0 = 0$ eigenvalue, associated to uniform shifts of the densities of equilibrated plateaux. Using $M|v^0\rangle = 0$ implies that $|v^0\rangle = (0,\dots,0,\delta\rho_1^0,\dots,\delta\rho_N^0)$ with

$$M^K|\delta\rho^0) = 0. \tag{6.15}$$

One easily checks that M^K is a Markov (or Intensity) matrix by summing its row elements: $\forall\, j,\ \sum_i M^K_{ij} = 0$. By the Perron-Frobenius theorem, M has a unique $\lambda = 0$ eigenvector $|\delta\rho^0)$ which is real and has all its non-zero components of the same sign (which we take to be positive).

It is easy to check that a perturbation of the density vector from $|\rho^{\rm p})$ to $|\rho^{\rm p}) + \epsilon|\delta\rho^0)$ for small ϵ indeed results in an equilibrated plateau, since to first order in ϵ

$$\begin{aligned}\sum_{j\neq i} K_{ji}(\rho_j^{\rm p}+\epsilon\delta\rho_j^0,\rho_i^{\rm p}+\epsilon\delta\rho_i^0) &= \sum_{j\neq i} K_{ji}(\rho_j^{\rm p},\rho_i^{\rm p}) + \epsilon\sum_{j\neq i} K^i_{ji}\delta\rho_i^0 + \epsilon\sum_{j\neq i} K^j_{ji}\delta\rho_j^0 \\ &= 0+\epsilon\sum_j M^K_{ij}\delta\rho_j^0 \\ &= 0\,,\end{aligned} \tag{6.16}$$

where we used the fact that $\sum_{j\neq i} K_{ji}(\rho_j^{\rm p},\rho_i^{\rm p}) = 0$ since $|\rho^{\rm p})$ is equilibrated.

The vector $|\delta\rho^0)$ is therefore the unique tangent vector to the one-dimensional manifold of equilibrated plateaux: all infinitesimal perturbations $|\delta\rho^{\rm p})$ such that $|\rho^{\rm p}) + |\delta\rho^{\rm p})$ remains equilibrated are thus parallel to $|\delta\rho^0)$. It is important to bear in mind that since M is a function of $|\rho^{\rm p})$, $|\delta\rho^0)$ also depends on $|\rho^{\rm p})$.

6.2.2 Connecting equilibrated plateaux to reservoirs

In this section we consider how a bulk plateau density vector $|\rho^{\rm p})$ may be connected by a density profile to equilibrated reservoirs $|\rho^{\rm r})$. For the sake of clarity, we focus here on the main results whose detailed derivations are given in Appendix B.2.

First, as noted above, we show in B.2.1 that in addition to the $\lambda = 0$ eigenvalue discussed in the previous section, the spectrum of M is composed of either

(i) N eigenvalues with positive real parts and $N-1$ eigenvalues with negative real parts,

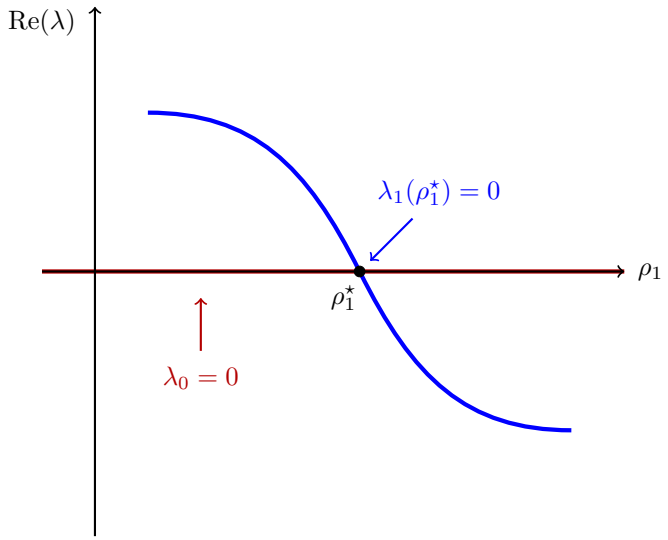

Figure 6.7 – Change of sign of an eigenvalue of stability matrix M given by (6.11). The eigenvalue λ_1 vanishes at $\rho_1 = \rho_1^\star$ while $\lambda_0 = 0$ everywhere.

(ii) $N-1$ eigenvalues with positive real parts and N eigenvalues with negative real parts.

We then show in B.2.2 that in case (i) the plateau density vector can only be connected to arbitrary equilibrated reservoir densities to the right. Thus, for equilibrated reservoirs, such plateaux can only be observed in a Left Phase – a phase in which the bulk plateaux are controlled by the left reservoirs – with $|\rho^{\mathrm{p}}) = |\rho^{L})$. Conversely, in case (ii) the plateau density vector can only be connected to arbitrary equilibrated reservoir densities to the left. Such plateaux can thus only be observed in a Right Phase.

As the density vector $|\rho^{\mathrm{p}})$ varies, the transition between the two cases corresponds to the vanishing of an eigenvalue, whose real part then changes sign. Precisely at the transition one then has $N-1$ eigenvalues with $\mathrm{Re}(\lambda_k) > 0$, $N-1$ eigenvalues with $\mathrm{Re}(\lambda_k) < 0$ and two zero eigenvalues. Since the eigenspace associated with $\lambda = 0$ is of dimension 2 but there is only one $\lambda = 0$ eigenvector, the matrix M is then non-diagonalizable. Let us now show that this corresponds to the local extrema of J_{tot} within the space of equilibrated plateaux.

6.2.3 Change of sign of Re(λ) and extrema of the current

From the discussion above it is clear that for the phase diagram to be richer than simply one Left Phase or one Right Phase, we need an eigenvalue – let us denote it λ_1 – to vanish and change sign as the reservoir densities are varied.

For equilibrated plateaux $|\rho)$ (to lighten the notation we drop the p superscript), all densities ρ_i and all eigenvalues of $M(\rho_1, \ldots, \rho_N)$ can be written as functions of the density

of the first lane ρ_1 via the equilibrated plateau condition (6.3). For some value $\rho_1^\star$, we thus require $\lambda_1(\rho_1^\star) = 0$ with $\lambda_1(\rho_1^\star \pm \varepsilon) \neq 0$ (see Fig. 6.7). As we show below, this happens at all the local extrema of the total current

$$J_{\text{tot}}(\rho_1) \equiv \sum_i J_i[\rho_i(\rho_1)] \tag{6.17}$$

within the set of equilibrated plateaux.

At a given plateau $|\rho)$, the tangent vector to the set of equilibrated plateaux is the $\lambda = 0$ eigenvector $|\delta\rho^0)$ of matrix $M^K(\rho_1,\ldots,\rho_N)$, defined in (6.12). The extrema of J_{tot} within the set of equilibrated plateaux thus occur when

$$\mathrm{d}J_{\text{tot}} = \nabla J_{\text{tot}} \cdot |\delta\rho^0) = \sum_i J_i^i \delta\rho_i^0 = 0. \tag{6.18}$$

The linearized steady-state mean-field Eq. (6.10) becomes, when we take $\delta\rho_i = \delta\rho_i^1 \mathrm{e}^{\lambda_1 x}$, an eigenvector equation for $|\delta\rho^1)$ which reads

$$(\lambda_1)^2 D_i \delta\rho_i^1 - \lambda_1 J_i^i \delta\rho_i^1 + \sum_{j\neq i}\left[K_{ji}^i \delta\rho_i^1 + K_{ji}^j \delta\rho_j^1\right] = 0. \tag{6.19}$$

By summing (6.19) over i, one finds $(\lambda_1)^2 \sum_i D_i \delta\rho_i^1 - \lambda_1 \sum_i J_i^i \delta\rho_i^1 = 0$ and thus

$$\sum_i J_i^i \delta\rho_i^1 = \lambda_1 \sum_i D_i \delta\rho_i^1. \tag{6.20}$$

As we approach $\rho_1^\star$, where $\lambda_1 \to 0$, the left hand side of (6.20) must tend to zero.

However, since M^K is a Markov matrix, there is a unique eigenvector corresponding to the zero eigenvalue, which is $|\delta\rho^0)$. Therefore as $\lambda_1 \to 0$, we must have $\delta\rho_i^1 \to \delta\rho_i^0$. Thus as $\rho_1 \to \rho_1^\star$ we conclude that

$$\sum_i J_i^i \delta\rho_i^1 \to \sum_i J_i^i \delta\rho_i^0 = \mathrm{d}J_{\text{tot}} \to 0. \tag{6.21}$$

As $\rho_1 \to \rho_1^\star$ this corresponds to the extremal current condition, Eq. (6.18). The vanishing of $\mathrm{Re}(\lambda_1)$ thus occurs at the extrema of J_{tot}.

Finally, since $|\delta\rho^0)$ is the unique zero eigenvector of a Markov matrix M^K, all its components are of the same sign. As D_i are all positive, equations (6.20) and (6.21) imply that $\mathrm{Re}(\lambda_1(\rho_1))$ and $J'_{\text{tot}}(\rho_1)$ are of the same sign in the vicinity of the extrema of J_{tot}. Since neither of them vanish and change sign elsewhere, $\mathrm{Re}(\lambda(\rho_1))$ and $J'_{\text{tot}}(\rho_1)$ must always have the same sign.

Chapter 7

Results: phase diagram and shear localization

In this chapter, we first present the recipe for the construction of the phase diagram, based on the linear analysis just performed, and we show that it is equivalent to a generalized extremal current principle for the total current $J_{\text{tot}}(\rho_1)$. We then show how to construct the dynamics for the multilane system – that we *assumed* in the previous chapter – starting from microscopic models and we study some interesting cases.

7.1 Phase diagram and extrema of the currents

From sections 6.2.2 (B.2) and 6.2.3, one concludes that for equilibrated plateaux density vectors $|\rho)$, the sign of $J'_{\text{tot}}(\rho_1)$ controls the boundary reservoirs to which the plateaux can be connected:

- For $J'_{\text{tot}}(\rho_1) > 0$, the plateaux can only be connected to different equilibrated densities at their right ends

- For $J'_{\text{tot}}(\rho_1) < 0$, the plateaux can only be connected to different equilibrated densities at their left ends.

- $J'_{\text{tot}}(\rho_1) = 0$ is a singular limiting case between these two regimes;

    - For a local maximum of J_{tot}, perturbations with $\delta\rho_1 > 0$ are in a region where $J'_{\text{tot}}(\rho_1) < 0$ and can thus connect to equilibrated densities with $\tilde{\rho}_1 > \rho_1$ on the left. Perturbations with $\delta\rho_1 < 0$ are in a region where $J'_{\text{tot}}(\rho_1) > 0$ and can thus connect to equilibrated densities with $\tilde{\rho}_1 < \rho_1$ on the right.
    - For a local minimum of J_{tot}, perturbations with $\delta\rho_1 > 0$ are in a region where $J'_{\text{tot}}(\rho_1) > 0$ and can thus connect to equilibrated densities with $\tilde{\rho}_1 > \rho_1$ on the

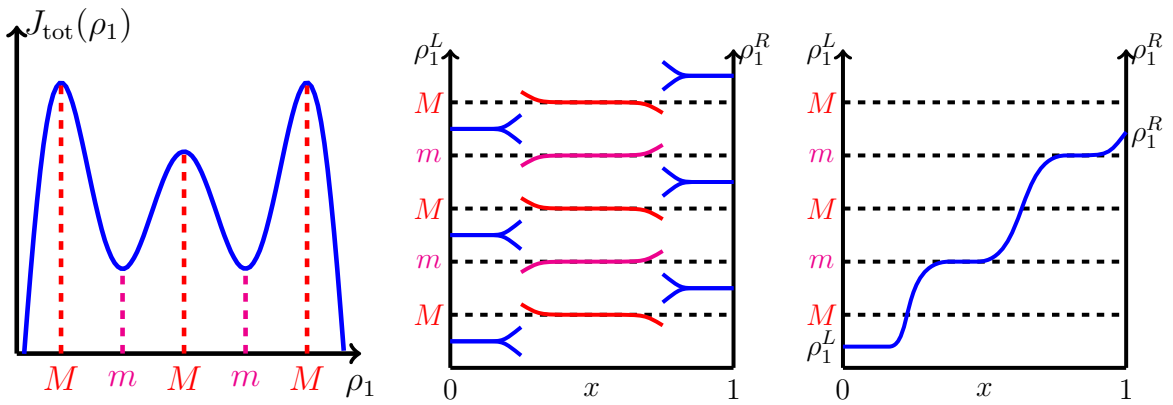

Figure 7.1 – Left: Example of current density relation $J_{\rm tot}(\rho_1)$. **Center**: Linear stability of all equilibrated plateau. **Right**: Example of possible profiles connecting left and right reservoirs. The shocks connecting the plateaux need not be stationary.

right. Perturbations with $\delta\rho_1 < 0$ are in a region where $J'_{\rm tot}(\rho_1) < 0$ and can thus connect to equilibrated densities with $\tilde{\rho}_1 < \rho_1$ on the left.

The exact shape of the profile in this case, which may involve algebraic functions rather than exponential, is beyond the scope of our work.

To construct the phase diagram, one thus computes $J_{\rm tot}(\rho_1)$ and finds the values of all its extrema, as shown in the left panel of Fig. 7.1. This allows one to determine for each plateau if, and how, it can be connected to other equilibrated densities at its left or right ends, as shown in the central panel of Fig. 7.1. Then, for given sets of equilibrated reservoirs $|\rho^L)$ and $|\rho^R)$, one can construct the profiles which are in agreement with the linear analysis. As shown in the right panel of Fig. 7.1, these profiles are monotonic and made of successions of plateaux, whose densities are set by the reservoirs or correspond to local extrema of the current, connected by shocks.

While such shocks are in agreement with the linear analysis of the steady-state mean-field equations, they need not be stationary. Let us consider the situation depicted in Fig. 7.2. The rate of change of the number of particles in the region $[x_1, x_2]$ due to the moving shock profile is

$$\dot{\mathcal{N}}_{[x_1,x_2]} = v \sum_i \left(\rho_i^1 - \rho_i^2\right), \tag{7.1}$$

where v is the shock velocity and the sum is over lanes. By the continuity equation for the number of particles the rate of change is also given by the fluxes at the boundary of the region, thus

$$\dot{\mathcal{N}}_{[x_1,x_2]} = \int_{x_1}^{x_2} \sum_i \dot{\rho}_i = \sum_i \left[J_i(\rho_i^1) - J_i(\rho_i^2)\right] \tag{7.2}$$

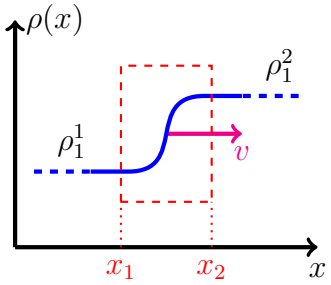

Figure 7.2 – Schematic of a shock profile connecting a plateau of density ρ_1^1 to a plateau of density ρ_1^2 moving with speed v. The number of particles within the red rectangle varies at a rate $v(\rho_{\text{tot}}^1 - \rho_{\text{tot}}^2)$. If $v > 0$ the plateau at $\rho_1 = \rho_1^1$ spreads while the plateau at $\rho_1 = \rho_1^2$ recedes. Conversely, for $v < 0$, the plateau at $\rho_1 = \rho_1^2$ spreads while the one at $\rho_1 = \rho_1^1$ recedes.

Equating the two expressions, the velocity v of the shock is thus given by

$$v = \frac{J_{\text{tot}}(\rho_1^1) - J_{\text{tot}}(\rho_1^2)}{\rho_{\text{tot}}^1 - \rho_{\text{tot}}^2} \tag{7.3}$$

where $\rho_{\text{tot}} = \sum_i \rho_i$.

Let us now show that the sign of $\rho_{\text{tot}}^1 - \rho_{\text{tot}}^2$ is the same as the sign of $\rho_1^1 - \rho_1^2$. Since the tangent vector to the set of equilibrated plateau, $|\delta\rho^0)$, has all its components of the same sign, a small increase in ρ_1 results in a new equilibrated plateau with small increases of $\rho_{i\neq 1}$. The total density ρ_{tot} is thus an increasing function of ρ_1: if one has $\rho_1^1 < \rho_1^2$ (resp. $\rho_1^1 > \rho_1^2$) then one must have $\rho_{\text{tot}}^1 < \rho_{\text{tot}}^2$ (resp. $\rho_{\text{tot}}^1 > \rho_{\text{tot}}^2$). Increasing and decreasing shocks thus correspond to $\rho_1^2 > \rho_1^1$ and $\rho_1^2 < \rho_1^1$.

Increasing shocks thus move to the right if $J_{\text{tot}}(\rho_1) < J_{\text{tot}}(\rho_2)$ and the plateau of density ρ_1 invades the plateau of density ρ_2. Conversely if $J_{\text{tot}}(\rho_1) > J_{\text{tot}}(\rho_2)$, the shock moves to the left and the plateau of density ρ_2 widens. For decreasing shocks, on the the other hand, the plateau corresponding to the larger current widens.

Note that the shocks on all lanes are co-localized, as shown by our linear stability analysis. Intuitively, unequilibrated densities would otherwise have to coexist between, say, the shock on lane 1 and on lane 2, which would make the profiles unstable [119].

7.1.1 Construction of the phase diagram

We can now gather everything together in a simple rule for constructing the phase diagram:

- For increasing profiles, when $\rho_1^L < \rho_1^R$, among all the plateaux in agreement with the linear analysis, the one corresponding to the smallest current spreads while the

others recedes. The possible plateaux correspond either to the reservoir densities, if $J'_{\text{tot}}(\rho_1)^L > 0$ or $J'_{\text{tot}}(\rho_1)^R < 0$, or to local minima of the currents (local maxima correspond to decreasing profiles as shown in Fig. 7.1). For continuous $J_{\text{tot}}(\rho_1)$, the global extrema of J_{tot} on $[\rho^L, \rho^R]$ are either at the boundaries or at local extrema so that the minima of J_{tot} among the possible plateaux correspond to the global minima of J_{tot} on $[\rho_1^L, \rho_1^R]$. Note that if there are several minima with the same value of the current, a shock connecting these densities does not propagate ballistically but simply diffuses.

- For decreasing profiles, when $\rho_1^L > \rho_1^R$, the converse reasoning leads to the selection of the plateau(x) with the largest current.
  This is summarized in the generalized ECP discussed in next section.

7.1.2 A generalized extremal current principle

Let us now show how our approach relates to the extremal current principle. As noted in section 5.1, based on the assumption that there exists a relation $J(\rho)$ between the particle current J and local density ρ, an extremal current principle can be used to derive the phase diagram of the TASEP [82]. In [46], this principle was generalized to two-lane systems with equilibrated reservoirs by extremising the *total* current summed over the two lanes. The results of the previous section thus generalizes this approach to the N-lane case in the presence of transverse currents.

Given two sets of equilibrated reservoirs at the left and right ends of the system, section 7.1.1 shows the equilibrated densities ρ_i^B observed in the bulk to satisfy

$$J_{\text{tot}}(\rho_1^B) = \begin{cases} \max_{\rho_1^B \in [\rho_1^R, \rho_1^L]} J_{\text{tot}}(\rho_1^B) & \text{for} \quad \rho_1^L > \rho_1^R \\ \min_{\rho_1^B \in [\rho_1^L, \rho_1^R]} J_{\text{tot}}(\rho_1^B) & \text{for} \quad \rho_1^L < \rho_1^R \,. \end{cases} \tag{7.4}$$

Note that the $N = 2$ case is rather atypical in that $K = 0$ automatically, the only non-zero stationary currents are thus longitudinal. For $N > 2$, non-zero transverse currents are generically present and it is perhaps surprising that they do not affect the extremal current principle.

7.2 Microscopic models of multilane systems

In the previous section we presented a linear stability analysis that allowed us to predict the phase diagrams of multilane systems starting from their hydrodynamic descriptions.

We now compare our theoretical predictions to various microscopic models. In particular, we discuss the validity of the generalized extremal current principle (7.4).

We consider N parallel lanes organized transversely "on a ring", as in Fig. 6.2: particles can hop from lane i to lane $i \pm 1$, with periodic boundary conditions. This allows us to study the phenomenology of non-zero transverse currents. We first consider $N = 10$ parallel TASEPs in section 7.2.1 before turning to a partial exclusion processes in section 7.2.2. Finally, in section 7.2.4 we discuss a case where, while the simple mean-field approximation we employ is not exact, the generalized extremal current principle still holds.

7.2.1 N TASEPs on a ring

We consider a system of length ℓ composed of N one-dimensional TASEPs. Particles hop along each lane at constant rates and there can be only one particle per site. Each lane is connected to reservoirs at its ends and particles can hop from lane i to the neighbouring lanes $i \pm 1$, giving rise to transverse currents between the lanes. For example, this could mimic the structure of microtubules which are composed of several protofilaments along and between which molecular motors can walk. Previously the case $N = 2$ has been considered (see for instance [46] and references therein) whereas the $N = 3$ case (without periodic boundary conditions in the transverse direction) has been studied numerically [150]. Here we show that indeed the system of N TASEPs for arbitrary N may be determined by the generalized ECP based on the total current.

A particle on lane i at site j can hop to the neighbouring site $j+1$ of lane i with rate p_i and on the site j of lanes $i \pm 1$ with rate $d_{i,i\pm1}$, provided the arrival site is empty. The microscopic mean-field equations, within the approximation of factorizing all density correlation functions, describing these N parallel TASEPs read

$$\begin{aligned}\frac{\mathrm{d}\rho_{i,j}}{\mathrm{d}t} &= p_i\,\rho_{i,j-1}(1-\rho_{i,j}) - p_i\,\rho_{i,j}(1-\rho_{i,j+1}) + \\ &+ d_{i-1,i}\,\rho_{i-1,j}(1-\rho_{i,j}) - d_{i,i-1}\,\rho_{i,j}(1-\rho_{i-1,j}) + \\ &+ d_{i+1,i}\,\rho_{i+1,j}(1-\rho_{i,j}) - d_{i,i+1}\,\rho_{i,j}(1-\rho_{i+1,j}),\end{aligned} \tag{7.5}$$

where $\rho_{i,j} = \langle n_{i,j}\rangle$ is the mean occupancy of the site j of lane i and we use transverse periodic boundary conditions by identifying lanes $i = N+1$ and $i = 1$.

We can now define the mean-field currents of the microscopic models:

$$\mathscr{J}_{ij} = p_i\,\rho_{i,j}(1-\rho_{i,j+1}) \tag{7.6}$$

$$\mathscr{K}_{(i,i+1)j} = d_{i,i+1}\,\rho_{i,j}(1-\rho_{i+1,j}) - d_{i+1,i}\rho_{i+1,j}(1-\rho_{ij}). \tag{7.7}$$

where $\mathscr{J}_{ij}$ is the mean-field approximation of the 'longitudinal' particle current between sites j and $j+1$ of lane i and $\mathscr{K}_{(i,i+1)j}$ is the mean-field approximation of the 'transverse' particle current between sites j of lanes i and $i+1$.

To obtain coarse-grained equations, we introduce the rescaled position $x = j/\ell$ along the lattices which now goes from $x = 0$ to $x = 1$. One then uses a standard Taylor expansion assuming that $\rho_{i,j}$ varies slowly from site to site along a given lane:

$$\rho_{i,j\pm1} \equiv \rho_i(x \pm 1/\ell) \simeq \rho_i(x) \pm \frac{1}{\ell}\frac{\partial \rho_i(x)}{\partial x} + \frac{1}{2\ell^2}\frac{\partial^2 \rho_i(x)}{\partial x^2}. \tag{7.8}$$

By keeping terms up to second order in gradients one can then write the coarse-grained mean-field equations:

$$\begin{aligned} \dot{\rho}_i(x) &= -\partial_x\left[J_i(\rho_i(x)) - D_i\partial_x\rho_i(x)\right] + \\ &\quad + K_{i-1,i}[\rho_{i-1}(x),\rho_i(x)] - K_{i,i+1}[\rho_i(x),\rho_{i+1}(x)] \end{aligned} \tag{7.9}$$

where

$$J_i(\rho_i(x)) = \frac{p_i}{\ell}\rho_i(x)\left[1-\rho_i(x)\right], \quad \text{and} \quad -D_i\partial_x\rho_i = -\frac{p_i}{2\ell^2}\partial_x\rho_i \tag{7.10}$$

are the advective and the diffusive parts of the mean-field current along lane i. We stress again that in the models we consider the longitudinal current of one lane depends solely on the occupancies in that lane. $K_{i,i+1}$ is the transverse current from lane i to lane $i+1$ defined as

$$K_{i,i+1}[\rho_i(x),\rho_{i+1}(x)] = d_{i,i+1}\rho_i(x)\left[1-\rho_{i+1}(x)\right] - d_{i+1,i}\rho_{i+1}(x)\left[1-\rho_i(x)\right], \tag{7.11}$$

with $K_{i,i+1} = -K_{i+1,i}$. In steady state, the equilibrated plateau (6.3) condition then reads

$$\forall i, \qquad K_{i,i+1} = -K_{i+1,i} = K \tag{7.12}$$

where periodic boundary conditions are implicit. At this stage, Eqs. (7.9), (7.10), and (7.11) completely define the hydrodynamic mean-field description of our model.

We proceed as follows: we first consider left and right equilibrated reservoirs of equal densities $\rho_1^R = \rho_1^L = \rho_1$; for each value of ρ_1, which is an input parameter, we solve the equilibrated mean-field Eqs. (6.3) to obtain $\rho_{i\neq1}^{L/R}(\rho_1)$, $K(\rho_1)$ and $J_{\text{tot}}(\rho_1)$, which we then use to predict the phase diagram. Let us first compare these mean-field predictions with the result of microscopic Monte Carlo simulations.

We show in Fig. 7.3 the results of simulations for $N = 10$ TASEPs on a ring, with $p_i = 1$ for all lanes and transverse rates: $d_{i,i+1} = 0.9$ and $d_{i+1,i} = 0.1$. For such transverse rates,

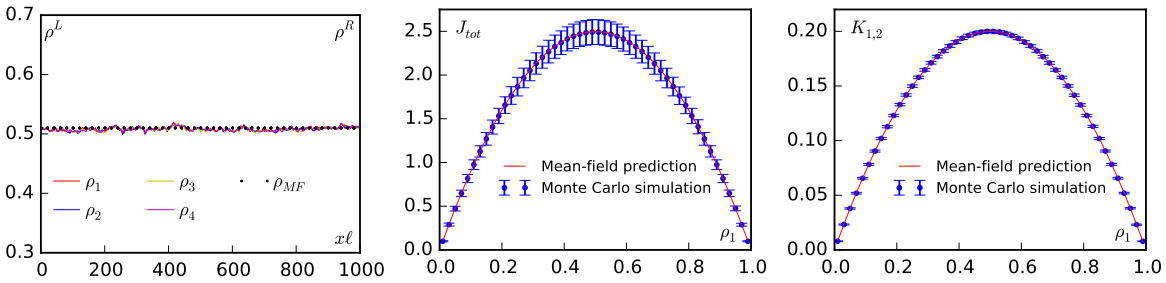

Figure 7.3 – Simulation results for $N = 10$ TASEPs on a ring, with $p_i = 1$ for all lanes and transverse rates: $d_{i,i+1} = 0.9$ and $d_{i+1,i} = 0.1$. **Left:** All density profiles are equal and coincide with the mean-field predictions. For sake of clarity, only the densities of lanes 1 to 4 are shown. ($\rho_1^L = \rho_1^R = 0.51$) **Center:** the total longitudinal current as a function of ρ_1; the maximum is at $\rho_1^M = 0.5$. **Right:** The transverse current between lane 1 and 2 corresponds to its mean-field description. As expected, all other currents $K_{i,i+1}$ are equal to $K_{1,2}$.

the equilibrated plateau condition simply forces the densities of all lanes to be equal. As predicted, we observe plateau profiles of densities $\rho_i(x) \simeq \rho_i^L = \rho_i^R$. The currents $J(\rho_1)$ and $K(\rho_1)$ are in agreement with their mean-field predictions. We can now use the generalized extremal current principle to construct the phase diagram of the system.

We proceed as in section 7.1: we first identify the extrema of the current and the regions where equilibrated plateaux can be connected to equilibrated reservoirs at different densities on their left or right ends (see the left panel of Fig. 7.4). We then use the extremal current principle to construct the phase diagram. As show in the right panel of Fig. 7.4, the agreement between the predicted phase diagram and the results of numerical simulations is very good.

The phase diagram shown in Fig. 7.4 is identical to that of a single TASEP. This shows that the frequently made assumption that the motion of molecular motors along a microtubule can be modelled by a single TASEP is indeed valid [76, 140]. Note, however, that the transverse current K is generically non-zero along the system (it follows the form of the longitudinal current J). Non-zero transverse currents have been observed experimentally, for instance for molecular motors that have helical trajectories along microtubules [147, 16, 104]. Our analysis thus covers the collective dynamics of such motors, suggesting that their propensity to form traffic jams should be identical to that of more standard motors [140, 84].

For the particular choice of rates made in this section, the equilibrated densities are equal across all lanes. The system thus has a particle-hole symmetry, and both $J(\rho_1)$ and $K(\rho_1)$ are symmetric with respect to $\rho_1 = 0.5$ (see right panels of Fig. 7.3). On the first-order transition line (see Fig. 7.4), K is therefore the same on both sides of a shock. We

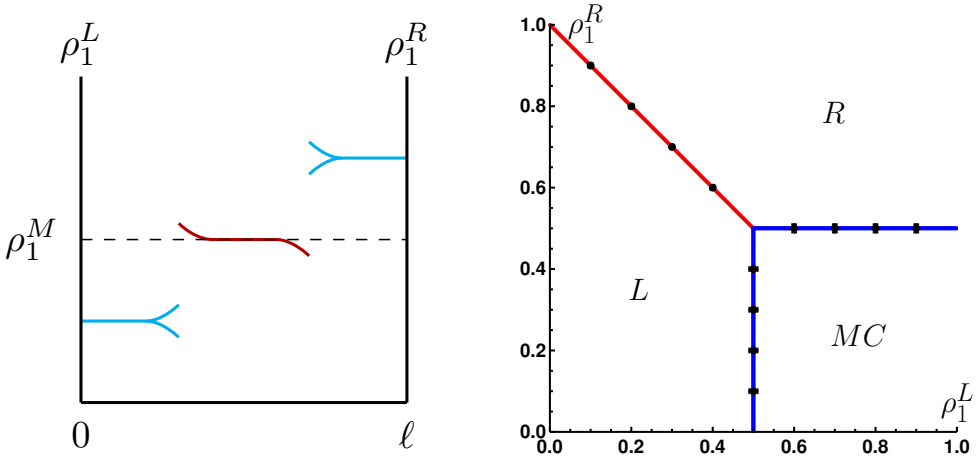

Figure 7.4 – Phase diagram for $N = 10$ TASEPs on a ring, with $p_i = 1$ for all lanes and transverse rates $d_{i,i+1} = 0.9$ and $d_{i+1,i} = 0.1$. **Left:** possible connections of equilibrated plateaux predicted by the linear stability analysis. **Right:** phase diagram where blue lines indicate second order phase transitions and the red line indicates a first order phase transition. Black error bars indicate the phase boundaries obtained by Monte Carlo simulations. The different phases are left (L), right (R) and maximal current phase (MC).

now turn to a more general system where this symmetry is violated and show that one can have coexistence between plateaux with very different values of the transverse current K.

7.2.2 Counter-rotating shocks

Let us now turn to more intriguing cases where the transverse current is not simply proportional to the longitudinal current. A particular example we consider is that of a transverse current which changes sign along the lane. A way of achieving a spatial reversal of K would be to have a transverse current $K(\rho)$ which changes sign as a function of density. Specifically, one could impose reservoir densities at the two ends of the system to have, say, clockwise and counter-clockwise flows imposed by the left and right reservoirs, respectively (see Fig. 7.5). Thus, at the boundaries the transverse currents have opposite signs. One can then wonder how the transverse flow in the bulk is selected when the system is "sheared" by such boundary conditions.

In order to achieve a transverse current $K(\rho)$ which changes sign as a function of density, one can first relax the condition that the transverse rates $d_{i,i+1}$ and $d_{i,i-1}$ are equal for all lanes. As we show in section 7.2.4, the equilibration condition then does not impose equal densities on all lanes. The transverse current K generically loses its particle-hole

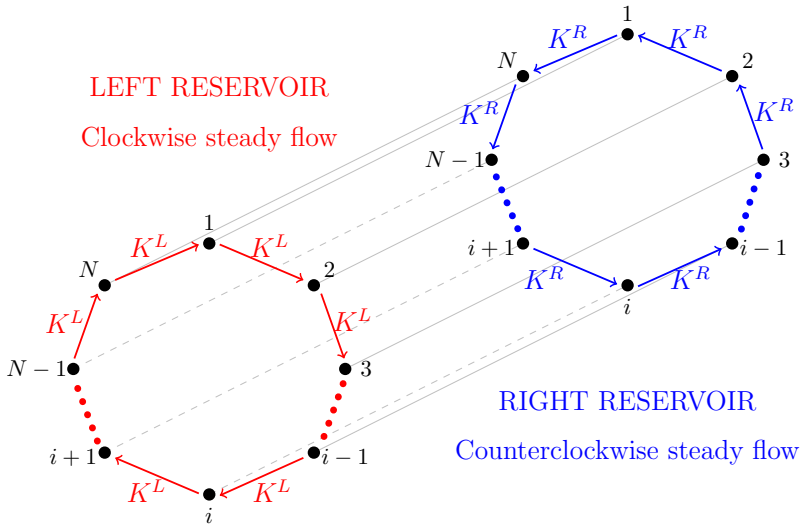

Figure 7.5 – Sketch of a system where $K(\rho^L)$ is positive and $K(\rho^R)$ is negative.

symmetry but, as we show in Appendix B.3, it cannot change sign as a function of the density for transverse rates of the form $d_{i,i\pm1}\rho_i(1-\rho_{i\pm1})$.

As we now show, a partial exclusion process, in which the restriction to at most one particle per site is relaxed, allows us to obtain the desired change of sign in the transverse current. Specifically, we study N parallel one-dimensional lattice gases in which up to $N_{\max}$ particles are allowed on each site. Particles hop from site j to $j+1$ on lane i with rate

$$W(i,j\to i,j+1) = p_i \frac{n_{i,j}}{N_{\max}}\left(1-\frac{n_{i,j+1}}{N_{\max}}\right) \tag{7.13}$$

and we refer to this as the Totally Asymmetric Partial Exclusion Process (TAPEP). For the transverse hopping rates from site j of lane i to site j of lane $i\pm1$, we choose

$$W(i,j\to i\pm1,j) = d_{i,i\pm1}\frac{n_{i,j}}{N_{\max}}\left(1-\frac{n_{i\pm1,j}}{N_{\max}}\right) \tag{7.14}$$

apart from the hopping from lane 1 to 2, in which we impose a different hopping rate:

$$W(2,j\to 1,j) = d_{2,1}\left(\frac{n_{2,j}}{N_{\max}}\right)^2\left(1-\frac{n_{1,j}}{N_{\max}}\right). \tag{7.15}$$

Note that in the case of the TASEP ($N_{\max}=1$) the hopping dynamics from lane 1 to 2 is the same as that between other lanes since $n_{2,j}^2 = n_{2j}$. Therefore we need to consider partial exclusion ($N_{\max}>1$) to observe novel behaviour.

To derive the hydrodynamic mean-field description of our model, we proceed as before, to obtain a dynamics given by (7.9), where we have introduced the mean densities

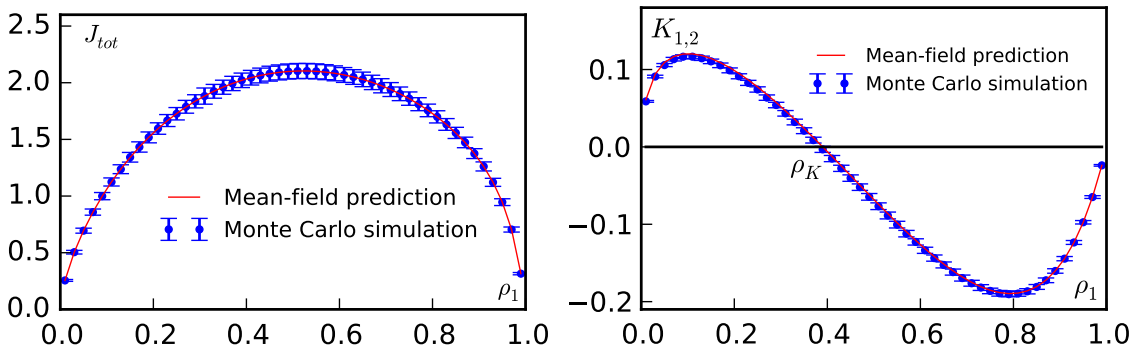

Figure 7.6 – Comparison of numerical simulations of 10 TAPEPs with mean-field predictions. **Left:** total longitudinal current as a function of ρ_1: the maximum is at $\rho_1^M = 0.52$. **Right:** transverse current between lane 1 and 2 (currents between all other pairs of lanes are the same). In the simulation we have set $N_{\max}$=100 and $p = 1$ for all the lanes. The transverse rates are: $d_{1,2} = 56$, $d_{2,3} = 89$, $d_{3,4} = 7$, $d_{4,5} = 27$, $d_{5,6} = 49$, $d_{6,7} = 45$, $d_{7,8} = 18$, $d_{8,9} = 8$, $d_{9,10} = 50$, $d_{10,1} = 62$, $d_{1,10} = 47$, $d_{2,1} = 78$, $d_{3,2} = 95$, $d_{4,3} = 94$, $d_{5,4} = 10$, $d_{6,5} = 41$, $d_{7,6} = 8$, $d_{8,7} = 15$, $d_{9,8} = 15$, $d_{10,9} = 79$.

$$\rho_{i,j} = \frac{\langle n_{i,j} \rangle}{N_{\max}} \,. \tag{7.16}$$

Advective and transverse currents are again given by (7.10) and (7.11), apart from $K_{1,2}$ whose expression is:

$$K_{1,2} = d_{1,2}\rho_1 \left(1-\rho_2\right) - d_{2,1} \left(\rho_2\right)^2 \left(1-\rho_1\right). \tag{7.17}$$

Using the methodology introduced in section 7.1, we can now compute, for equilibrated plateaux, the transverse and longitudinal currents $K(\rho_1)$ and $J_{\text{tot}}(\rho_1)$.

In Fig. 7.6, we compare the results of numerical simulations of 10 TAPEPs with mean-field predictions. Again, the agreement is excellent. Significantly, for the particular choice of transverse rate (7.15), $K(\rho_1)$ changes sign as ρ_1 varies, at $\rho_1 \equiv \rho_1^K$. Using the expression of $J_{\text{tot}}(\rho_1)$ and the generalized extremal current princle, we derive the phase diagram which is compared with Monte Carlo simulations in Fig. 7.7.

On the the red line of Fig. 7.7, one observes coexistence between two profiles of different densities separated by a shock. On this line, for $\rho^L < \rho_1^K$, these shocks separate the bulk of the system into homogeneous phases with counter-rotating transverse currents (see Fig. 7.8).

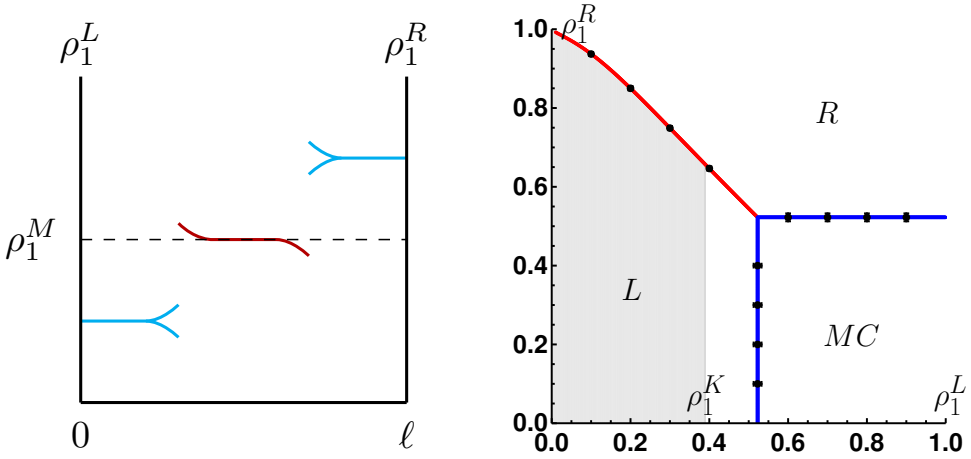

Figure 7.7 – Phase diagram of $N = 10$ TAPEPs with $N_{\max} = 100$. **Left:** possible connections of equilibrated plateaux predicted by the linear stability analysis. **Right:** phase diagram where blue lines indicate second order phase transitions and the red line indicates first order phase transitions. The different phases are left, right or maximal current phases. The gray shaded region corresponds to the region where $K > 0$ is observed in the bulk (bottom-left); in the rest of the phase diagram, one observes $K < 0$ in the bulk. The rates are the same as in Fig. 7.6.

7.2.3 Shear localization

The phenomenology shown in Fig. 7.8 is rather counterintuitive. Indeed, for a Symmetric Partial Exclusion Process which yields diffusive dynamics, one expects the density profile to linearly interpolate between the two reservoir densities. This in turn leads to a continuous variation of the transverse current K (see Fig. 7.9). In contrast, for the driven diffusive dynamics of the TAPEP, which leads to the formation of shocks, our analysis shows that a localized discontinuity of the transverse current may occur. Thus in the type of driven system we consider, it is the driven longitudinal dynamics which determine the phase behaviour and the transverse currents are dictated by the longitudinal ones.

For standard fluids, where momentum is conserved, such a shear discontinuity is unexpected [83]. Multilane models, based on random particle hopping, however describe situations where the momentum of the system is not even locally conserved. This is relevant, for instance, to models of molecular motors hopping along a microtubule without a proper description of the surrounding fluid. The shear localization phenomenon thus belongs to the class of surprising phenomena which can be observed in momemtum non-conserving systems (see [133] for how the concept of pressure can fail for such systems).

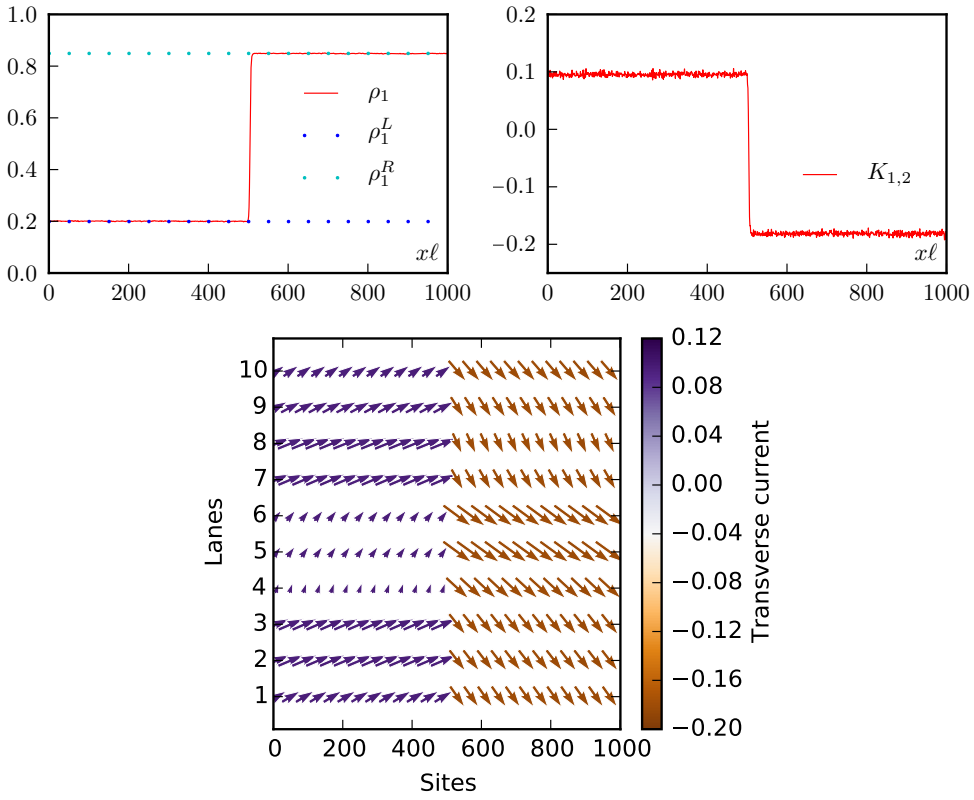

Figure 7.8 – Simulations of $N = 10$ TAPEPs with up to $N_{\max} = 100$ particles allowed per site. All longitudinal rates are equal ($p_i = p = 1$) whereas the transverse rates are chosen as follows: $d_{12} = 56$, $d_{21} = 47$, $d_{23} = 89$, $d_{32} = 78$, $d_{34} = 7$, $d_{43} = 95$, $d_{45} = 27$, $d_{54} = 94$, $d_{56} = 49$, $d_{65} = 10$, $d_{67} = 45$, $d_{76} = 41$, $d_{78} = 18$, $d_{87} = 8$, $d_{89} = 8$, $d_{98} = 15$, $d_{910} = 50$, $d_{109} = 15$, $d_{101} = 62$, $d_{110} = 79$. **Top-left:** the density profile of lane 1 exhibits a shock between a left and a right phase. The densities imposed at the two reservoirs are $\rho_1^L = 0.199$ and $\rho_1^R = 0.849$. **Top-right:** The transverse current between lane 1 and 2 similarly shows a shock between two values of opposite signs. **Bottom:** Vector field of the current $(J_i, K_{i,i+1})$ along the lattice. The color code shows the value of K. The length of the arrows corresponds to the modulus of the current vector.

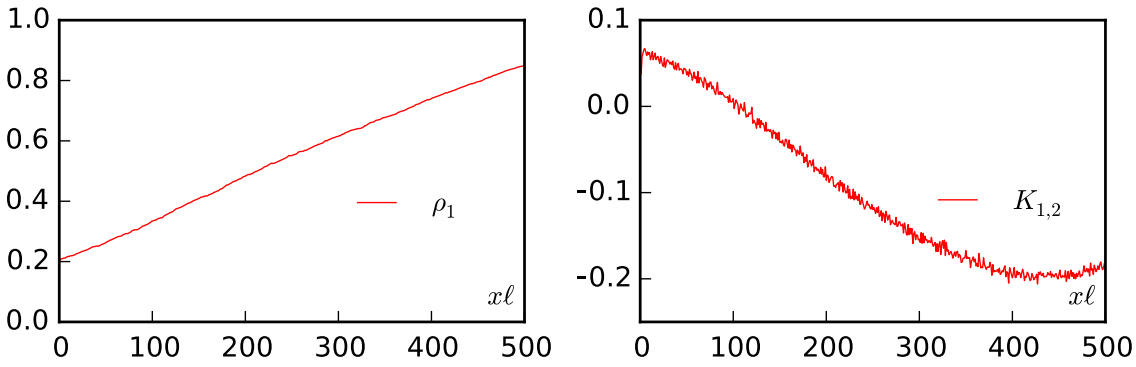

Figure 7.9 – Simulations of 10 Symmetric Partial Exlusion Processes. The simulation details are the same as in Fig. 7.8 with the exception of the longitudinal dynamics which is now symmetric, i.e. $p = q = 1$ for all lanes, where p and q are the forward and backward hopping parameters respectively. **Left:** density profile of lane 1 linearly interpolates between the left and right boundary conditions. The density values imposed at the two reservoirs are $\rho_1^L = 0.199$ and $\rho_1^R = 0.849$. **Right:** transverse current between lane 1 and 2 continuously interpolates between the left and right boundary conditions.

7.2.4 Beyond mean-field

The approach presented in this work relies on mean-field hydrodynamic descriptions of lattice-gases. We employed a simple mean-field approximation involving the factorization of all density correlations. In the aforementioned examples, this approach seems to perfectly predict the phase diagram observed in Monte Carlo simulations. As we now show, this is not always the case and the simple mean-field prediction for $J_{\text{tot}}(\rho_1)$ may fail. Despite of this, the extremal current principle can still be applied, but with the *numerically measured* current-density relation $J(\rho_1)$. This suggests that our approach solely relies on the existence of a hydrodynamic equation, Eq. (6.1), and not on the particular mean-field procedure we used here to derive it. Note that the same is true for single-lane systems. In [57] an exact current-density relation, differing from the mean-field prediction, was used to construct the phase diagram of a single-lane interacting lattice gas using the extremal current principle.

Let us now illustrate this by considering N parallel TASEPs where the transverse hopping rates are nonuniform. Furthermore, to allow for a richer phase diagram than those shown above, we alternate lanes where the particles hop rightwards, from site j to site $j+1$, with lanes where they hop leftwards, from site j to site $j-1$. The nonuniformity of the transverse hopping rates induces correlations between different lanes which are neglected within mean-field theory. As we show in Fig. 7.10, for a given example with 10 lanes and hopping rates specified in the caption, the profiles and currents calculated using the simple mean-field approximation do not match exactly the ones measured in the

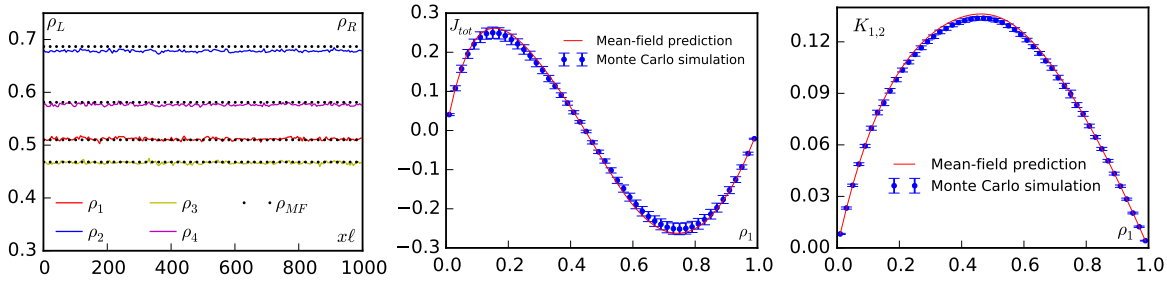

Figure 7.10 – Simulation results for $N = 10$ TASEPs on a ring. Even lanes ($i = 2,4,6,8,10$) correspond to right-going TASEPs whereas odd lanes ($i = 1,3,5,7,9$) correspond to left-going TASEPs; in all cases, the hopping rate is $p_i = 1$. The transverse rates are: $d_{1,2} = 0.95$, $d_{2,3} = 0.55$, $d_{3,4} = 0.72$, $d_{4,5} = 0.62$, $d_{5,6} = 0.79$, $d_{6,7} = 0.99$, $d_{7,8} = 0.81$, $d_{8,9} = 0.61$, $d_{9,10} = 0.93$, $d_{10,1} = 0.53$, $d_{2,1} = 0.05$, $d_{3,2} = 0.45$, $d_{4,3} = 0.02$, $d_{5,4} = 0.32$, $d_{6,5} = 0.19$, $d_{7,6} = 0.49$, $d_{8,7} = 0.01$, $d_{9,8} = 0.41$, $d_{10,9} = 0.03$, $d_{1,10} = 0.23$. **Left:** profiles of densities of lanes 1 to 4 are shown for $\rho_1^L = \rho_1^R = 0.51$. **Center:** total longitudinal current as a function of ρ_1: the maximum is at $\rho_1^M = 0.15$ while the minimum is at $\rho_1^m = 0.75$ (Monte Carlo values). **Right:** transverse current between lane 1 and 2 (currents between all other pairs of lanes are the same).

Monte Carlo simulations.

Consequently, the phase-diagram predicted by the mean-field expression, $J_{\text{tot}}(\rho_1)$, is slightly off its Monte Carlo counterpart. However, applying the extremal current principle instead on the numerically measured current-density relation yields a phase diagram which is in perfect agreement with the Monte Carlo simulations (see Fig. 7.11).

7.3 Conclusion

Our work shows that a generalized extremal current principle can be used to construct the phase diagram of multilane driven diffusive systems under the hypothesis that the hopping rate along one lane does not depend on the occupancies of the neighbouring lanes, and that the hopping rate between lanes increases with the occupancy of the departing site and decreases with the occupancy of the target site. This allowed us to show that the phase diagrams of such systems are equivalent to those of single-lane systems, though with much more complicated current-density relations. It validates the frequently made hypothesis that molecular motors hopping along microtubules can be effectively described by single-lane models. In all our modelling, we have used equilibrated reservoirs; all our results extends to the case of non-equilibrated reservoirs but with two new boundary layers connecting the bulk equilibrated plateaux with the reservoirs, as shown

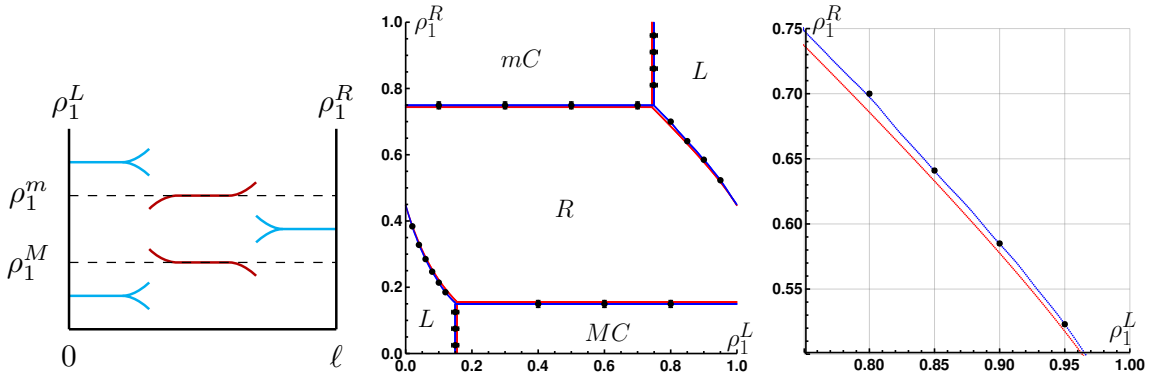

Figure 7.11 – Simulation results for $N = 10$ TASEPs on a ring, with the same parameters as in Fig. 7.10. **Left:** possible connections of equilibrated plateaux predicted by the linear stability analysis. **Center:** phase diagram where now red lines represent the result of the extremal current principle applied to the mean-field prediction and blue lines represent the result of the extremal current principle applied to the Monte Carlo simulation of J_{tot}. Black dots represent numerical simulations (with quite invisible errorbars) in the vicinity of phase transition lines. The possible phases are Left Phase, Right Phase, Maximal Current Phase and minimal Current Phase. **Right:** zoom on a region where the discrepancy between mean-field prediction and Monte Carlo simulation results are appreciable.

in Fig. 6.5. In this case, the relation between the densities of the bulk plateaux and those of the reservoirs is, however, not known in general.

Our theory is based on the analysis of hydrodynamic descriptions of lattice gases. To apply our approach to precise microscopic models one thus needs to construct such continuous descriptions, for instance using approximations such as the simple mean-field approximation we have employed here (cf. section 7.2.1). Those are known to fail when correlations between neighbouring sites are important but we have shown that the generalized extremal current principle still holds with respect to the exact current-density relation which can be measured in a simulation.

The existence of transverse currents, impossible for single and two lane systems, can lead to interesting phenomenology. For instance, we have shown that when a system has different transverse flows imposed at its boundaries, driven diffusive systems can have a bulk behaviour strongly different from simply diffusive systems. For the latter, the transverse flow smoothly interpolates between its imposed bundary conditions whereas driven dffusive systems can exhibit 'shear-localization'. The system then splits into homogeneous parts with constant transverse flows separated by sharp interface(s).

Our study extends the physics of one-dimensional boundary driven phase transitions to more complex systems and in particular to 2D lattices. It would be interesting to further pursue this approach with more general lattice structures, such as the network of

filaments encountered in active gels [102].

Conclusion

This thesis was dedicated to the study and investigation of two non-equilibrium systems at two different scales of the biological world. We have first studied the emerging collective behaviour of colonies of single and multispecies bacteria with specific interactions, before descending at the sub-cellular level with the investigation of the dynamics of populations of molecular motors[1].

When one is interested in finding the connection between microscopic interactions – where the equilibrium principle of detailed balance is not satisfied – and collective behaviours, it is inevitably necessary to start from microscopic models in order to build up macroscopic descriptions which can be studied with generic tools. We have shown with different techniques and approximations how it is possible to build up a hydrodynamic description of the macroscopic behaviours in the two cases – bacteria and molecular motors – starting from different models. The choice of the different procedures is dictated by the characteristics of the system under study: for instance, it is natural to model the dynamics of run-and-tumble bacteria – who swim in a continuous space – off lattice, while the dynamics of molecular motors – who move by discrete steps – was defined on lattice. Once a macroscopic mathematical description is obtained, standard tools such as linear analysis can then be used to study the behaviour of the system at a collective level. The results we obtained are clear signatures of non-equilibriumness:

- Bacteria can self-organize in patterns and spatio-temporal structures, thanks to the simple principle of accumulation where their transport efficiency is reduced. We were able to explain and characterize these structures, by a combination of theoretical and numerical tools, and the very good agreement with experimental results suggest that this mechanism can indeed be very general. Future development of techniques to measure and control the interactions in the experiments will open up exciting perspectives in *identifying* such simple principles in *in vivo* systems and *using* them to design functional communities.

- The motors, on the other hand, are capable of exhibiting phase transitions in one dimension. This allowed physicists to study transport problems with an extremely

[1] Note that, chronologically, part II of this thesis was the first project I tackled in my Ph.D.

simplified model, the TASEP. However, in most practical situations, general multilane problems are expected to be more relevant. We found that they can be mapped into single-lane systems by showing that they can yield the same phase diagram, at the price of a much more complicated current-density relation. However, the novelty is that they can now give rise to a much richer phenomenology, with several different phases, and to completely new features, such as shear localization.

Then, it is natural that to overcome the limits of the chosen models, one has to relax some of the constraints imposed by the approximations employed. For instance, in the case of phase separation in bacterial colonies, we neglected gradients that are known to be important to stabilize the interfaces. As for the multilane problems, the question remains open of how the phase diagram would be modified if we consider hopping rates between different lanes that depend on the occupancy of neighbouring sites. These represents interesting questions to be answered in future works.

To conclude, by studying two different problems, we have exemplified the fact that the use of system-specific models, approximations, and tools is typical of non-equilibrium problems, although the physicists' unrepentant hope of finding universal principles leads us to appeal to generic schemes, often coming from the equilibrium pot. Then, deviations from the expected behaviours are often a signature of new exciting features (or, even more often, of a bug in the code).

Appendix A

Methods and simulations of Part I

A.1 Coarse-graining with joint probability distribution

A.1.1 Diffusion-drift approximation

We recall the master equation for the probability density $P(\{\mathbf{r}_n,\theta_n,\sigma_n\},t)$

$$\begin{aligned}\dot{P} = &\sum_{\ell=1}^{N}\sigma_\ell\left[-\nabla_\ell\cdot(v_\ell\mathbf{u}_{\theta_\ell}P)-\alpha_\ell P+\frac{\beta_\ell}{2\pi}\int \mathrm{d}\theta'_\ell P_{\sigma_\ell=0}\right]\\ &+\sum_{\ell=1}^{N}(1-\sigma_\ell)[-\beta_\ell P+\alpha_\ell P_{\sigma_\ell=1}],\end{aligned} \tag{A.1}$$

and the moment expansion of P on the joint Fourier basis

$$P(\{\mathbf{r}_n,\theta_n,\sigma_n\}) = (2\pi)^{-N}\sum_{\{k_n\}} c_{k_1\dots k_N}(\{\mathbf{r}_n,\sigma_n\})\exp\left(i\sum_{j=1}^{N}k_j\theta_j\right). \tag{A.2}$$

To begin with, we consider the marginal probability $P_{\sigma_\ell} = P(\{\mathbf{r}_n,\theta_n\},\sigma_\ell) = \sum_{\sigma_{n\neq\ell}}P$ where the dynamical state variable of all the particles except ℓ have been eliminated by summation. The dynamics of P_{σ_ℓ} then reads:

$$\begin{aligned}\dot{P}_{\sigma_\ell} = &\sigma_\ell\left\{-\nabla_\ell\left[v_\ell\mathbf{u}_{\theta_\ell}P_{\sigma_\ell}\right]-\alpha_\ell P_{\sigma_\ell}+\frac{\beta_\ell}{2\pi}\int\mathrm{d}\theta'_\ell P_{\sigma_\ell=0}\right\}\\ &+(1-\sigma_\ell)\left\{-\beta_\ell P_{\sigma_\ell}+\alpha_\ell P_{\sigma_\ell=1}\right\}\\ &-\sum_{m\neq\ell}\nabla_m[v_m\mathbf{u}_{\theta_m}P_{\sigma_m=1,\sigma_\ell}].\end{aligned} \tag{A.3}$$

We then project (A.3) on the zeroth harmonic (that has $k_j = 0\ \forall\, j$) and obtain:

$$\begin{aligned}\dot{C}_0^{\sigma_\ell} = \sigma_\ell \left\{ -\nabla_\ell \left[\frac{v_\ell}{2} \left(C_{-\ell}^{\sigma_\ell} \begin{pmatrix} 1 \\ -i \end{pmatrix} + C_{+\ell}^{\sigma_\ell} \begin{pmatrix} 1 \\ i \end{pmatrix} \right) \right] - \alpha_\ell C_0^{\sigma_\ell} + \beta_\ell C_0^{\sigma_\ell=0} \right\} \\ + (1-\sigma_\ell) \left\{ -\beta_\ell C_0^{\sigma_\ell} + \alpha_\ell C_0^{\sigma_\ell=1} \right\} \\ - \sum_{m\neq\ell} \nabla_m \left[\frac{v_m}{2} \left(C_{-m}^{\sigma_m=1,\sigma_\ell} \begin{pmatrix} 1 \\ -i \end{pmatrix} + C_{+m}^{\sigma_m=1,\sigma_\ell} \begin{pmatrix} 1 \\ i \end{pmatrix} \right) \right].\end{aligned} \tag{A.4}$$

To eliminate the dependence of C_0 on σ_ℓ we define the probability of a system of N run-tumble-stop bacteria being in any dynamical state at position $\mathbf{r}_n$ at time t by summing over all possible values of σ_ℓ: $C_0 = \sum_{\sigma_\ell=0,1} C_0^{\sigma_\ell}$. We can now write the equation governing the dynamics of the density C_0:

$$\dot{C}_0 = -\sum_\ell \nabla_\ell \cdot \left[\frac{v_\ell}{2} \left(C_{-\ell}^{\sigma_\ell=1} \begin{pmatrix} 1 \\ -i \end{pmatrix} + C_{+\ell}^{\sigma_\ell=1} \begin{pmatrix} 1 \\ i \end{pmatrix} \right) \right]. \tag{A.5}$$

Eq. (A.5) is not yet a self-consistent equation because the dynamics of C_0 is expressed as a function of the first moment coefficients $C_{\pm\ell}^{\sigma_\ell=1}$: it is then necessary to study their dynamics. We do this by projecting Eq. (A.4) on the semi-space $\sigma_\ell = 1$, then on the first order harmonic $\exp(\pm i\theta_\ell)$. We therefore obtain

$$\begin{aligned}\dot{C}_{\pm\ell}^{\sigma_\ell=1} = -\nabla_\ell \cdot \left[\frac{v_\ell}{2} \left(C_0^{\sigma_\ell=1} \begin{pmatrix} 1 \\ \mp i \end{pmatrix} + C_{\pm 2\ell}^{\sigma_\ell=1} \begin{pmatrix} 1 \\ \pm i \end{pmatrix} \right) \right] - \alpha_\ell C_{\pm\ell}^{\sigma_\ell=1} \\ - \sum_{m\neq\ell} \nabla_m \left[\frac{v_m}{2} \left(C_{\pm\ell-m}^{\sigma_m=1,\sigma_\ell=1} \begin{pmatrix} 1 \\ -i \end{pmatrix} + C_{\pm\ell+m}^{\sigma_m=1,\sigma_\ell=1} \begin{pmatrix} 1 \\ i \end{pmatrix} \right) \right].\end{aligned} \tag{A.6}$$

From Eq. (A.6) we note that $\dot{C}_{\pm\ell}^{\sigma_\ell=1} \propto -C_{\pm\ell}^{\sigma_\ell=1}$, which tells us that $C_{\pm\ell}^{\sigma_\ell=1}$ is a fast variable. We therefore take the following fast variable approximation: $\dot{C}_{\pm\ell}^{\sigma_\ell=1} = 0$. This allows us to get an expression for $C_{\pm\ell}^{\sigma_\ell=1}$:

$$\begin{aligned}C_{\pm\ell}^{\sigma_\ell=1} = -\frac{1}{\alpha_\ell} \nabla_\ell \cdot \left[\frac{v_\ell}{2} \left(C_0^{\sigma_\ell=1} \begin{pmatrix} 1 \\ \mp i \end{pmatrix} + C_{\pm 2\ell}^{\sigma_\ell=1} \begin{pmatrix} 1 \\ \pm i \end{pmatrix} \right) \right] \\ - \frac{1}{\alpha_\ell} \sum_{m\neq\ell} \nabla_m \left[\frac{v_m}{2} \left(C_{\pm\ell-m}^{\sigma_m=1,\sigma_\ell=1} \begin{pmatrix} 1 \\ \mp i \end{pmatrix} + C_{\pm\ell+m}^{\sigma_m=1,\sigma_\ell=1} \begin{pmatrix} 1 \\ \pm i \end{pmatrix} \right) \right].\end{aligned} \tag{A.7}$$

If we now inserted expression (A.7) in (A.5) we still would not have a closed expression because of the second moments $C_{\pm 2\ell}^{\sigma_\ell=1}$ and $C_{\pm\ell\pm m}^{\sigma_m=1,\sigma_\ell=1}$. Again, we can try and characterize them by studying their dynamics. By the same proceeding as done for the first moments,

one can show that all second moments are also fast variables and that they are proportional to gradients of the density $C_0^{\sigma_\ell=1}$. Substituting their expression in (A.7) then leads to:

$$C_{\pm\ell}^{\sigma_\ell=1} = -\frac{1}{\alpha_\ell}\left\{\nabla_\ell \cdot \left[\frac{v_\ell}{2} C_0^{\sigma_\ell=1}\begin{pmatrix}1\\ \mp i\end{pmatrix}\right]\right\} + \mathcal{O}\left(\nabla^3 C_0^{\sigma_\ell=1}\right). \tag{A.8}$$

Inserting the expression for $C_{\pm\ell}^{\sigma_\ell=1}$ in (A.5) gives

$$\dot{C}_0 = \sum_\ell \nabla_\ell \left[\frac{v_\ell}{2\alpha_\ell}\nabla_\ell\left(v_\ell C_0^{\sigma_\ell=1}\right)\right] + \mathcal{O}\left(\nabla^4 C_0^{\sigma_\ell=1}\right). \tag{A.9}$$

We can now perform a gradient expansion that consists in neglecting the terms proportional to higher order in gradients. Finally, note that, by definition, $C_0 = C_0^{\sigma_\ell=1} + C_0^{\sigma_\ell=0}$. The closed expression we are looking for is the one in which only the quantity C_0 is involved, instead of the marginals $C_0^{\sigma_\ell=0}$ and $C_0 = C_0^{\sigma_\ell=1}$. We then study the dynamics of $C_0^{\sigma_\ell=0}$:

$$\begin{aligned}\dot{C}_0^{\sigma_\ell=0} &= -\beta_\ell C_0^{\sigma_\ell=0} + \alpha_\ell C_0^{\sigma_\ell=1} \\ &\quad - \sum_{m\neq\ell} \nabla_m \left[\frac{v_m}{2}\left(C_{-m}^{\sigma_m=1,\sigma_\ell=0}\begin{pmatrix}1\\ -i\end{pmatrix} + C_m^{\sigma_m=1,\sigma_\ell=0}\begin{pmatrix}1\\ i\end{pmatrix}\right)\right].\end{aligned} \tag{A.10}$$

We first note that $\dot{C}_0^{\sigma_\ell=0} \propto C_0^{\sigma_\ell=0}$: it is therefore a fast variable and $\dot{C}_0^{\sigma_\ell=0} = 0$. Then, one can easily show that the first harmonics appearing in the sum in Eq. (A.10) are fast variables too and that they are proportional to higher order gradients of the density. They can therefore be neglected, which gives

$$C_0^{\sigma_\ell=0} = C_0 - C_0^{\sigma_\ell=1} = \frac{\alpha_\ell}{\beta_\ell} C_0^{\sigma_\ell=1} \quad \rightarrow \quad C_0^{\sigma_\ell=1} = \frac{1}{1+\frac{\alpha_\ell}{\beta_\ell}} C_0 \tag{A.11}$$

and we finally obtain the closed expression:

$$\dot{C}_0 = \sum_\ell \nabla_\ell \left[\frac{v_\ell}{2\alpha_\ell}\nabla_\ell\left(\frac{v_\ell}{1+\frac{\alpha_\ell}{\beta_\ell}} C_0\right)\right] = \sum_\ell \nabla_\ell (D_\ell \nabla_\ell C_0 - \mathbf{F}_\ell C_0), \tag{A.12}$$

where

$$D_\ell = \frac{v_\ell^2}{2\alpha_\ell\left(1+\frac{\alpha_\ell}{\beta_\ell}\right)} \qquad \text{and} \qquad \mathbf{F}_\ell = -\frac{v_\ell}{2\alpha_\ell}\nabla_\ell \frac{v_\ell}{1+\frac{\alpha_\ell}{\beta_\ell}}. \tag{A.13}$$

A.1.2 Itō calculation for interacting bacteria

For the sake of clarity, we recall here the form of the Fokker-Planck equation for the probability density

$$\dot{C}_0 = \sum_\ell \nabla_\ell \cdot \left[\frac{v_\ell^2}{2\alpha_\ell \left(1+\frac{\alpha_\ell}{\beta_\ell}\right)} \nabla_\ell C_0 + \frac{v_\ell}{2\alpha_\ell} \nabla_\ell \frac{v_\ell}{1+\frac{\alpha_\ell}{\beta_\ell}} C_0 \right] \tag{A.14}$$

and the equivalent Langevin process for the trajectory of a single particle

$$\dot{\mathbf{r}}_\ell(t) = \mathbf{f}_\ell + \sqrt{2g_\ell}\,\eta_\ell(t), \quad \langle \eta_i^\mu(t)\eta_j^\nu(t')\rangle = \delta_{ij}\delta_{\mu\nu}\delta(t-t'), \tag{A.15}$$

with

$$\mathbf{f}_\ell = \frac{v_\ell}{1+\frac{\alpha_\ell}{\beta_\ell}} \nabla_\ell \frac{v_\ell}{2\alpha_\ell} \quad \text{and} \quad g_\ell = \frac{v_\ell^2}{2\alpha_\ell \left(1+\frac{\alpha_\ell}{\beta_\ell}\right)}. \tag{A.16}$$

Note that in the expressions (A.16) we have applied the substitutions (2.24) or, more generally, the one with the non-local coarse-grained density (2.25). Therefore, $g_\ell = g[\tilde{\rho}(\mathbf{r}_\ell)]$ and $\mathbf{f}_\ell = \mathbf{f}[\tilde{\rho}(\mathbf{r}_\ell)]$.

We now proceed in the computation of the time evolution of the density field $\rho(\mathbf{r},t) = \sum_\ell \rho_\ell(\mathbf{r},t) = \sum_\ell \delta(\mathbf{r}-\mathbf{r}_\ell(t))$, following Itō calculus:

$$\begin{aligned}
\dot{\rho}(\mathbf{r},t) &= \sum_{\ell=1}^{N} \left[(\nabla_\ell \rho_\ell)\dot{\mathbf{r}}_\ell + (\Delta_\ell \rho_\ell) g[\tilde{\rho}(\mathbf{r}_\ell)] \right] \\
&= \sum_\ell \left[(\nabla_\ell \rho_\ell) \left(\mathbf{f}[\tilde{\rho}(\mathbf{r}_\ell)] + \sqrt{2g[\tilde{\rho}(\mathbf{r}_\ell)]}\,\eta_\ell \right) + (\Delta_\ell \rho_\ell) g[\tilde{\rho}(\mathbf{r}_\ell)] \right] \\
&= \sum_\ell \Big[-\nabla \left(\delta(\mathbf{r}-\mathbf{r}_\ell)\mathbf{f}[\tilde{\rho}(\mathbf{r}_\ell)] \right) - \nabla(\delta(\mathbf{r}-\mathbf{r}_\ell)\sqrt{2g[\tilde{\rho}(\mathbf{r}_\ell)]}\,\eta_\ell) \\
&\qquad + \Delta(\delta(\mathbf{r}-\mathbf{r}_\ell) g[\tilde{\rho}(\mathbf{r}_\ell)]) \Big],
\end{aligned} \tag{A.17}$$

where ∇ and Δ are the gradient and the laplacian with respect to the space coordinate $\mathbf{r}$. Thus, since $\mathbf{f}[\tilde{\rho}(\mathbf{r}_\ell)]$ and $g[\tilde{\rho}(\mathbf{r}_\ell)]$ depend on the trajectories of the particles and not of the space coordinate, they can be included in the gradient and laplacian.

What we want to do next is to express the RHS of Eq. (A.17) as a function of $\rho(\mathbf{r},t)$ by exploiting its definition. In order to do this we have to re-write $\mathbf{f}[\tilde{\rho}(\mathbf{r}_\ell)]$ and $g[\tilde{\rho}(\mathbf{r}_\ell)]$ in such a way that they do not depend on ℓ anymore. Let us start with the last term in Eq. (A.17):

$$\begin{aligned}
\sum_\ell \Delta\left(\delta(\mathbf{r}-\mathbf{r}_\ell) g_\ell(\mathbf{r}_\ell)\right) &= \sum_\ell \Delta\left(\delta(\mathbf{r}-\mathbf{r}_\ell) g[\tilde{\rho}(\mathbf{r}_\ell)]\right) \\
&= \sum_\ell \Delta\left(\delta(\mathbf{r}-\mathbf{r}_\ell) g[\tilde{\rho}(\mathbf{r})]\right) \\
&= \Delta\left(\rho(\mathbf{r}) g[\tilde{\rho}(\mathbf{r})]\right).
\end{aligned} \tag{A.18}$$

The second term can be treated similarly, but some more attention has to be paid because of the multiplicative noise:

$$\sum_\ell \nabla(\delta(\mathbf{r}-\mathbf{r}_\ell)\sqrt{2g_\ell(\mathbf{r}_\ell)}\,\eta_\ell(t)) = \nabla\left(\sqrt{2g[\tilde{\rho}(\mathbf{r})]}\sum_\ell \delta(\mathbf{r}-\mathbf{r}_\ell)\eta_\ell(t)\right). \tag{A.19}$$

Following [39] one can show that the noise term in Eq. (A.19) has the same correlations of

$$\nabla\left(\sqrt{2g[\tilde{\rho}(\mathbf{r})]\rho(\mathbf{r})}\,\Lambda(\mathbf{r},t)\right), \quad \langle\Lambda_\mu(\mathbf{r},t)\Lambda_\nu(\mathbf{r}',t')\rangle = \delta_{\mu\nu}\delta(\mathbf{r}-\mathbf{r}')\delta(t-t'). \tag{A.20}$$

In the first term, in order to make the total density $\rho(\mathbf{r},t)$ appear, we have to detail the computation more. We first re-write (2.25) from the main text as

$$\tilde{\rho}(\mathbf{r}_\ell) = \int \mathrm{d}\mathbf{y}\, K(\mathbf{y}-\mathbf{r}_\ell)\rho(\mathbf{y}) = \int \mathrm{d}\mathbf{y}\, K(\mathbf{y}-\mathbf{r}_\ell)\sum_j \delta(\mathbf{y}-\mathbf{r}_j) = \sum_j K(\mathbf{r}_j-\mathbf{r}_\ell) \tag{A.21}$$

then consider the function $\mathbf{f}_\ell(\mathbf{r}_\ell)$ as a gradient of some generic function $h_\ell(\mathbf{r}_\ell)$:

$$\begin{aligned}
\mathbf{f}_\ell(\mathbf{r}_\ell) &= \nabla_\ell h_\ell(\mathbf{r}_\ell) \\
&= \nabla_\ell h[\tilde{\rho}(\mathbf{r}_\ell)] \\
&= \nabla_\ell h\left[\sum_j K(\mathbf{r}_j-\mathbf{r}_\ell)\right] \\
&= h'[\tilde{\rho}(\mathbf{r}_\ell)]\left(\sum_j \nabla K(\mathbf{r}_j-\mathbf{r}_\ell)\right),
\end{aligned} \tag{A.22}$$

where ∇K is the gradient with respect to its argument. We now consider and develop

$$\begin{aligned}
\sum_\ell \delta(\mathbf{r}-\mathbf{r}_\ell)\mathbf{f}_\ell &= \sum_\ell \delta(\mathbf{r}-\mathbf{r}_\ell)h'[\tilde{\rho}(\mathbf{r}_\ell)]\sum_j \nabla K(\mathbf{r}_j-\mathbf{r}_\ell) \\
&= \sum_\ell \delta(\mathbf{r}-\mathbf{r}_\ell)h'[\tilde{\rho}(\mathbf{r})]\nabla\left(\sum_j K(\mathbf{r}_j-\mathbf{r})\right) \\
&= \sum_\ell \delta(\mathbf{r}-\mathbf{r}_\ell)h'[\tilde{\rho}(\mathbf{r})]\nabla\tilde{\rho}(\mathbf{r}) \\
&= \sum_\ell \delta(\mathbf{r}-\mathbf{r}_\ell)\nabla h[\tilde{\rho}(\mathbf{r})] \\
&= \sum_\ell \delta(\mathbf{r}-\mathbf{r}_\ell)\mathbf{f}[\tilde{\rho}(\mathbf{r})] \\
&= \rho(\mathbf{r})\mathbf{f}[\tilde{\rho}(\mathbf{r})].
\end{aligned} \tag{A.23}$$

Eq. (A.17) takes thus the form

$$\begin{aligned}\dot{\rho}(\mathbf{r},t) &= -\nabla\left[\rho(\mathbf{r},t)\mathbf{f}[\tilde{\rho}(\mathbf{r})] + \sqrt{2g[\tilde{\rho}(\mathbf{r})]\rho(\mathbf{r},t)}\,\Lambda(\mathbf{r},t) - \nabla(\rho(\mathbf{r},t)g[\tilde{\rho}(\mathbf{r})])\right] \\ &= -\nabla\left[\rho\left(\frac{v}{1+\frac{\alpha}{\beta}}\nabla\frac{v}{2\alpha}\right) + \sqrt{2\frac{v^2}{2\alpha\left(1+\frac{\alpha}{\beta}\right)}\rho}\,\Lambda_A - \nabla\left(\rho\frac{v^2}{2\alpha}\right)\right] \\ &= -\nabla\left[-\frac{v^2}{2\alpha\left(1+\frac{\alpha}{\beta}\right)}\nabla\rho - \frac{v}{2\alpha}\nabla\frac{v}{1+\frac{\alpha}{\beta}}\rho + \sqrt{2\frac{v^2}{2\alpha\left(1+\frac{\alpha}{\beta}\right)}\rho}\,\Lambda\right] \\ &= -\nabla\left[-D[\tilde{\rho}]\nabla\rho + \mathbf{F}[\tilde{\rho}]\rho + \sqrt{2D[\tilde{\rho}]\rho}\,\Lambda\right],\end{aligned} \tag{A.24}$$

which is Eq. (2.30) in the main text.

A.2 Simulation details

A.2.1 Off-lattice microscopic simulations

A.2.1.1 General features and time evolution

In the off-lattice simulations, particle k with $1 \le k \le N$ is associated to the following variables:

- the position, in terms of a couple of continuous variables (x_k, y_k) with $0 \le x_k, y_i < L$ and L is the size of the system;
- the orientation, in terms of a continuous variable θ_k with $0 \le \theta_k < 2\pi$;
- the coarse-grained density $\tilde{\rho}_k = \sum_\ell K_{k\ell}/Z$, where Z is a normalization constant, $K_{k\ell}$ the interaction kernel of particle k with particle ℓ and the sum runs over the particles ℓ whose position is within a certain range r_0 from the position of particle k. We choose the interaction kernel to take the form $K_{k\ell} = \exp\left(-\frac{1}{1-(r_{k\ell}/r_0)^2}\right)$, so that it is symmetric around k and it decreases as the distance between the two particles $r_{k\ell}$ increases. In the multispecies mutual interaction case, particles ℓ do not belong to the same species of particle k;
- a discrete variable σ indicating if the particle is running ($\sigma = 1$) or tumbling ($\sigma = 0$). This last variable is not present in simulations with instantaneous tumbling.

The simulation is performed in discrete time with parallel update: at each time step dt, the coarse-grained density is first computed for each particle. Then, all particles move of a

distance $dr = v\,dt$. Depending on the case, v can be constant or density-dependent. The run-to-tumble and tumble-to-run events occur randomly at frequency α and β, which again, depending on the case, can be constant or density-dependent. When a tumble-to-run event occurs, the new orientation of the particle is chosen at random.

If birth and death is included, an additional step must be considered during which the particles are either added at rate $b = b_0$, or deleted at rate $d(\rho)$, an increasing function of the local density. Note that in our convention, the birth and death events are exclusive: if one particle just divided, it cannot die at the same time step.

A.2.1.2 Calculation of the coarse-grained density

Only particles within a distance r_0 contribute to each other's coarse-grained density so that performing a loop on all the N particles at each time step would be redundant and extremely time-consuming. What we want to do instead, is a loop on only those particles within the interaction distance. In order to do this, we discretize the space in such a way that each lattice site has a size $a \geq r_0$. We then associate to each site a chained list[1], corresponding to the particles present on that site at that specific time. To compute the coarse-grained density around particle k at site (i, j), we therefore only look at particles at the same site and at the neighbouring ones.

A.2.2 On-lattice microscopic simulations

A.2.2.1 General features and time evolution

In on-lattice simulations, the position and the orientation of the particles are discretized. For the particles' position, it just corresponds to the lattice site coordinates; for their orientation, we choose to let them move in 4 directions: vertical, horizontal, and the two diagonals. They can therefore have 8 possible orientations, 2 for each direction. If we consider finite tumble duration, each particle is also associated with the discrete variable $\sigma = 0, 1$ indicating that the particle is in a tumble or run state, respectively. Finally, both the local and the coarse-grained densities, whose computation method is explained in next section, are associated not with the particles themselves, but with the site.

In this case, the time evolution is implemented with random sequential update: we divide the time step dt in N microsteps of size $\delta t = dt/N$ and for each microstep we randomly select one of the N particles. If N is large then δt is small and the process is almost

[1] A chained list is a series of pointers, each of which points to the next element in the list. It is then very easy to go through the list and add/remove elements from it.

identical to an ordered sequential update [19, p. 26]: on average, all the N particles are selected at each time step dt.

Once the particle is selected, it then performs an action, according to its state and orientation. If the particle is in the run state, it can either move (at rate v in the vertical and horizontal direction, at rate $v/\sqrt{2}$ in the two diagonal directions), tumble (at rate α), or do nothing. If the particle is in the tumble state, it can either resume a run (at rate β) in a randomly chosen direction, or do nothing. If we consider birth (occurring at rate b) and death (occurring at rate d), those events are included in the possible actions for both running and tumbling particles. Note that when a particle is added (following a birth event) or deleted (following a death event) the microstep δt is modified). Once again, depending on the specific model, all the rates are constant or density-dependent. To select which action is performed, we use the tower sampling algorithm.

The advantage of sequential as opposed to parallel update is that in the first case it is not necessary to compute the coarse-grained densities for all the sites at each time step, which is the most time-consuming computation in the simulation. The drawback is that it can be used only in those cases where the effect of one particle's action on the system configuration state is very small: in our case, for instance, when particle on site (i, j) at time t moves, dies, or replicates, it affects the local density of site (i, j) and the coarse-grained density of all the sites that interact with site (i, j). If at time $t + n\delta t$, with $n < N$, a particle that lies within the interaction range from site (i, j) is selected, its action is influenced by what happened to the first particle at time t, giving rise to artificial correlations between the two actions, which should in principle occur at the same time and therefore be independent. However, if the density is large enough, the correlation introduced should be negligible.

A.2.2.2 Calculation of the coarse-grained density

We consider the particles on site (i, j) and an interaction range $r_0 \geq 1$. They thus interact with particles on sites (i_n, j_n) such that $r_n = \sqrt{(i - i_n)^2 + (j - j_n)^2} \leq r_0$. If the number of sites that satisfy $r_n \leq r_0$ is m, then the coarse-grained densities of particles on site (i, j) is simply the sum of all the particles on the m sites divided by m. This is equivalent to take a quasi-circular step-like interaction kernel. This computation is done only once for all the sites at the beginning of the simulation. Then, during the simulation, the coarse-grained density is updated every time a particle changes site, only for the sites concerned by the displacement, i.e. those that determine the perimeter of the interaction area. This allows to perform $n_r \sim r_0$ calculations instead of $N_r \sim r_0^2$ at each microstep δt.

Appendix B

Methods of Part II

B.1 Dynamical stability of equilibrated plateaux

Consider a small perturbation $\delta\rho$ around the equilibrated plateau solution (see section 6.1.1) which may be decomposed as

$$\rho_i(x,t) = \rho_i^0 + \sum_q \delta\rho_i^q(t)\exp\big(iqx\big), \tag{B.1}$$

where $q = 2\pi n$ with $n = 1,\dots,\ell-1$. We denote by $|\delta\rho^q)$ the vector $(\delta\rho_1^q,\dots\delta\rho_N^q)$. Inserting expression (B.1) into the mean-field equations (7.9) and expanding to first order in $\delta\rho_i^q$ yields the equation

$$\frac{\mathrm{d}}{\mathrm{d}t}|\delta\rho^q) = C^q|\delta\rho^q), \tag{B.2}$$

where the matrix C^q is defined by

$$C_{ii}^q = -D_i q^2 - \mathrm{i}qJ_i^i + \sum_{j\neq i} K_{ji}^i; \qquad C_{ij\neq i}^q = K_{ji}^j, \tag{B.3}$$

with $J_i^i \equiv \partial_{\rho_i} J_i(\rho^0)$. Note that the matrix C_{ii}^q can be defined for any positive real number q and not only for the discrete values $q = 2\pi n$. As we now show, the eigenvalues $\lambda_i(q)$ of the matrix C^q always have negative real parts and $|\delta\rho^q(t))$ thus vanishes at large time.

For $q = 0$, C^q is a Markov matrix and none of its eigenvalues $\lambda_i(0)$ has a positive real part: Eq. (B.3) indeed shows the sum of each column elements to vanish for $q = 0$. Conversely, when $q \to \infty$, $\lambda_i(q) \sim -D_i q^2$ and $\lambda_i(q)$ thus has a negative real part. Physically, the short wave-length perturbations are stabilized by the diffusive terms while the large wave-length perturbations are stabilized by the exchange between lanes.

The eigenvalues of a matrix are continuous functions in $\mathbb{C}$ of its coefficients. For $C(q)$ to have an eigenvalue with a positive real part, we need $q^* \in [0,\infty[$ such that at least one

eigenvalue satisfies $\mathrm{Re}(\lambda_i(q^*)) = 0$, which means

$$\exists |v) \neq 0 \qquad \text{such that} \qquad C^q|v) = i\varphi|v), \quad \text{where} \quad \varphi \in \mathbb{R}. \tag{B.4}$$

The matrix $A \equiv C^q - i\varphi\mathbb{I}$ is thus singular. It is however easy to see that A^t, the transpose of A, is a strictly diagonally dominant matrix, i.e.

$$\begin{aligned} |A^t_{ii}| &= |D_i q^2 + \Big(\sum_{j\neq i} K^i_{ij}\Big) + \mathrm{i}(qJ^i_i + \varphi)| \\ &> \sum_{j\neq i} |A^t_{ij}| = \sum_{j\neq i} |K^i_{ij}| = |\sum_{j\neq i} K^i_{ij}|. \end{aligned} \tag{B.5}$$

The Gershgorin circle theorem states that all eigenvalues of a square matrix B can be found within one of the circles centered on B_{ii} of radii $\sum_{j\neq i} |B_{ij}|$. This implies that strictly diagonally dominant matrices cannot be singular: A^t and A are thus invertible. Therefore, the matrix $C(q)$ cannot have purely imaginary eigenvalues: all its eigenvalues thus have a negative real part for all q. Equilibrated plateaux are thus always dynamically stable when J_i is only a function of ρ_i and when Eqs. (6.2) are satisfied. This can break down for more general systems, when interactions between the lanes are allowed for [46].

B.2 Connecting bulk plateaux to equilibrated reservoirs

This appendix is divided into two parts. In the first part, we show that the spectrum of M is composed of either (i) N eigenvalues with positive real parts and $N-1$ eigenvalues with negative real parts, or (ii) $N-1$ eigenvalues with positive real parts and N eigenvalues with negative real parts. The second part then shows that these two cases respectively correspond to plateaux which can only be observed in Left and Right phases.

B.2.1

We begin by considering a semi-infinite problem with a reservoir at the left end of the system. Let us assume that the equilibrated plateaux densities ρ^{p}_j are determined by single-valued (a priori unknown) functions of the reservoir densities $|\rho^L)$:

$$\forall j \qquad \rho^{\mathrm{p}}_j = H_j(\rho^L_1, \ldots, \rho^L_N), \tag{B.6}$$

When the reservoir is equilibrated, one simply has $\rho^{\mathrm{p}}_j = H_j(\rho^L_j) = \rho^L_j$. We now focus on perturbations of equilibrated reservoirs and show that the space of perturbations $|\delta\rho^L)$ that leave $|\rho^{\mathrm{p}})$ invariant is of dimension $N-1$.

To see this, let us look at the consequence of an infinitesimal perturbation $|\delta\rho^L)$ of the reservoir densities. This perturbation results in a change of bulk equilibrated densities from $|\rho^{\rm p})$ to $|\rho^{\rm p}) + |\delta\rho^{\rm p})$, with

$$\delta\rho_j^{\rm p} = \sum_i \left(\partial_{\rho_i^L} H_j\right) \delta\rho_i^L, \tag{B.7}$$

which can be rewritten in matrix form as

$$|\delta\rho^{\rm p}) = H'|\delta\rho^L) \quad \text{where} \quad H'_{ji} \equiv \partial_{\rho_i^L} H_j. \tag{B.8}$$

By definition the bulk densities $|\rho^{\rm p}) + |\delta\rho^{\rm p})$ are still equilibrated. Therefore, as shown in section 6.2.1, $|\delta\rho^{\rm p}) = \epsilon|\delta\rho^0)$, where ϵ is a small parameter and thus

$$H'|\delta\rho^L) = \epsilon|\rho^0). \tag{B.9}$$

The key observation is that since Eq. (B.9) holds for any perturbation $|\delta\rho^L)$, the matrix H' projects any vector $|\delta\rho^L)$ onto the direction $|\delta\rho^0)$. Furthermore, we now show that H' is indeed a projector satisfying $(H')^2 = H'$. Since $H'|\delta\rho^L) \propto |\delta\rho^0)$, the image of H' is Span$|\delta\rho^0)$. If we consider an equilibrated boundary density vector $|\rho^L)$ then $|\rho^L + \epsilon\delta\rho^0)$ is also equilibrated, which implies $H(|\rho^L + \epsilon\delta\rho^0)) = |\rho^L) + \epsilon|\delta\rho^0)$. Then by linearization, $H'|\delta\rho^0) = |\delta\rho^0)$. Since (B.9) holds for all $|\delta\rho^L)$, H' thus satisfies $\left(H'\right)^2 = H'$.

We may now invoke a basic theorem of linear algebra that for a projector, here H', the direct sum of the image space and the kernel gives the full N dimensional vector space:

$$\mathbb{R}^N = \text{Span}(|\delta\rho^0)) \oplus \ker(H'). \tag{B.10}$$

Note that $\ker(H')$ is the space of perturbations $|\delta\rho^L)$ that leave $|\rho^{\rm p})$ invariant (since $H'|\delta\rho^{\rm r}) = |\delta\rho^{\rm p}) = 0$). Therefore the space of perturbations $|\delta\rho^L)$ that leave the bulk density vector invariant is of dimension $N-1$.

To connect these perturbations to the eigenvectors of the matrix M, let us consider a given equilibrated plateau $|\rho^{\rm p})$ and ask which reservoir density vectors $|\rho^{\rm p} + \delta\rho^{\rm r})$ it can be connected to through a perturbation $|\delta\rho(x))$. Such a perturbation can be decomposed using the eigenvectors of M as in Eq. (6.14):

$$|\delta\rho(x)) = \sum_{k=1}^{2N-1} \alpha_k |\delta\rho^k) e^{\lambda_k x}. \tag{B.11}$$

By definition, $|\delta\rho(x))$ vanishes in the bulk of the system (see Fig. 6.6) so there is no α_0 term in the sum.

The sum in (B.11) is restricted to $\mathrm{Re}(\lambda_k) < 0$ when connecting to left reservoirs as terms coming from eigenvectors with eigenvalues with $\mathrm{Re}(\lambda_k) \geq 0$ would not die out in the bulk. Since $|\delta\rho(x=0)) = |\delta\rho^{\mathrm{r}})$, the perturbations (B.11) need to span the sets of left reservoir perturbations that leave $|\rho^{\mathrm{p}})$ invariant. Since the vector spaces of such perturbations are $N-1$ dimensional, one needs at least $N-1$ eigenvectors with $\mathrm{Re}(\lambda_k) < 0$. Conversely, the same reasoning for a semi-infinite system connected to a reservoir on its right would lead to the conclusion that one needs at least $N-1$ eigenvectors with $\mathrm{Re}(\lambda_k) > 0$.

To conclude the first part of this appendix, let us summarize what we know on the spectrum of the matrix M. Since it has $2N$ eigenvectors, one of which is associated with the eigenvalue $\lambda_0 = 0$, among the remaining $2N-1$ there must be either $N-1$ eigenvectors with $\mathrm{Re}(\lambda_k) < 0$ and N eigenvectors with $\mathrm{Re}(\lambda_k) > 0$ or $N-1$ eigenvectors with $\mathrm{Re}(\lambda_k) > 0$ and N eigenvectors with $\mathrm{Re}(\lambda_k) < 0$.

B.2.2

We now show that the first case, with $N-1$ eigenvectors with $\mathrm{Re}(\lambda_k) < 0$ and N eigenvectors with $\mathrm{Re}(\lambda_k) > 0$, corresponds to a Left Phase.

1. **Connection to left reservoirs**. As we have shown, there is a space of perturbations $|\delta\rho^{\mathrm{r}})$ of dimension $N-1$ that leave $|\rho^{\mathrm{p}})$ invariant. Since these are spanned by the $N-1$ eigenvectors with $\mathrm{Re}(\lambda_k) < 0$, the latter constitute a basis of $\ker[H'(\rho^{\mathrm{p}})]$ and one can construct a perturbation $|\delta\rho(x))$ that connects ρ^{p} to the reservoir $\rho^{\mathrm{p}} + \delta\rho^{\mathrm{r}}$.

   Let us now consider a small equilibrated perturbation $|\delta\rho^{\mathrm{r}}) = \alpha|\delta\rho^0)$ of $|\rho^{\mathrm{r}})$ for which there exists a stationary profile connecting $|\rho^{\mathrm{p}})$ to $|\rho^{\mathrm{r}}) + \alpha|\delta\rho^0)$. Since the profile connects to the reservoir at $x = 0$, one needs to find a decomposition of $|\delta\rho(x))$ such that

   $$|\delta\rho(0)) = \sum_{\mathrm{Re}(\lambda_k)<0} \alpha_k |\delta\rho^k) = \alpha|\delta\rho^0). \tag{B.12}$$

   However, since H' is a projection on $|\delta\rho^0)$ and $\mathrm{Span}(|\delta\rho^k), \mathrm{Re}(\lambda_k) < 0) = \ker(H')$, Eq. (B.10) applies and the intersection between $\ker H'$ and $\mathrm{Span}[|\delta\rho^0)]$ is the empty set. As a consequence, $\delta\rho_i(0)$, which belongs to both sets because of (B.12), is the null vector ($\alpha_k = \alpha = 0$): the sole equilibrated reservoir to which ρ^{p} can be connected to the left corresponds to $|\rho^{\mathrm{r}}) = |\rho^{\mathrm{p}})$.

2. **Connection to right reservoirs**. We now consider only the N eigenvectors with $\mathrm{Re}(\lambda_k) > 0$. While they still span $\ker(H')$, and $|\rho^{\mathrm{p}})$ can still be connected to unequilibrated reservoirs on the right, the $|\delta\rho^k)$ need not anymore be in $\ker(H')$. Let

us show that $|\rho^{\mathrm{p}})$ can be connected to an equilibrated reservoir on the right with $|\delta\rho^{\mathrm{r}}) \neq 0$. Again, this requires a perturbation $|\delta\rho)$ which satisfies

$$\sum_{\mathrm{Re}(\lambda_k)>0} \alpha^k |\delta\rho^k) = \epsilon |\delta\rho^0), \tag{B.13}$$

Let us first remember that the eigenvectors $|v^k\rangle$ of $M(\rho^{\mathrm{p}})$ are $2N$-dimensional and that $|\delta\rho^k)$ are simply the second half of the components of these vectors. We want to show that $|\delta\rho^0) \in \mathrm{Span}[|\delta\rho^k), \mathrm{Re}(\lambda_k) > 0]$. To do so, we consider the vector space $X = \{(x_1, \ldots, x_N, 0, \ldots, 0), x_i \in \mathbb{R}\}$ of dimension N. The eigenvector associated to $\lambda = 0$ is $|v^0\rangle = \left(0, \ldots, 0, \delta\rho_1^0, \ldots, \delta\rho_N^0\right)$ and clearly $|v^0\rangle \notin X$. From this we can say that

$$\dim(X + \mathrm{Span}|v^0\rangle) = N + 1. \tag{B.14}$$

Since one also has

$$\begin{aligned} &\dim[\mathrm{Span}[|v^k\rangle, \mathrm{Re}(\lambda_k) > 0]] = N \quad \text{and} \\ &\dim[(X + \mathrm{Span}|v^0\rangle) + (\mathrm{Span}|v^k\rangle)] \leq 2N \end{aligned} \tag{B.15}$$

(the total space is $2N$ dimensional), it follows that

$$\begin{aligned} \dim[(X + \mathrm{Span}|v^0\rangle) + (\mathrm{Span}|v^k\rangle)] < \dim(X + \mathrm{Span}|v^0\rangle) \\ + \dim(\mathrm{Span}|v^k\rangle) = 2N + 1. \end{aligned} \tag{B.16}$$

The intersection between the two spaces is not the empty set

$$(X + \mathrm{Span}|v^0\rangle) \cap (\mathrm{Span}|v^k\rangle) \neq \emptyset \tag{B.17}$$

and there exists a vector $|w\rangle \in X + \mathrm{Span}|v^0\rangle$ of the form

$$|w\rangle = \left(x_1, \ldots, x_N, \epsilon\delta\rho_1^0, \ldots, \epsilon\delta\rho_N^0\right) \tag{B.18}$$

which is also in $\mathrm{Span}|v^k\rangle$. This vector can be written as $|w\rangle = \sum_{\mathrm{Re}(\lambda_k)>0} \alpha^k |v^k\rangle$ and the equality of the second half of the components yield

$$\forall i \quad \sum_{\mathrm{Re}(\lambda_k)>0} \alpha^k \delta\rho_i^k = \epsilon\delta\rho_i^0. \tag{B.19}$$

One can thus construct a perturbation, spanned by the $|v_k\rangle$ with $\mathrm{Re}(\lambda_k) > 0$, which is proportional to $|v_k^0\rangle$ and connects $|\rho^{\mathrm{p}})$ to an equilibrated reservoir $|\rho^{\mathrm{p}}) + \epsilon|\delta\rho^0)$ with $\epsilon \neq 0$.

Conversely, the same reasoning would show that, for equilibrated reservoirs, a plateau with N eigenvalues with $\mathrm{Re}(\lambda_k) < 0$ can only be observed in a Right Phase.

B.3 Transverse current in parallel TASEPs

We now show that a definition of the transverse current such as the one given in (7.11) cannot possibly yield a change of sign in K, i.e., $K = 0 \Leftrightarrow \rho_i = \rho_{i\pm1} = 0, 1$. To show this, consider at first $N = 3$ and let us take $K = 0$. Then we have

$$\begin{aligned} d_{12}\rho_1\left(1-\rho_2\right) &= d_{21}\rho_2\left(1-\rho_1\right) \\ d_{23}\rho_2\left(1-\rho_3\right) &= d_{32}\rho_3\left(1-\rho_2\right) \\ d_{31}\rho_3\left(1-\rho_1\right) &= d_{13}\rho_1\left(1-\rho_3\right). \end{aligned} \tag{B.20}$$

Solving the system of equation for ρ_i ($i = 1, 2, 3$) yields the equality

$$\left(d_{12}d_{23}d_{31} - d_{21}d_{32}d_{13}\right)\left(1-\rho_i\right)\rho_i = 0, \tag{B.21}$$

from which we can easily see that either $\rho_i = 0$ or $\rho_i = 1$, i.e. the two solutions that we excluded, or $d_{12}d_{23}d_{31} = d_{21}d_{32}d_{13}$. This last condition corresponds to an exactly null transverse current for any value of the density.

This result can be generalized to the case of an $N-$lane system by using the recursion relation

$$\rho_{i+1} = \frac{\prod_{j=1}^{i} d_{j,j+1}\rho_1}{\prod_{j=1}^{i} d_{j,j+1}\rho_1 + \prod_{j=1}^{i} d_{j+1,j}\left(1-\rho_1\right)} \tag{B.22}$$

and by imposing the periodic condition at the boundary: $\rho_{N+1} = \rho_1$. Then we find that in order to have $K = 0$ for some $\rho_i \neq 0, 1$ one must have $\prod_{j=1}^{N} d_{j,j+1} = \prod_{j=1}^{N} d_{j+1,j}$, which however implies $K = 0 \ \forall \ \rho_i \neq 0, 1$. We have shown here only the necessary condition, but the sufficent one can be proved by taking (7.11) and setting $\prod_{j=1}^{N} d_{j,j+1} = \prod_{j=1}^{N} d_{j+1,j}$ for generic N.

Note that this appendix shows that K cannot vanish if $\rho_i \neq 0, 1$ unless it is always zero. One could imagine, however, that K changes sign discontinuously, without ever satisfying $K = 0$. This never occurs with the simple choice of rates K_{ij} we have considered (which is not very surprising since K can be shown to be the solution of a polynomial equation whose coefficients are continuous functions of ρ_1). More complicated transverse hopping rates, not considered in this work, leading to multiple possibilities of equilibrated plateaux for a given value of ρ_1, could, however, exhibit more complicated behaviours.

Bibliography

[1] J. ADLER – "Chemotaxis in bacteria", *Science* **153** (1966), p. 708–716.

[2] Y. AGHABABAIE, G. I. MENON and M. PLISCHKE – "Universal properties of interacting Brownian motors", *Phys. Rev. E* **59** (1999), p. 2578.

[3] U. ALON, L. CAMARENA, M. G. SURETTE, B. A. ARCAS, Y. LIU, S. LEIBLER and J. B. STOCK – "Response regulator output in bacterial chemotaxis", *EMBO J.* **17** (1998), p. 4238–4248.

[4] R. ASSHETON – "The geometrical relation of the nuclei in an invaginating gastrula (e.g. Amphioxus) considered in connection with cell rhythm, and Driesch's conception of entelechy", *Dev. Genes Evol.* **29** (1910), p. 46–78.

[5] F. K. BALAGADDÉ, H. SONG, J. OZAKI, M. COLLINS, C. H. ANN BARNET, F. H. ARNOLD, S. R. QUAKE and L. YOU – "A synthetic *Escherichia coli* predator-prey ecosystem", *Mol. Syst. Biol.* **4** (2008), p. 187.

[6] M. BASU and P. K. MOHANTY – "Asymmetric simple exclusion process on a cayley tree", *J. Stat. Mech.: Theor. Exp.* (2010), p. P10014.

[7] S. BASU, Y. GERCHMAN, C. H. COLLINS, A. F. H. and R. WEISS – "A synthetic multicellular system for programmed pattern formation", *Nature* **434** (2005), p. 1130–1134.

[8] W. BECHTEL and R. C. RICHARDSON – "Vitalism", Routledge Encyclopedia of Philosophy, London: Routledge, 1998.

[9] B. P. BELOUSOV – "A periodic reaction and its mechanism", *Ref. Radiats. Med.* (1958).

[10] E. BEN-JACOB, O. SCHOCHET, A. TENENBAUM, I. COHEN, A. CZIROK and T. VICSEK – "Generic modelling of cooperative growth patterns in bacterial colonies", *Nature* **368** (1994), p. 46–49.

[11] H. C. BERG – "The rotary motor of bacterial flagella", *Annu. Rev. Biochem.* **72** (2003), p. 19–54.

[12] — , *E. coli in motion*, Springer Science & Business Media, 2008.

[13] H. C. BERG and D. A. BROWN – "Chemotaxis in *Escherichia coli* analysed by three-dimensional tracking", *Nature* **239** (1972), p. 500–504.

[14] W. BIALEK – "Perspectives on theory at the interface of physics and biology", `arXiv:1512.08954 [physics.bio-ph]` (2015).

[15] K. C. BOESCH, R. E. SILVERSMITH and R. B. BOURRET – "Isolation and characterization of nonchemotactic CheZ mutants of *Escherichia coli*", *J. Bacteriol.* **182** (2000), p. 3544–3552.

[16] V. BORMUTH, B. NITZSCHE and F. E. A. RUHNOW – "The highly processive kinesin-8, Kip3, switches microtubule protofilaments with a bias toward the left", *Biophys. J.* **103** (1988), p. L4.

[17] S. S. BRANDA, F. CHU, D. B. KEARNS, R. LOSICK and R. KOLTER – "A major protein component of the *Bacillus subtilis* biofilm matrix", *Mol. Microbiol.* **59** (2006), p. 1229–1238.

[18] M. P. BRENNER, L. S. LEVITOV and E. O. BUDRENE – "Physical mechanisms for chemotactic pattern formation by bacteria", *Biophys. J.* **74** (1998), p. 1677–1693.

[19] J. BRÜGMANN – *Modelling and implementation of a microscopic traffic simulation system*, Logos Verlag Berlin, 2015.

[20] E. O. BUDRENE and H. C. BERG – "Complex patterns formed by motile cells of *Escherichia coli*", *Nature* **349** (1991), p. 630–633.

[21] Y. CAO, M. D. RYSER, S. PAYNE, B. LI, C. V. RAO and L. YOU – "Collective space-sensing coordinates pattern scaling in engineered bacteria", *Cell* **165** (2016), p. 620–630.

[22] M. E. CATES – "Diffusive transport without detailed balance in motile bacteria: does microbiology need statistical physics?", *Rep. Prog. Phys.* **75** (2012), p. 042601.

[23] M. E. CATES, D. MARENDUZZO, I. PAGONABARRAGA and J. TAILLEUR – "Arrested phase separation in reproducing bacteria creates a generic route to pattern formation", *Proc. Natl. Acad. Sci. USA* **107** (2010), p. 11715–11729.

[24] M. E. CATES and J. TAILLEUR – "When are active Brownian particles and run-and-tumble particles equivalent? Consequences for motility-induced phase separation", *Europhys. Lett.* **101** (2013), p. 20010.

[25] M. E. CATES and J. TAILLEUR – "Motility-induced phase separation", *Annu. Rev. Cond. Matt. Phys.* **6** (2015), p. 219–244.

[26] A. CELANI and M. VERGASSOLA – "Bacterial strategies for chemotaxis response", *Proc. Natl. Acad. Sci. USA* **107** (2010), p. 1391–1396.

[27] T. CHOU, K. MALLICK and Z. R. K. P. – "Non-equilibrium statistical mechanics: from a paradigmatic model to biological transport", *Rep. Prog. Phys.* **74** (2011), p. 116601.

[28] D. CHOWDHURY, A. GARAI and J.-S. WANG – "Traffic of single-headed motor proteins KIF1A: effects of lane changing", *Phys. Rev. E* **77** (2008), p. 050902.

[29] D. A. CLARK and L. C. GRANT – "The bacterial chemotactic response reflects a compromise between transient and steady-state behavior", *Proc. Natl. Acad. Sci. USA* **102** (2005), p. 9150–9155.

[30] R. CLÉMENT – "Stéphane Leduc and the vital exception in the life sciences", `arXiv:1512.03660 [q-bio.OT]` (2015).

[31] J. W. COSTERTON, K. J. CHENG, G. G. GEESEY, T. I. LADD, J. C. NICKEL, M. DASGUPTA and T. J. MARRIE – "Bacterial biofilms in nature and disease", *Annu. Rev. Microbiol.* **41** (1987), p. 435–464.

[32] J. W. COSTERTON, Z. LEWANDOWSKI, D. E. CALDWELL, D. R. KORBER and H. M. LAPPIN-SCOTT – "Microbial biofilms", *Annu. Rev. Microbiol.* **49** (1995), p. 711–745.

[33] M. C. CROSS and P. C. HOHENBERG – "Pattern formation outside of equilibrium", *Rev. Mod. Phys.* **65** (1993), p. 851.

[34] A. I. CURATOLO, M. R. EVANS, Y. KAFRI and J. TAILLEUR – "Multilane driven diffusive systems", *J. Phys. A* **49** (2016), p. 095601.

[35] R. DANIELS, J. VANDERLEYDEN and J. MICHIELS – "Quorum sensing and swarming migration in bacteria", *FEMS Microbiol. Rev.* **28** (2004), p. 261–289.

[36] M. E. DAVEY and G. A. O'TOOLE – "Microbial biofilms: from ecology to molecular genetics", *Microbiol. Mol. Biol. Rev.* **64** (2000), p. 847–867.

[37] D. G. DAVIES, M. R. PARSEK, J. P. PEARSON, B. H. IGLEWSKI, J. W. COSTERTON and E. P. GREENBERG – "The involvement of cell-to-cell signals in the development of a bacterial biofilm", *Science* **280** (1998), p. 295–298.

[38] P.-G. DE GENNES – "Chemotaxis: the role of internal delays", *Eur. Biophys. J.* **33** (2004), p. 691–693.

[39] D. S. DEAN – "Langevin equation for the density of a system of interacting Langevin processes", *J. Phys. A* **29** (1996), p. L613.

[40] B. DERRIDA, E. DOMANY and D. MUKAMEL – "An exact solution of a one-dimensional asymmetric exclusion model with open boundaries", *J. Stat. Phys.* **67** (1992), p. 667.

[41] B. DERRIDA, M. R. EVANS, V. HAKIM and V. PASQUIER – "Exact solution of a 1D asymmetric exclusion model using a matrix formulation", *J. Phys. A* **26** (1993), p. 1493.

[42] H. DRIESCH – *The science & philosophy of the organism (The Gifford lectures)*, A. and C. Black (London), 1907.

[43] W. DRIEVER and C. NÜSSLEIN-VOLHARD – "The *bicoid* protein determines position in the Drosophila embryo in a concentration-dependent manner", *Cell* **54** (1988), p. 95–104.

[44] P. B. ECKBURG, E. M. BIK, C. N. BERNSTEIN, E. PURDOM, L. DETHLEFSEN, M. SARGENT, S. R. GILL, K. E. NELSON and D. A. RELMAN – "Diversity of the human intestinal microbial flora", *Science* **308** (2005), p. 1635–1638.

[45] A. D. ECONOMOU, A. OHAZAMA, T. PORNTAVEETUS, P. T. SHARPE, S. KONDO, M. A. BASSON, A. GRITLI-LINDE, M. T. COBOURNE and J. B. A. GREEN – "Periodic stripe formation by a Turing mechanism operating at growth zones in the mammalian palate", *Nat. Genet.* **44** (2012), p. 348–351.

[46] M. R. EVANS, Y. KAFRI, K. E. P. SUGDEN and J. TAILLEUR – "Phase diagram of two-lane driven diffusive systems", *J. Stat. Mech.: Theor. Exp.* (2011), p. P06009.

[47] Y. FILY and M. C. MARCHETTI – "Athermal phase separation of self-propelled particles with no alignment", *Phys. Rev. Lett.* **108** (2012), p. 235702.

[48] R. A. FISHER – "The wave of advance of advantageous genes", *Ann. Hum. Gen.* **7** (1937), p. 355–369.

[49] X. FU, L. H. TANG, C. LIU, J. D. HUANG, T. HWA and P. LENZ – "Stripe formation in bacterial systems with density-suppressed motility", *Phys. Rev. Lett.* **108** (2012), p. 198102.

[50] C. W. FUQUA, S. C. WINANS and E. P. GREENBERG – "Quorum sensing in bacteria: the LuxR-LuxI family of cell density-responsive transcriptional regulators", *J. Bacteriol.* **176** (1994), p. 269–275.

[51] J. L. GARCIA-PALACIOS – "Introduction to the theory of stochastic processes and Brownian motion problems", `arXiv:cond-mat/0701242 [cond-mat.stat-mech]` (2007).

[52] A. GIERER and H. MEINHARDT – "A theory of biological pattern formation", *Biol. Cyber.* **12** (1972), p. 30–39.

[53] K. M. GRAY, L. PASSADOR, B. H. IGLEWSKI and G. E. P. – "Interchangeability and specificity of components from the quorum-sensing regulatory systems of *Vibrio fischeri* and *Pseudomonas aeruginosa*", *J. Bacteriol.* **176** (1994), p. 3076–3080.

[54] P. GREULICH, L. CIANDRINI, R. J. ALLEN and M. C. ROMANO – "A mixed population of competing TASEPs with a shared reservoir of particles", *Phys. Rev. E* **85** (2012), p. 011142.

[55] A. K. GUPTA and I. DHIMAN – "Asymmetric coupling in two-lane simple exclusion processes with Langmuir kinetics: phase diagrams and boundary layers", *Phys. Rev. E* **89** (2014), p. 022131.

[56] S. J. HAGEN (ed.) – *The physical basis of bacterial quorum communication*, Springer, 2015.

[57] J. S. HAGER, J. KRUG, V. POPKOV and G. M. SCHUTZ – "Minimal current phase and universal boundary layers in driven diffusive systems", *Phys. Rev. E* **63** (2001), p. 056110.

[58] M. P. HARRIS, S. WILLIAMSON, J. F. FALLON, H. MEINHARDT and R. O. PRUM – "Molecular evidence for an activator–inhibitor mechanism in development of embryonic feather branching", *Proc. Natl. Acad. Sci. USA* **102** (2005), p. 11734–11739.

[59] R. J. HARRIS and R. B. STINCHCOMBE – "Ideal and disordered two-lane traffic models", *Physica A* **354** (2005), p. 582–596.

[60] M. L. HIGGINS, G. D. SHOCKMAN and A. RYTER – "Procaryotic cell division with respect to wall and membranes", *CRC Crit. Rev. Microbiol.* **1** (1971), p. 29–72.

[61] H. HILHORST and C. APPERT-ROLLAND – "A multi-lane TASEP model for crossing pedestrian traffic flows", *J. Stat. Mech.* (2012), p. P06009.

[62] H. HORN and S. LACKNER – "Modelling of biofilm systems: a review", Productive Biofilms, Springer, 2014, p. 53–76.

[63] J. HOWARD, G. S. W. and J. S. BOIS – "Turing's next steps: the mechanochemical basis of morphogenesis", *Nat. Rev. Mol. Cell Biol.* **12** (2011), p. 392–398.

[64] R. B. HOYLE – *Pattern formation: an introduction to methods*, Cambridge University Press, 2006.

[65] J. S. HUXLEY – *Problems of relative growth*, New York, Lincoln MacVeagh, The Dial Press, 1932.

[66] R. JIANG, M.-B. HU, Y.-H. WU and Q.-S. WU – "Weak and strong coupling in a two-lane asymmetric exclusion process", *Phys. Rev. E* **77** (2008), p. 041128.

[67] R. JIANG, K. NISHINARI, M.-B. HU, Y.-H. WU and Q.-S. WU – "Phase separation in a bidirectional two-lane asymmetric exclusion process", *J. Stat. Phys.* **136** (2009), p. 73.

[68] R. JUHASZ – "Weakly coupled, antiparallel, totally asymmetric simple exclusion processes", *Phys. Rev. E* **76** (2007), p. 021117.

[69] Y. KAFRI and R. A. DA SILVEIRA – "Steady-state chemotaxis in *Escherichia coli*", *Phys. Rev. Lett.* **100** (2008), p. 238101.

[70] N. G. VAN KAMPEN – *Stochastic processes in physics and chemistry*, Elsevier Science Publishers, New York, 1992.

[71] R. KAPRAL and K. SHOWALTER (eds.) – *Chemical waves and patterns: understanding chemical reactivity*, Dordrecht: Kluwer Academic Publishers, 1994.

[72] K. KAWASAKI, A. MOCHIZUKI, M. MATSUSHITA, T. UMEDA and N. SHIGESADA – "Modelling spatio-temporal patterns generated by *Bacillus subtilis*", *J. Theor. Biol.* **188** (1997), p. 177–185.

[73] E. F. KELLER – *Making sense of life: explaining biological development with models, metaphors, and machines*, Harvard University Press, 2009.

[74] E. F. KELLER and L. A. SEGEL – "Model for chemotaxis", *J. Theor. Biol.* **30** (1971), p. 225–234.

[75] — , "Traveling bands of chemotactic bacteria: a theoretical analysis", *J. Theor. Biol.* **30** (1971), p. 235–248.

[76] S. KLUMPP and R. LIPOWSKY – "Traffic of molecular motors through tube-like compartments", *J. Stat. Phys.* **113** (2003), p. 233.

[77] A. KOCH and H. MEINHARDT – "Biological pattern formation: from basic mechanisms to complex structures", *Rev. Mod. Phys.* **66** (1994), p. 1481.

[78] R. KOLTER, D. A. SIEGELE and A. TORMO – "The stationary phase of the bacterial life cycle", *Annu. Rev. Microbiol.* **47** (1993), p. 855–874.

[79] S. KONDO and R. ASAI – "A reaction-diffusion wave on the skin of the marine angelfish *Pomacanthus*", *Nature* **376** (1995), p. 765.

[80] S. KONDO and T. MIURA – "Reaction-diffusion model as a framework for understanding biological pattern formation", *Science* **329** (2010), p. 1616–1620.

[81] W. KONG, A. E. BLANCHARD, C. LIAO and T. LU – "Engineering robust and tunable spatial structures with synthetic gene circuits", *Nucleic Acids Res.* **45** (2017), p. 1005–1014.

[82] J. KRUG – "Boundary-induced phase transitions in driven diffusive systems", *Phys. Rev. Lett.* **67** (1991), p. 1882.

[83] R. G. LARSON – *The structure and rheology of complex fluids*, Oxford University Press (New York), 1999.

[84] C. LEDUC, C. K. PADBERG-GEHLE, V. VARGA, D. HELBING and S. DIEZ – "Molecular crowding creates traffic jams of kinesin motors on microtubules", *Proc. Natl. Acad. Sci. USA* **109** (2012), p. 6100.

[85] S. LEDUC – *Théorie physico-chimique de la vie et générations spontanées*, A. Poinat (Paris), 1910.

[86] — , *La biologie synthétique*, A. Poinat (Paris), 1912.

[87] T. LEPPÄNEN – "The theory of Turing pattern formation", Current Topics In Physics, Imperial College Press, 2005, p. 199–227.

[88] P. LEWUS and R. M. FORD – "Quantification of random motility and chemotaxis bacterial transport coefficients using individual-cell and population-scale assays", *Biotechnol. Bioeng.* **75** (2001), p. 292–304.

[89] J. LIANG, Y. LUO and H. ZHAO – "Synthetic biology: putting synthesis into biology", *Wiley Interdiscip. Rev. Syst. Biol. Med.* **3** (2011), p. 7–20.

[90] C. LIU, X. FU, L. LIU, X. REN, C. K. CHAU, S. LI, L. XIANG, H. ZENG, G. CHEN, L. H. TANG, P. LENZ, X. CUI, W. HUANG, T. HWA and J. D. HUANG – "Sequential establishment of stripe patterns in an expanding cell population", *Science* **334** (2011), p. 238–241.

[91] C. A. LOZUPONE, J. I. STOMBAUGH, J. I. GORDON, J. K. JANSSON and R. KNIGHT – "Diversity, stability and resilience of the human gut microbiota", *Nature* **489** (2012), p. 220–230.

[92] C. T. MACDONALD, J. H. GIBBS and A. C. PIPKIN – "Kinetics of biopolymerization on nucleic acid templates", *Biopolymers* **61** (1968), p. 1–25.

[93] A. MARROCCO, H. HENRY, I. B. HOLLAND, M. PLAPP, S. J. SÉROR and B. PERTHAME – "Models of self-organizing bacterial communities and comparisons with experimental observations", *Math. Model. Nat. Phenom.* **5** (2010), p. 148–162.

[94] V. A. MARTINEZ, R. BESSELING, O. A. CROZE, J. TAILLEUR, M. REUFER, J. SCHWARZ-LINEK, L. G. WILSON, M. A. BEES and W. C. K. POON – "Differential dynamic microscopy: A high-throughput method for characterizing the motility of microorganisms", *Biophys. J.* **103** (2012), p. 1637–1647.

[95] M. B. MILLER and B. L. BASSLER – "Quorum sensing in bacteria", *Annu. Rev. Microbiol.* **55** (2001), p. 165–199.

[96] L. MÖCKL, D. C. LAMB and C. BRÄUCHLE – "Super-resolved fluorescence microscopy: Nobel prize in chemistry 2014 for Eric Betzig, Stefan Hell, and William E. Moerner", *Angew. Chem. Int. Ed.* **53** (2014), p. 13972–13977.

[97] P. MOTTISHAW, B. WACLAW and M. R. EVANS – "An exclusion process on a tree with constant aggregate hopping rate", *J. Phys. A* **46** (2013), p. 405003.

[98] D. MUKAMEL – "Phase transitions in non-equilibrium systems", Soft and Fragile Matter: Non-equilibrium Dynamics, Metastability and Flow (M. E. Cates and M. R. Evans, eds.), Institute of Physics Publishing, Bristol, 2000, p. 237–258.

[99] S. MUKHERJI and A. VAN OUDENAARDEN – "Synthetic biology: understanding biological design from synthetic circuits", *Nat. Rev. Genet.* **10** (2009), p. 859.

[100] J. D. MURRAY – *Mathematical biology: II. Spatial models and biomedical applications*, 3 ed., Springer, 2002.

[101] P. NANNIPIERI, J. ASCHER, M. CECCHERINI, L. LANDI, G. PIETRAMELLARA and G. RENELLA – "Microbial diversity and soil functions", *Eur. J. Soil Sci.* **54** (2003), p. 655–670.

[102] I. NERI, N. KERN and A. PARMEGGIANI – "Totally asymmetric simple exclusion process on networks", *Phys. Rev. Lett.* **107** (2011), p. 068702.

[103] K. NISHINARI, Y. OKADA, A. SCHADSCHNEIDER and D. CHOWDHURY – "Intracellular transport of single-headed molecular motors KIF1A", *Phys. Rev. Lett.* **95** (2005), p. 118101.

[104] D. ORIOLA, S. ROTH, M. DOGTEROM and C. J. – "Formation of helical membrane tubes around microtubules by single-headed kinesin KIF1A", *Nat. Commun.* **6** (2015), p. 8025.

[105] M. R. PARSEK and E. P. GREENBERG – "Sociomicrobiology: the connections between quorum sensing and biofilms", *Trends Microbiol.* **13** (2005), p. 27–33.

[106] S. PAYNE, B. LI, Y. CAO, D. SCHAEFFER, M. D. RYSER and Y. L. – "Temporal control of self-organized pattern formation without morphogen gradients in bacteria", *Mol. Syst. Biol.* **9** (2013), p. 697.

[107] O. PENROSE – "Kinetics of phase transitions", Stochastic processes in nonequilibrium systems, Springer, 1978, p. 210–234.

[108] E. C. PESCI, J. P. PEARSON, P. C. SEED and B. H. IGLEWSKI – "Regulation of *las* and *rhl* quorum sensing in *Pseudomonas aeruginosa*", *J. Bacteriol.* **179** (1997), p. 3127–3132.

[109] V. POPKOV and M. SALERNO – "Hydrodynamic limit of multichain driven diffusive models", *Phys. Rev. E* **69** (2004), p. 046103.

[110] V. POPKOV and G. M. SCHUTZ – "Steady-state selection in driven diffusive systems with open boundaries", *Europhys. Lett.* **48** (1999), p. 257.

[111] — , "Shocks and excitation dynamics in a driven diffusive two-channel system", *J. Stat. Phys.* **112** (2003), p. 523.

[112] L. A. PRATT and R. KOLTER – "Genetic analysis of *Escherichia coli* biofilm formation: roles of flagella, motility, chemotaxis and type I pili", *Mol. Microbiol.* **30** (1998), p. 285–293.

[113] E. PRONINA and A. B. KOLOMEISKY – "Two-channel totally asymmetric simple exclusion processes", *J. Phys. A* **37** (2004), p. 9907–9918.

[114] T. REICHENBACH, F. T. and F. E. – "Traffic jams induced by rare switching events in two-lane transport", *New J. Phys.* **9** (2007), p. 159.

[115] M. G. SANNA and M. I. SIMON – "In vivo and in vitro characterization of *Escherichia coli* protein CheZ gain- and loss-of-function mutants", *J. Bacteriol.* **178** (1996), p. 6275–6280.

[116] J. SARAGOSTI, P. SILBERZAN and A. BUGUIN – "Modelling *E. coli* tumbles by rotational diffusion. Implications for chemotaxis", *PLoS One* **7** (2012), p. e35412.

[117] A. SCHADSCHNEIDER – "Modelling of transport and traffic problems", p. 22–31, Springer Berlin Heidelberg, 2008.

[118] Y. SCHAERLI, A. MUNTEANU, M. GILI, J. COTTERELL, J. SHARPE and M. ISALAN – "A unified design space of synthetic stripe-forming networks", *Nat. Commun.* **5** (2014), p. 4905.

[119] C. SCHIFFMANN, C. APPERT-ROLLAND and L. SANTEN – "Shock dynamics of two-lane driven lattice gases", *J. Stat. Mech.: Theor. Exp.* (2010), p. P06002.

[120] B. SCHMITTMANN, J. KROMETIS and R. K. P. ZIA – "Will jams get worse when slow cars move over?", *Europhys. Lett.* **70** (2005), p. 299–305.

[121] B. SCHMITTMANN and R. K. P. ZIA – *Statistical mechanics of driven diffusive systems*, Phase Transitions and Critical Phenomena, vol. 17, Academic Press, 1995.

[122] M. J. SCHNITZER – "Theory of continuum random walks and application to chemotaxis", *Phys. Rev. E* **48** (1993), p. 2553–2568.

[123] M. J. SCHNITZER, S. M. BLOCK, H. C. BERG and E. M. PURCELL – "Strategies for chemotaxis", *Symp. Soc. Gen. Microbiol.* **46** (1990), p. 15–34.

[124] G. SCHUTZ and E. DOMANY – "Phase transitions in an exactly soluble one-dimensional exclusion process", *J. Stat. Phys.* **72** (1993), p. 277.

[125] A. SEMINARA, T. E. ANGELINI, J. N. WILKING, H. VLAMAKIS, S. EBRAHIM, R. KOLTER, D. A. WEITZ and M. P. BRENNER – "Osmotic spreading of *Bacillus subtilis* biofilms driven by an extracellular matrix", *Proc. Natl. Acad. Sci. USA* **109** (2012), p. 1116–1121.

[126] J. A. SHAPIRO – "Thinking about bacterial populations as multicellular organisms", *Annu. Rev. Microbiol.* **52** (1998), p. 81–104.

[127] S. SICK, S. REINKER, J. TIMMER and T. SCHLAKE – "WNT and DKK determine hair follicle spacing through a reaction-diffusion mechanism", *Science* **314** (2006), p. 1447–1450.

[128] R. E. SILVERSMITH, M. D. LEVIN, E. SCHILLING and R. B. BOURRET – "Kinetic characterization of catalysis by the chemotaxis phosphatase CheZ - Modulation of activity by the phosphorylated CheY substrate", *J. Biol. Chem.* **283** (2008), p. 756–765.

[129] A. B. SLOWMAN, M. R. EVANS and R. A. BLYTHE – "Exact solution of two interacting run-and-tumble random walkers with finite tumble duration", `arXiv:1705.04812 [cond-mat.stat-mech]` (2017).

[130] P. SOLLICH – "Predicting phase equilibria in polydisperse systems", *J. Phys.: Condens. Matter* **14** (2001), p. R79.

[131] P. SOLLICH, P. B. WARREN and M. E. CATES – "Moment free energies for polydisperse systems", *Adv. Chem. Phys.* **116** (2001), p. 265–336.

[132] A. P. SOLON, M. E. CATES and J. TAILLEUR – "Active Brownian particles and run-and-tumble particles: a comparative study", *Eur. Phys. J. Spec. Top.* **224** (2015), p. 1231–1262.

[133] A. P. SOLON, Y. FILY, A. BASKARAN, M. E. CATES, Y. KAFRI, M. KARDAR and T. J. – "Pressure is not a state function for generic active fluids", *Nat. Phys.* **11** (2015), p. 673–678.

[134] A. P. SOLON, J. STENHAMMAR, M. E. CATES, Y. KAFRI and J. TAILLEUR – "Generalized thermodynamics of phase equilibria in scalar active matter", `arXiv:1609.03483 [cond-mat.stat-mech]` (2016).

[135] H. SONG, S. PAYNE, M. GRAY and L. YOU – "Spatiotemporal modulation of biodiversity in a synthetic chemical-mediated ecosystem", *Nat. Chem. Biol.* **5** (2009), p. 929–935.

[136] S. P. STRONG, B. FREEDMAN, W. BIALEK and R. KOBERLE – "Adaptation and optimal chemotactic strategy for *E. coli*", *Phys. Rev. E* **57** (1998), p. 4604.

[137] K. E. P. SUGDEN, M. R. EVANS, W. C. K. POON and N. D. READ – "Model of hyphal tip growth involving microtubule-based transport", *Phys. Rev. E* **75** (2007), p. 031909.

[138] J. J. TABOR, H. SALIS, Z. B. SIMPSON, A. A. CHEVALIER, A. LEVSKAYA, E. M. MARCOTTE, C. A. VOIGT and A. D. ELLINGTON – "A synthetic genetic edge detection program", *Cell* **137** (2009), p. 1272–1281.

[139] J. TAILLEUR and M. E. CATES – "Statistical mechanics of interacting run-and-tumble bacteria", *Phys. Rev. Lett.* **100** (2008), p. 218103.

[140] J. TAILLEUR, M. R. EVANS and K. Y. – "Non-equilibrium phase transitions in tubulation by molecular motors", *Phys. Rev. Lett.* **102** (2009), p. 118109.

[141] A. G. THOMPSON, J. TAILLEUR, M. E. CATES and R. A. BLYTHE – "Lattice models of non-equilibrium bacterial dynamics", *J. Stat. Mech.: Theor. Exp.* **2011** (2011), p. P02029.

[142] D. W. THOMPSON – *On growth and form*, 2 ed., Cambridge University Press, 1942.

[143] V. TORSVIK, J. GOKSØYR and F. L. DAAE – "High diversity in DNA of soil bacteria", *Applied and environmental microbiology* **56** (1990), p. 782–787.

[144] A. TURING – "The chemical basis of morphogenesis", *Philos. Trans. R. Soc. Lond., B, Biol. Sci.* **237** (1952), p. 37–72.

[145] R. TYSON, S. R. LUBKIN and J. D. MURRAY – "A minimal mechanism for bacterial pattern formation", *Proc. R. Soc. Lond., B, Biol. Sci.* **266** (1999), p. 299–304.

[146] — , "Model and analysis of chemotactic bacterial patterns in a liquid medium", *J. Math. Biol.* **38** (1999), p. 359–375.

[147] R. VALE and Y. TOYOSHIMA – "Rotation and translocation of microtubules in vitro induced by dyneins from Tetrahymena cilia", *Cell* **52** (1988), p. 459.

[148] M. C. M. VAN LOOSDRECHT, J. J. HEIJNEN, H. EBERL, J. KREFT and C. PICIOREANU – "Mathematical modelling of biofilm structures", *Antonie van Leeuwenhoek* **81** (2002), p. 245–256.

[149] S. VAN VLIET and M. ACKERMANN – "Bacterial ventures into multicellularity: collectivism through individuality", *PLoS Biol.* **13** (2015), p. e1002162.

[150] Y.-Q. WANG, R. JIANG, Q.-S. WU and H.-Y. WU – "Phase transitions in three-lane TASEPs with weak coupling", *Mod. Phys. Lett. B* **28** (2014), p. 1450123.

[151] J. D. WATSON and F. H. C. CRICK – "Molecular structure of nucleic acids", *Nature* **171** (1953), p. 737–738.

[152] A. J. WOLFE and H. C. BERG – "Migration of bacteria in semisolid agar", *Proc. Natl. Acad. Sci. USA* **86** (1989), p. 6973–6977.

[153] L. WOLPERT – "Positional information and the spatial pattern of cellular differentiation", *J. Theor. Biol.* **25** (1969), p. 1–47.

[154] D. E. WOODWARD, R. TYSON, M. R. MYERSCOUGH, J. D. MURRAY, E. O. BUDRENE and H. C. BERG – "Spatio-temporal patterns generated by *Salmonella typhimurium*", *Biophys. J.* **68** (1995), p. 2181–2189.

[155] V. YADAV, R. SINGH and S. MUKHERJI – "Phase-plane analysis of driven multi-lane exclusion models", *J. Stat. Mech.: Theor. Exp.* (2012), p. P04004.

[156] L. YOU, R. S. COX, R. WEISS and F. H. ARNOLD – "Programmed population control by cell-cell communication and regulated killing", *Nature* **428** (2004), p. 868–871.

[157] A. N. ZAIKIN and A. M. ZHABOTINSKY – "Concentration wave propagation in two-dimensional liquid-phase self-oscillating system", *Nature* **225** (1970), p. 535–537.